



**HAL**  
open science

# Micromechanical modeling of initially anisotropic clayey rocks considering water saturation effect

Jianjian Zhao

► **To cite this version:**

Jianjian Zhao. Micromechanical modeling of initially anisotropic clayey rocks considering water saturation effect. Civil Engineering. Université de Lille, 2021. English. NNT : 2021LILUI026 . tel-03960838

**HAL Id: tel-03960838**

**<https://theses.hal.science/tel-03960838>**

Submitted on 28 Jan 2023

**HAL** is a multi-disciplinary open access archive for the deposit and dissemination of scientific research documents, whether they are published or not. The documents may come from teaching and research institutions in France or abroad, or from public or private research centers.

L'archive ouverte pluridisciplinaire **HAL**, est destinée au dépôt et à la diffusion de documents scientifiques de niveau recherche, publiés ou non, émanant des établissements d'enseignement et de recherche français ou étrangers, des laboratoires publics ou privés.

**THÈSE DE DOCTORAT  
DE L'UNIVERSITÉ DE LILLE**

**LABORATOIRE DE MÉCANIQUE, MULTIPHYSIQUE ET  
MULTIECHELLE (UMR9013, CNRS)**

Présentée par

**Jianjian ZHAO**

pour l'obtention du grade de

**DOCTEUR DE L'UNIVERSITÉ DE LILLE**

Domaine

**GÉNIE CIVIL**

Sujet de la thèse

**Modélisation micromécanique des roches argileuses initialement  
anisotropes avec la prise en compte des effets de saturation**

**(Micromechanical modeling of initially anisotropic clayey rocks  
considering water saturation effect)**

Soutenue le 27 Janvier 2021 devant le jury composé de :

<b>Mme. Hélène DUMONTET</b>	Professeur	Sorbonne Université	<i>Présidente du jury</i>
<b>Mr. Dashnor HOXHA</b>	Professeur	Université d'Orléans	<i>Rapporteur</i>
<b>Mr. Mountaka SOULEY</b>	Dr. HDR	INERIS	<i>Rapporteur</i>
<b>Mr. Minh Ngoc VU</b>	Docteur	ANDRA	<i>Examineurs</i>
<b>Mr. Wanqing SHEN</b>	MCF HDR	Université de Lille	<i>Invité</i>
<b>Mr. Jean Baptiste COLLIAT</b>	Professeur	Université de Lille	<i>Co-directeur de thèse</i>
<b>Mr. Jianfu SHAO</b>	Professeur	Université de Lille	<i>Directeur de thèse</i>

**LAMCUBE - L'UNIVERSITÉ DE LILLE**

## Abstract

This thesis aims to propose a new constitutive model that can describe the elastic-plastic deformation, time-dependent deformation, and induced damage in clayey rocks under hydro-mechanical coupling. To this end, the macroscopic elastic tensor and plastic yield criterion are determined by two steps of homogenization, considering the transversely isotropic solid clay matrix, pores, and inclusions at three distinct scales. The effective elastic properties of clayey rocks are estimated by using the Mori-Tanaka scheme. And the key step in calculating the effective elastic properties of clayey rocks is to use an efficient numerical method to determine the Hill's tensor of the spheroidal inclusions in the transversely isotropic matrix at mesoscale and the Hill's tensor of the pores inside the porous matrix at the microscale. Then, the damage of rocks due to the debonding of matrix-inclusions interfaces is taken into account and coupled with both the elastic and plastic properties. Further, the time-dependent behavior of clayey rocks is also considered as the delayed plastic strain. Moreover, the effect of water saturation on the elastic and plastic behavior of clayey rocks is investigated. The methodology for the determination of parameters involved in the model is presented.

Based on this model and identified parameters, a series of laboratory tests have been simulated, including lateral decompression tests with constant mean stress, conventional triaxial compression tests with different water saturation degrees, and creep tests. Besides, the proposed model is implemented in a finite element code considering hydromechanical processes, and then applied to studying hydromechanical responses during in situ experiments realized in the underground research laboratory of ANDRA. Variations and distributions of displacement and pore pressure around the gallery are investigated and compared with *in situ* measurements.

**Keywords:** Clayey rocks; anisotropic rocks; plasticity; damage; viscoplasticity; micromechanics.

## Résumé

Cette thèse vise à proposer un nouveau modèle constitutif qui peut décrire la déformation élastique-plastique, la déformation en fonction du temps et l'endommagement induit dans les roches argileuses sous couplage hydromécanique. À cette fin, le tenseur élastique macroscopique et le critère de plasticité sont déterminés par deux étapes d'homogénéisation, en considérant la matrice argileuse solide isotrope transverse, les pores, et les inclusions à trois échelles distinctes. Les propriétés élastiques effectives des roches argileuses sont estimées en utilisant le schéma de Mori-Tanaka. Et l'étape clé dans le calcul des propriétés élastiques effectives des roches argileuses est de proposer une méthode numérique efficace pour déterminer le tenseur de Hill des inclusions sphéroïdales dans la matrice isotrope transverse à l'échelle mésoscopique et le tenseur de Hill des pores à l'intérieur de la matrice poreuse à l'échelle microscopique. Ensuite, l'endommagement des roches dû au décollement des interfaces matrice-inclusions est pris en compte et couplés aux propriétés élastiques et plastiques. De plus, le comportement des roches argileuses en fonction du temps est également étudié comme la déformation plastique retardée. De plus, l'effet de la saturation en eau sur le comportement élastique et plastique des roches argileuses est étudié. La méthodologie pour la détermination des paramètres introduits dans le modèle est présentée.

Sur la base de ce modèle et des paramètres identifiés, une série de tests de laboratoire ont été simulés, y compris des tests de décompression latérale avec une contrainte moyenne constante, des tests de compression triaxiale conventionnelle avec différents degrés de saturation en eau, et des tests de fluage. En outre, le modèle proposé est implémenté dans un code d'éléments finis prenant en compte les processus hydromécaniques, puis appliqué à l'étude des réponses hydromécaniques lors des expériences *in situ* réalisées dans le laboratoire de recherche souterrain de l'ANDRA. Les variations et les distributions du déplacement et de la pression interstitielle autour de la galerie sont étudiées et comparées aux mesures *in situ*.

**Mots clés:** Roches argileuses; roches anisotropes; plasticité; endommagement; viscoplasticité; micromécanique.

## Acknowledgement

First of all, I would like to express my thanks to my supervisor Professor Jianfu SHAO for his careful and patient guidance throughout my research. He also gave me a lot of valuable suggestions in my academic paper and thesis writing. His rigorous attitude to scientific research is my best example, and I am proud to be one of his students.

I would like to thank Professor Jean-Baptiste COLLIAT for his support and motivation throughout my research.

Then, I am deeply grateful to Professor Wanqing SHEN. When I encountered problems in my research, he always gave me good solutions and devoted a lot of time to my research work. His rigorous research attitude will have a good influence on my future work and studies.

In addition, I would like to thank Professor Hanbing BIAN for his guidance and help in the last part of my thesis.

Further, I would also like to thank Professor Yun JIA. She gave me a lot of support and encouragement during my studies.

Special thanks to Dr. Zhan YU and Dr. Yue SUN for their help in my research and life. I would also like to thank my colleagues Dr. Yudan JIN, Dr. Yue TONG, Dr. Hailing SHI, Dr. Xi CHEN, and Dr. Dongmei ZHANG. They are very friendly and willing to provide me with help and motivation.

Thanks to my friends Dr. Xiaodan CAO, Dr. Alexis DOS SANTOS, Jueliang CHEN, Siyu LIU, Wang ZHANG, Meng WANG, Changdong DING, Yuhao ZHANG, Jinzhou BAI.

Also, I would like to thank the China Scholarship Council (CSC) for its financial support during my research period.

Finally, I would like to thank my family for their weekly video encouragement, which makes me feel close to them in a faraway country.

Jianjian ZHAO

# Contents

<b>Contents</b>	<b>i</b>
<b>Notations</b>	<b>v</b>
<b>General Introduction</b>	<b>vii</b>
<b>I Introduction of CO<sub>x</sub> clayey rocks and research objective of the thesis</b>	<b>1</b>
1 General information about CO <sub>x</sub> clayey rocks . . . . .	1
1.1 Context . . . . .	1
1.2 Macroscopic behavior of inherently anisotropic clayey rocks under hydro-mechanical coupling . . . . .	3
1.3 Micro-mesoscopic properties of inherently anisotropic clayey rocks . . . . .	9
2 Mechanical behavior of the anisotropic material . . . . .	13
2.1 Transversely isotropic material . . . . .	15
2.2 Orthotropic materials and Monoclinic materials . . . . .	17
2.3 Isotropic materials . . . . .	19
3 Industrial context and objective of this thesis . . . . .	19
4 Conclusions . . . . .	20
<b>II Linear homogenization method considering initial anisotropy and water saturation effect applied to CO<sub>x</sub> claystone</b>	<b>23</b>
1 Introduction . . . . .	23
2 Effective elastic property of CO <sub>x</sub> claystone . . . . .	24
2.1 Determination of elastic properties . . . . .	25
2.2 Localization tensor $\mathbb{A}$ . . . . .	27
3 Eshelby's solution for isotropic inclusions . . . . .	29
3.1 Green's function for transversely isotropic matrix . . . . .	30
3.2 Hill's tensor for transversely isotropic matrix . . . . .	32
4 Hydraulic properties of claystone . . . . .	36
5 Conclusions . . . . .	38
<b>III Nonlinear homogenization method applied to CO<sub>x</sub> claystone that considers the macroscopic plastic-viscoplastic criterion, hydraulic effects,</b>	

<b>and damage</b>	<b>39</b>
1 Introduction . . . . .	39
2 Description of macroscopic plastic criterion . . . . .	41
3 Extension of the macroscopic yield criterion . . . . .	46
3.1 Macroscopic yield criterion considering anisotropic effects . . . . .	46
3.2 Constitutive model for long-term behavior of clayey rocks . . . . .	53
3.3 Description of damage . . . . .	54
3.4 Effect of hydro-mechanical coupling on plastic deformation of clayey rocks . . . . .	61
4 Conclusions . . . . .	62
<b>IV Abaqus implementation, simulations of CO<sub>x</sub> claystone laboratory tests</b>	<b>65</b>
1 Introduction . . . . .	65
2 Identification of model's parameters . . . . .	66
2.1 Elastic parameters . . . . .	66
2.2 Plastic, viscoplastic and damage parameters . . . . .	68
2.3 Hydro-mechanical coupling parameters for partially saturated media	71
3 Comparisons between numerical and experimental results . . . . .	75
3.1 Lateral decompression test . . . . .	76
3.2 Triaxial compression tests with different water saturation . . . . .	77
3.3 Time-dependent plastic deformation simulation results . . . . .	80
4 Conclusions . . . . .	81
<b>V Simulations of in-situ experiments</b>	<b>83</b>
1 Introduction . . . . .	83
2 Background and research objectives . . . . .	84
3 Presentation of excavation model . . . . .	88
3.1 Identification of elastic, plastic and viscoplastic parameters . . . . .	88
3.2 Boundary conditions . . . . .	90
3.3 Verification of numerical accuracy . . . . .	94
4 Numerical modeling of excavation deformation zones . . . . .	95
4.1 Excavation simulations under purely mechanical conditions . . . . .	95
4.2 Excavation simulations under hydro-mechanical coupling conditions	99
5 Conclusions . . . . .	105

<b>VI Conclusions and perspectives</b>	<b>107</b>
1 Conclusions . . . . .	107
2 Perspectives . . . . .	108
<b>VII Appendix</b>	<b>109</b>
<b>Bibliography</b>	<b>115</b>



# Notations

## Common notations

$\tilde{\sigma}, \sigma$	Local stress tensor in solid clay phase and in porous clay matrix
$\Sigma$	Macroscopic stress tensor
$d$	Local strain rate of porous clay matrix
$D$	Macroscopic strain rate
$\hat{\varepsilon}^m, \hat{\varepsilon}^i$	Local strain tensor of porous clay matrix and inclusions
$\tilde{\varepsilon}^p$	Equivalent plastic strain in the solid clay phase
$E^e, E^p, E^{vp}, E$	Macroscopic elastic, plastic, viscoplastic, and total strain tensor
$E^{hom}$	Macroscopic Young's modulus
$\nu^{hom}$	Macroscopic Poisson's ratio
$G^{hom}$	Macroscopic shear modulus
$K$	Macroscopic Bulk modulus
$\dot{\lambda}$	Plastic multiplier
$C^s, C^i, C^{pm}$	Local elastic tensor of the solid clay phase, inclusions, and porous matrix
$C^{hom}, S$	Macroscopic elastic stiffness and flexibility matrix
$L^{pm}$	Local tangent elastic-plastic operator of the porous matrix
$C^{tan}$	Macroscopic tangent elastic-plastic stiffness tensor
$\tilde{A}$	Transformation matrix
$A$	Localization tensor
$G$	Green's function
$P$	Hill's tensor
$S^E$	Eshelby's tensor

**Model parameters**

$c$	Cohesion
$\varphi$	Frictional angle
$f$	Porosity
$\rho$	Volumetric fraction of inclusion
$h$	Hydrostatic tensile yield stress
$b_1, b_2, b_{vp}$	Plastic and viscoplastic parameters
$T, t$	Frictional coefficients
$\eta$	Scalar parameter
$\theta$	Angle between the loading direction and the bedding plane
$\mathbf{l}$	Normalized loading orientation vector
$\mathbf{L}$	Loading vector
$\eta_1, m$	Parameters controlling the evolution of viscoplastic strain rate
$S_0, M$	Parameters controlling the debonding degree
$S_{lq}$	Saturation
$H_r$	Relative humidity
$p_{cp}$	Capillary pressure
$i$	Hydraulic gradient
$M_{vp}^{ol}$	Molar mass of vapor
$R$	Universal gas constant
$T_{abs}$	Absolute temperature
$\rho_{lq}$	Volumetric mass of liquid
$\underline{Q}$	Flow rate
$k$	Permeability
$\underline{K}$	Hydraulic conductivity in the flow direction
$\underline{g}$	Acceleration due to gravity
$\mu_{lq}$	Dynamic viscosity of the fluid mass
$\mathbf{B}$	Second-order tensor of macroscopic Biot's coefficient
$\beta_1, \beta_2$	Parameters controlling the hydraulic effect

# General Introduction

Clayey rocks are often encountered in many underground projects. Due to their stable physical-mechanical properties and low permeability, they are used as a potential geological formation for nuclear waste disposal. Therefore, it is of great value to study the physical and mechanical properties of clayey rocks. The clayey rocks are characterized by complex mineralogical compositions and multi-scale micro-structures. At the usually called mesoscopic scale (from hundreds of micrometers to mm), these different mineral compositions with different sizes and shapes are randomly distributed in the porous clay matrix and bonded with the clay matrix to bear the external loads. At the microscopic scale (tens of micrometers), with the help of different kinds of techniques, the clay matrix is found to consist of solid clay phase and pores. Even at smaller scales, such as nanometers, the solid clay particle also has a complex structure. On the basis of previous research, a number of macroscopic multi-scale models have been developed, but most of these models ignore the influence of pores inside the clay matrix. In this thesis, clayey rocks are considered to contain mineral particles, pores and solid clay phase at two relevant scales (i.e., mesoscopic and microscopic scales), and two homogenization steps are introduced to study their mechanical properties. The first homogenization step is realized to estimate the effective elastic properties and to establish the effective plastic criterion of the porous matrix by considering the effect of pores. The second homogenization step is devoted to estimating the macroscopic elastic properties and formulating the macroscopic plastic criterion of the inclusion-reinforced clay composite.

On the other hand, many of the multi-scale models developed so far are based on the assumption of isotropic materials. However, due to the presence of the bedding plane and the random distribution of mineral grains, the clayey rocks exhibit different kinds of inherent anisotropy. For the study of the physical and mechanical behavior of clayey rocks, it is important and complex to propose a numerical simulation model that can consider their anisotropy from microscopic scale to macroscopic scale, especially when the simulation model needs to take into account both the mineral particles, the solid matrix

and the pores inside the clay matrix. An important step in the homogenization procedure for anisotropic materials is to establish a suitable relation between the macroscopic strain and the local strain. Therefore, the Mori-Tanaka scheme is selected to estimate the elastic properties of the anisotropic clayey rocks. Besides, the Eshelby and Hill polarization tensors are introduced to consider the influence of embedded minerals and pores in the anisotropic porous matrix. And these polarization tensors depend on the shape of the mineral particles or pores and elastic properties of the porous clay matrix. In addition, for plastic deformation calculation, the macroscopic strength criterion for anisotropic claystone is much more complex than the classical Drucker-Prager criterion and many influencing factors need to be taken into account. This thesis proposes a macroscopic yield criterion that considers the anisotropy of the clay matrix, which also takes into account the influence of mineral particles and voids inside the clay matrix. The degree of anisotropy of the clayey rocks in this macroscopic yield criterion can be achieved by adjusting the value of  $\eta$ .

The damage in this multi-scale anisotropic model is mainly considered to be caused by the debonding of the interface between the inclusions and the surrounding clay matrix. In the initial state, the interface is assumed to be perfectly bonded in the elastic regime. The interface is completely debonded after the damage is activated. The degree of damage is evaluated by a Weibull's probability distribution function. When the interface between the mineral particle and clay matrix is debonded, this mineral particle is considered to be a void that can't bear the load any longer. On the other hand, with the progress of interface debonding, the porosity increases while the volumetric fraction of mineral particles decreases. Besides, changes in porosity will also have an impact on the macroscopic effective stiffness. Therefore, for the multi-scale model in this thesis, the damage caused by the interfacial debonding is a complex process that affects the simulation results of macroscopic elastic and plastic deformation of the clayey rocks.

Considering the actual complex geological conditions, the hydro-mechanical coupling effect is also considered in the multi-scale model of this thesis. We assume that the effective elastic modulus of the porous clay matrix and the plastic frictional coefficient will vary with the pore water pressure. Another, pore pressure (or saturation) affects the plastic and potential functions by using the net stress tensor in this thesis. Further, a mechanism for time-dependent behavior is proposed in this thesis: viscoplastic strain. The viscoplastic strain also is considered to be anisotropic and depends on the loading orientation.

This thesis aims to propose an anisotropic multi-scale model that can be used to describe the elastic-plastic deformation, time-dependent deformation, and induced damage

in clayey rocks under hydro-mechanical coupling conditions. And this thesis is divided into five chapters and organized as follows:

In Chapter I , a bibliographic review is first presented about the basic physical-mechanical properties of anisotropic clayey rocks. The complex characteristics of the clayey rocks in the actual geological environment are presented in terms of the size and distribution of mineral particles and voids, as well as the permeability of clayey rocks. Secondly, several different types of anisotropic structures are discussed because of the anisotropy of clayey rocks in the actual geological environment. They are transversely isotropic, orthorhombic, and monoclinic materials. And the elastic properties of inherently isotropic structure is also presented in this section. The final section presents the main research objectives and issues of this thesis.

In Chapter II , firstly, the macroscopic stress-strain relations of clayey rocks are expressed using the two homogenization steps. Secondly, two different homogenization schemes for calculating the effective macroscopic stiffness tensor are presented, and each scheme considers different material microstructures. For the multi-scale anisotropic model of this thesis, taking into account the interactions between the minerals and pores inside the clay matrix, the Mori-Tanaka scheme is chosen. This section also introduces the basic theory of Green's function in order to consider the anisotropic characteristics of porous clay matrix. Finally, the influence of hydraulic on the elastic properties of clayey rocks is considered.

In Chapter III , macroscopic plastic yield criterion is determined by two steps of homogenization, taking into account the isotropic solid clay phase, pores, and mineral particles. An extension of the macroscopic yield criterion is then defined, including the macroscopic criterion that takes into account clayey rocks anisotropy, time-dependent deformation, damage, and hydro-mechanical coupling effects. In this section, the relation between the pore pressure and the maximum frictional coefficient is established.

Chapter IV focuses on the simulations of laboratory experiments using the multi-scale anisotropic model presented in Chapters II and III . For this chapter, three sections are presented. The first section mainly deals with the determination of the model's parameters. The second section involves three different experimental simulations, including the lateral decompression tests with different loading orientations, the normal triaxial compression tests with different relative humidity, and the creep tests. The last section deals with further analysis and related conclusions.

Chapter V presents the simulation results about the excavation disturbance zone around the gallery using the multi-scale anisotropic model presented in Chapters II and

III . For this chapter, three sections are presented. The first section is a review of the background and objective of excavation simulation. The second section introduces the simulation model, including parameters determination, mesh, dimensions of the excavation model, and the stress distribution. The last section deals with presenting the results of the excavation simulations, divided into two cases: excavation simulations under purely mechanical conditions and excavation simulations under hydro-mechanical coupling conditions.

# Chapter I

## Introduction of CO<sub>x</sub> clayey rocks and research objective of the thesis

### Contents

---

<b>1</b>	<b>General information about CO<sub>x</sub> clayey rocks . . . . .</b>	<b>1</b>
1.1	Context . . . . .	1
1.2	Macroscopic behavior of inherently anisotropic clayey rocks under hydro-mechanical coupling . . . . .	3
1.3	Micro-mesoscopic properties of inherently anisotropic clayey rocks . . .	9
<b>2</b>	<b>Mechanical behavior of the anisotropic material . . . . .</b>	<b>13</b>
2.1	Transversely isotropic material . . . . .	15
2.2	Orthotropic materials and Monoclinic materials . . . . .	17
2.3	Isotropic materials . . . . .	19
<b>3</b>	<b>Industrial context and objective of this thesis . . . . .</b>	<b>19</b>
<b>4</b>	<b>Conclusions . . . . .</b>	<b>20</b>

---

## 1 General information about CO<sub>x</sub> clayey rocks

### 1.1 Context

At present, several countries (e.g., French, Belgium, Switzerland, Canada) consider the deep geological repository as a relative security disposal solution for high- and long-lived radioactive wastes. In order to ensure that nuclear waste does not pollute the surrounding

environment, the deep buried geological repository method should have several functions as follows:

- ★ The geological repository is away from human habitation;
- ★ The geological rocks that wrap the nuclear waste should have better impermeability to prevent nuclear waste pollutants into the groundwater;
- ★ Long-term creep performance should be stable.

The Callovian-Oxfordian (COx) clayey rocks are disposed at depth of about 420m to 550m [Andra, 2005b] and have an inherent anisotropic property. Due to its extremely low permeability and relatively high compressive strength, it has been selected as a candidate host rock for the potential repository. Therefore, the study of its physical and mechanical behavior is an essential research project. Over the past few years, a large number of experimental tests have been carried out on the clayey rocks. For example, the French national agency for radioactive waste management (ANDRA) constructed the Meuse/Haute-Marne URL (completed in the year 2000), which is located about 300 kilometers northeast of Paris. Many *in situ* experiments have been completed. The experimental drifts are mainly at the depth of 490m and 445m, generally (as shown in Figure I .1).

As shown in Figure I .1, the experimental drifts at 445m are not at the same level as the main level 490m. *In situ* experiments illustrate that the drifts at 445m does not exhibit the significantly induced fracture networks by the excavation at depth of 490m. Therefore, some relatively intact samples can be drilled from this layer for laboratory testing.

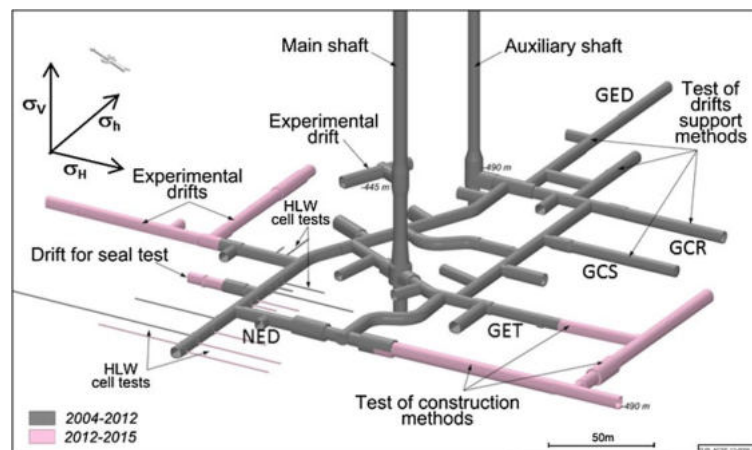


**Figure I .1:** Meuse/Haute-Marne URL drifts network [Armand et al., 2014]

Drifts in the main level can be divided into two different types. One is excavation along with the horizontal major stresses, and the other is excavation along with the minor stresses. The fractures caused by the two different types of excavation are completely different. And this part will be presented in Chapter V .

As shown in Figure I .2, the vertical plan of the geological layers near the URL is presented. The clayey rocks can be found at depths of 417.29m to 508m with a thickness of at least 90m. And the main mineral types can also be seen in this figure.

Numerous *in situ* experiments have shown that clayey rocks in geo-environment are not perfectly homogeneous materials and exhibit inherent anisotropic characteristics. It can also be seen in Figure I .2 that the mineral content of the clayey rocks varies with depth. And the  $\gamma$ -Ray also changes with depth.

## 1.2 Macroscopic behavior of inherently anisotropic clayey rocks under hydro-mechanical coupling

The properties of geo-materials have been investigated by many researchers and many valuable experimental research results have been obtained. As shown in Figure I .3, Abou-Chakra Guéry [2007] shows the pattern of compressive strength and elastic Young's modulus with depth. From this figure, it can be seen that the peak strength tends to decrease with depth, especially in the clay-rich layer of about 490m, where the peak strength is around 16MPa. Young's modulus tends to increase with depth. As can be seen from Figure I .2, geo-materials at different depths have different mineral compositions. Therefore, the variation of the peak strength and Young's modulus with depth indicates that the mineral composition affects the mechanical properties of the geo-material.

On the other hand, geo-materials in complex underground environments, such as clay-rich rocks, cannot be considered in terms of homogeneous, isotropic material theory due to the variety of environmental factors. Figure I .4 shows the different experimental results [Zhang et al., 2019] on the variation of mechanical strength of clayey rocks with the loading orientation. As shown in these figures, the strength of rock reaches its maximum value when the loading direction is parallel or perpendicular to the bedding plane ( $\theta = 0^\circ$  or  $\theta = 90^\circ$ ). The strength of rock reaches its minimum value when  $\theta = 30^\circ$  to  $60^\circ$ . Where the  $\theta$  represents the angle between the load orientation and the bedding plane. Actually, there are many such experimental results have been obtained (e.g., [Al-Harathi, 1998, Alliro et al., 1979, Liu et al., 2018a, Niandou et al., 1997]). Besides, it's worth noting that the peak strength of  $\theta = 0^\circ$  and  $\theta = 90^\circ$  are not exactly the same. This is also due to the anisotropic behavior of the geo-materials.

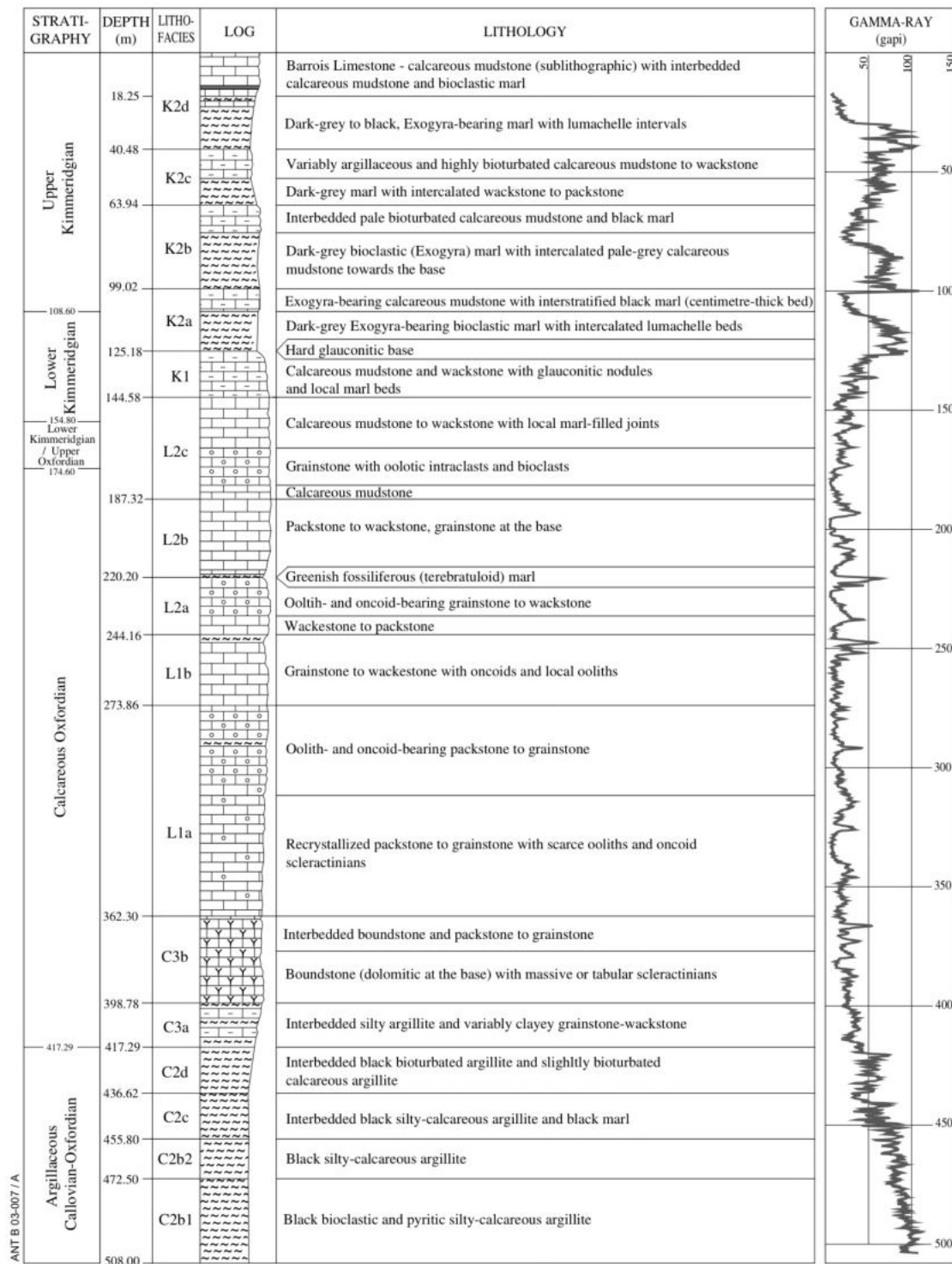
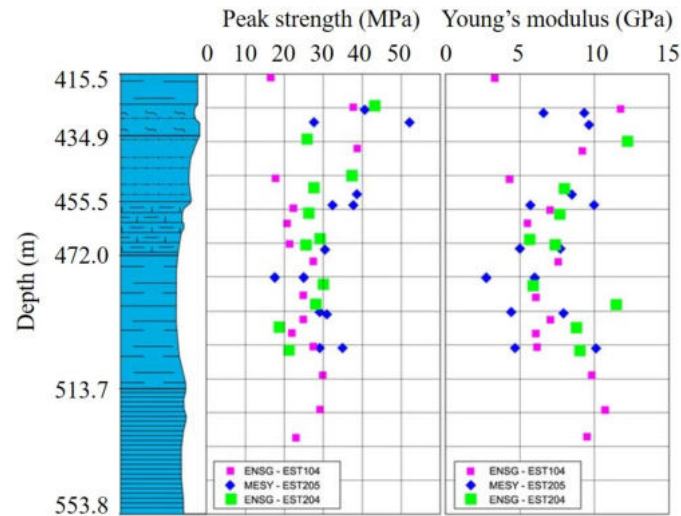
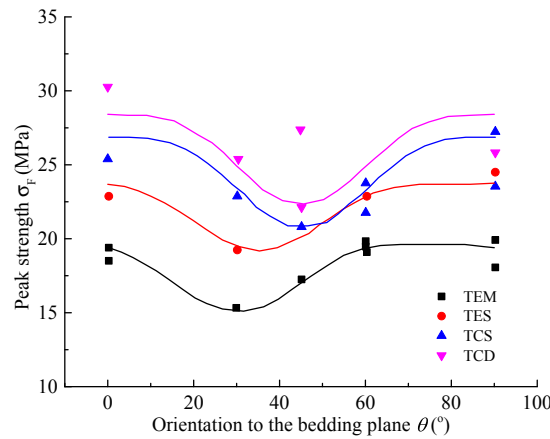


Figure I .2: Geological layer distribution in borehole EST205 [Gaucher et al., 2004]



**Figure I .3:** Compressive strength and Young’s modulus of geomaterials vary with depth [Abou-Chakra Guéry, 2007]



**Figure I .4:** Peak strength changes with loading orientation [Zhang et al., 2019]

Geo-materials in the deep underground have a complex structure, and their anisotropy is mainly influenced by the texture and structure of the principal rock-forming minerals [Ullemeyer et al., 2006]. Singh et al. [1989] provided anisotropic parameters for different types of anisotropic rocks to reflect the degree of anisotropy of rocks, as shown in Table I .1. And according to Bagheripour et al. [2011], there are three main reasons for the anisotropy of geo-materials as follows:

(1) Minerals inside the geo-materials have an irregular shape in their natural state. This may be due to the natural orientation caused by their flat/long surfaces. The random

distribution of these mineral particles gives them different mechanical properties;

(2) As a result of sedimentation over time, such as clayey rocks, shale or sandstone, it exhibits a layered structure. This structure will make the rock anisotropic. On the other hand, different layers or different minerals with different grain sizes will also cause their mechanical anisotropy;

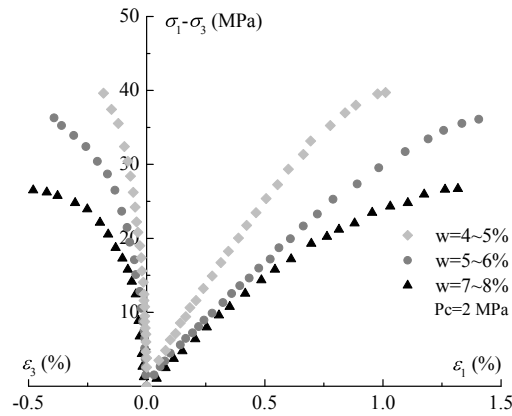
(3) Anisotropy of rock is caused by geological activity and other reasons. For example, the volcanic magma eruption can form anisotropic rocks. The distribution of pores inside the rock matrix can cause anisotropy as well.

anisotropic ratio	class	type of rock
$> 1.0 \cap < 1.1$	isotropic	sandstone
$> 1.1 \cap < 2.0$	slightly anisotropic	sandstone, argillite
$> 2.0 \cap < 4.0$	anisotropic	argillite, slate, phyllite
$> 4.0 \cap < 6.0$	strongly anisotropic	slate, phyllite
$> 6.0$	very strongly anisotropic	slate, phyllite

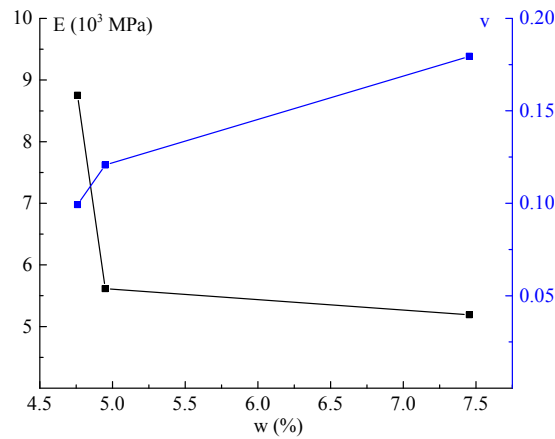
**Table I .1:** Anisotropic ratio of different anisotropic rocks [Singh et al., 1989]

Further, the hydro-mechanical coupling behavior is also an important factor affecting the mechanical properties of the clayey rocks. Numerous experimental studies [Chiarelli, 2000, Hoxha and Auvray, 2004, Pham, 2006, Zhang et al., 2007] have shown that there are three main effects of hydraulic action on clayey rocks, as follows: First, the hydraulic behavior affects the elastic modulus (i.e., Young's modulus and Poisson's ratio) of clayey rocks; Second, the hydraulic behavior affects the transition point of clayey rocks from elastic to plastic deformation; and Finally, the hydraulic behavior affects the compressive and tensile strength of clayey rocks.

As shown in Figure I .5(a), the peak strength of the clayey rocks gradually decreases as the water content increases. The effective Young's modulus of samples with water content equal to 7 ~ 8% is smaller than that of samples with water content equal to 4 ~ 5% and 5 ~ 6%. And it is also clear from this figure that the transition point from elastic to plastic deformation is smaller at water content  $w = 7 \sim 8\%$  than at  $w = 4 \sim 5\%$  and  $w = 5 \sim 6\%$  conditions. Also, the volume deformation under high water content content conditions is smaller under the same stress conditions.



(a) Stress-strain curves

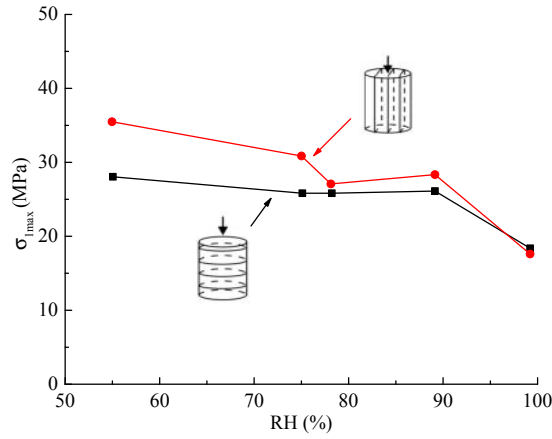


(b) Evolution of Young's modulus and Poisson's ratio

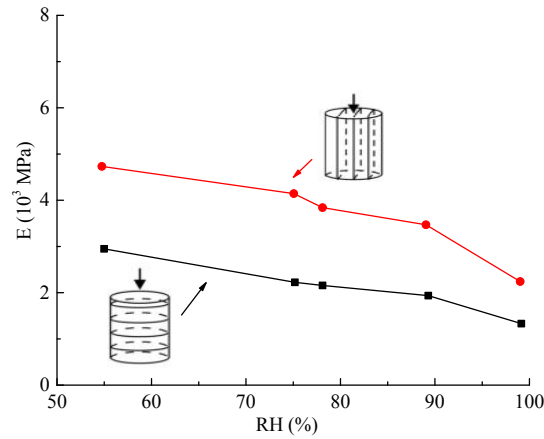
**Figure I .5:** Triaxial compression tests for clayey rocks under different water content [Chiarelli et al., 2003]

The Figure I .5(b) shows the evolution of the corresponding Young's modulus and Poisson's ratio for clayey rocks at different water contents. The confining pressure for these tests are equal to 2MPa. Young's modulus decreases significantly when the water content is lower than 5%, and the rate of decline decreases when the water content is higher than 5%. Similarly, Poisson's ratio increases with increasing water content, and increases significantly when the water content is less than 5%, and the rate of increase of Poisson's ratio gradually decreases when the water content exceeds 5%. This indicates that at low water content, the water content has a greater influence on the mechanical properties of clayey rocks. This is mainly due to the effect of hydraulic on the internal structure of the rock during the loading process.

Zhang et al. [2012] also found that the mechanical properties of clayey rocks are strongly influenced by water saturation and loading orientation, as shown in Figure I .6.



(a) Peak strength



(b) Young's modulus

**Figure I .6:** Evolution of Young's ratio and strength with different orientation and humidity

It can be seen from Figure I .6(a), the peak strength of the load direction parallel to the bedding plane is greater than the strength of the load direction perpendicular to the bedding plane under the low humidity conditions. This difference gradually disappears as the humidity increases. Young's modulus also gradually decreases with increasing humidity, and there exist differences between the different loading directions, as shown in Figure I .6(b).

As mentioned above, when studying the mechanical behavior of clayey rocks, it is

often necessary to consider their hydro-mechanical coupled properties due to the presence of groundwater and anisotropy. In unsaturated clayey rocks, the capillary pressure (i.e., negative pore pressure) will be involved. It is mainly due to the surface tension present at the pore surface. As the water content or relative humidity of the clayey rocks decreases, the capillary force increases accordingly.

In addition, the permeability of geo-materials is also an essential parameter for their mechanical properties, as it can be used to reflect the development of fractures inside the rock. In the case of low permeability materials, it is difficult to measure the permeability due to the low flow rate inside the rock. *In situ* permeability measurement methods include, for example, the constant level measuring system, Slug Test, and pumping wells. Plenty of experimental tests are performed in the laboratory. Many studies [Armand et al., 2017a, Enssle et al., 2011, Menaceur et al., 2015] have found that there exist differences in permeability parallel and perpendicular to the bedding plane. The difference in permeability along the two directions indicates that the development of fractures inside the rocks is heterogeneous.

### 1.3 Micro-mesoscopic properties of inherently anisotropic clayey rocks

Clayey rocks exhibit anisotropic characteristics at the macroscopic scale, which are directly related to their microstructure. As described in the previous sections, at the mesoscopic scale, the clayey rocks are considered to be composed of clay matrix and mineral particles, where the clay matrix consists of solid clay phase and pores at microscopic scales. The shape and size of mineral particles and pores were found to be non-uniform, and their distribution in the subsurface was not completely uniform. Therefore, this factor can lead to the anisotropic characteristic of the clayey rocks.

As shown in Figure I .7, Robinet [2008] provides the distribution of the mineral particles inside the clayey rocks. And this sample was drilled at 439m in the COx argillite layer. As can be seen from this figure, the shape and distribution of the minerals are irregular. Besides, the clay matrix shown in this figure has some voids inside, which are not interconnected. The existence of these voids will provide space for the storage and transport of groundwater.

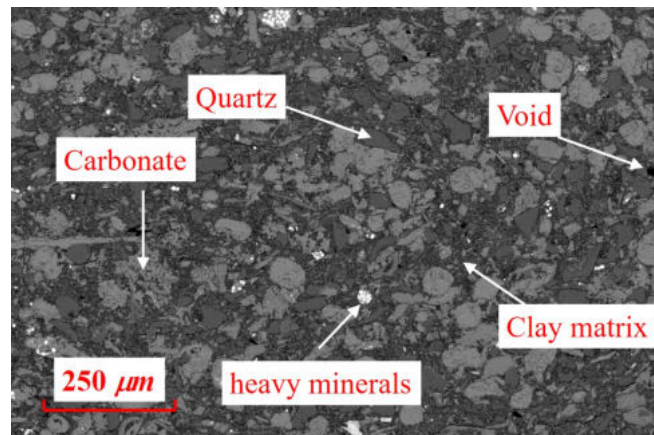


**Figure I .7:** Mineral distribution image from SEM [Robinet, 2008]

Figure I .8 illustrates the variation of mineralogical composition depth from 423m to 503m. The experimental data were measured in a vertical borehole, which 12.7km away from the URL. It can be seen that the carbonate decreases with the depth, while the clay matrix increases with the depth. And it can also be seen from this figure that when the depth range from 540m to 620m, the mineral grains account for about 40% of the total volume, and the clay matrix accounts for about 60% of the total volume. For clayey rocks, the mineral composition exhibits a non-uniform distribution with depth, which leads to variations in macroscopic physical and mechanical properties of clayey rocks with depth.

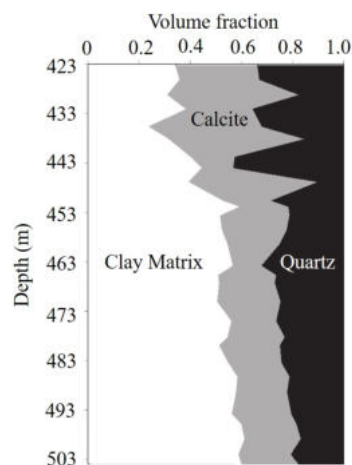
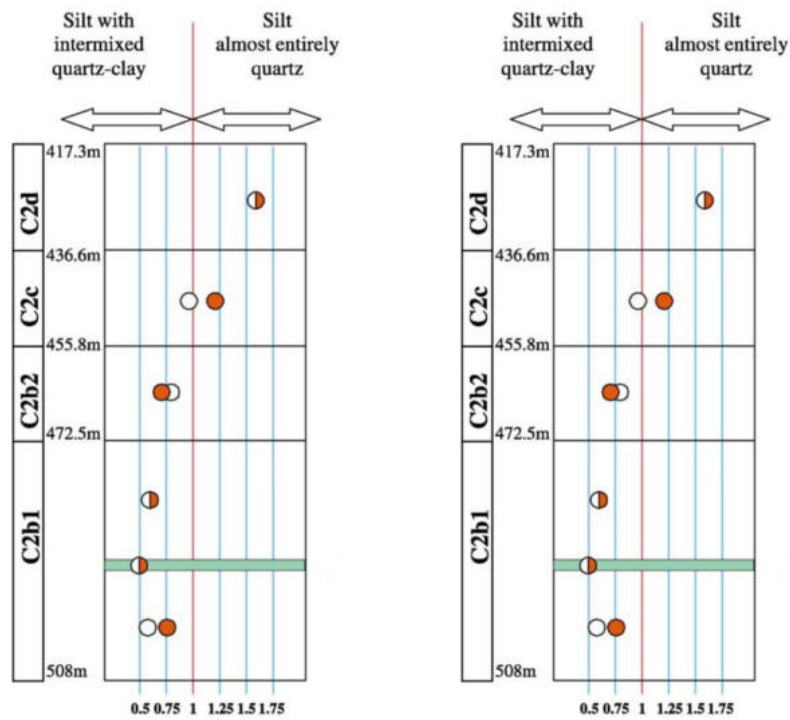
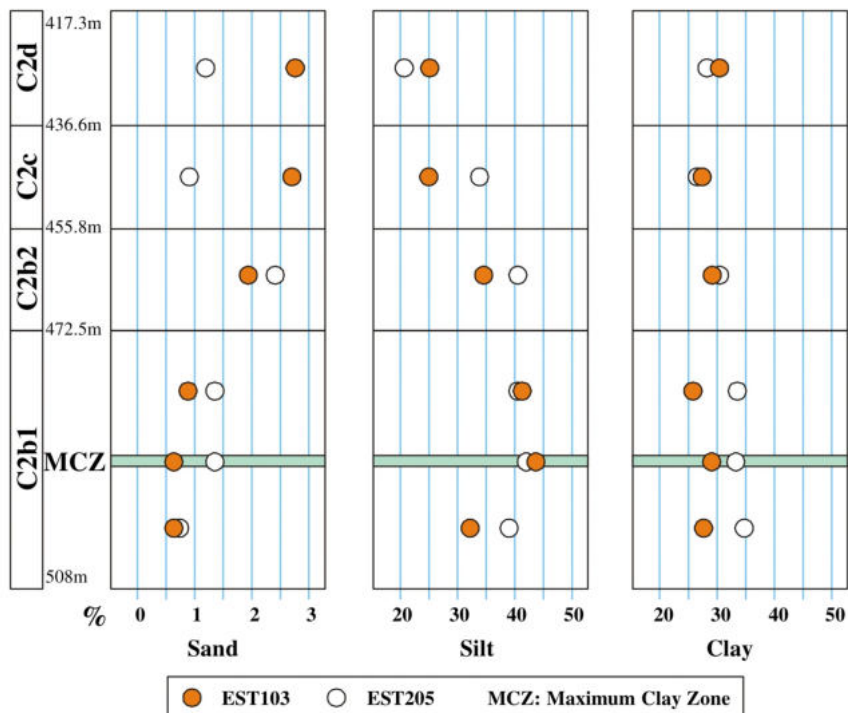


**Figure I .8:** Mineralogical composition changes with depth [Guéry et al., 2010]



(a) Variation of quartz content

(b) Variation of coarseness



(c) Distribution of rock composition

Figure I .9: Rock composition changes with depth [Gaucher et al., 2004]

Gaucher et al. [2004] analyzed the rock composition of the clay-rich layer, including mineral composition, porosity, and density, and its depth ranges from 417m to 508m through two 510m boreholes (i.e., EST205 and EST103) drilled by ANDRA. The Figure I .9 shows material composition distribution and particle size distribution of the clay-rich layer. In Figure I .9(a), the ratio of the horizontal axis satisfies the equation:  $ratio = (quartz + feldspar)/silt$ , showing the comparison of the mineral particles (in this case, mainly quartz) with the total silt content. And one can see that the quartz content is enriched sharply at depths less than 445m.

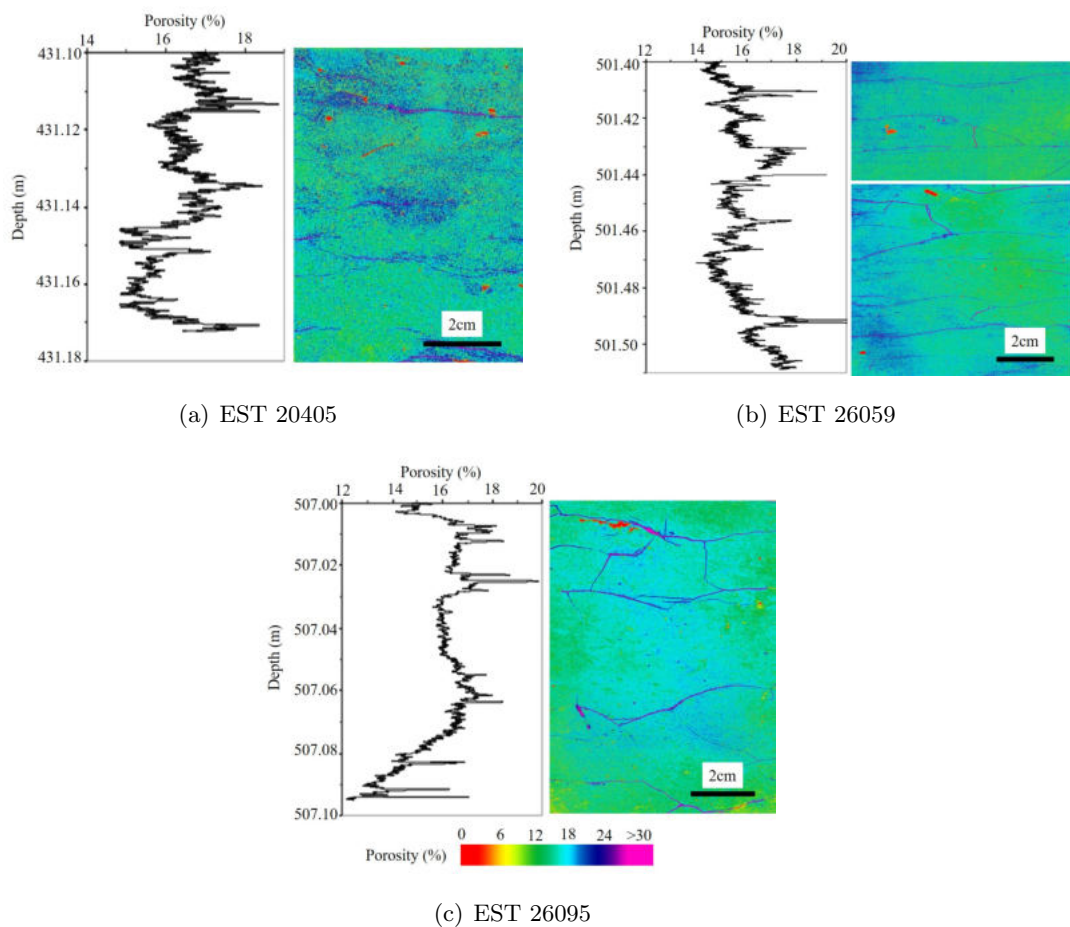


**Figure I .10:** Pore distribution of the claystone varies with depth [Robinet, 2008]

And in Figure I .9(b) shows that the mineral particles are getting finer when the depth is less than 445m, and the ratio on the horizontal axis satisfies the equation:  $ratio = clay\ minerals / (< 4\mu m\ particles\ size)$ . Figure I .9(c) shows that the content of sand decreases with depth. And the silt content increases with depth at a depth of less than 485.97m and decreases with depth at a depth of greater than 489.11m. The content of

clay varies slightly with increasing depth.

Besides, the distribution of pores inside the rock also causes the complex geological environment of the clay-rich layers. It is assumed that the gas in the pores (unsaturated solids) is infinitely compressible. Therefore, the pore distribution will affect the mechanical properties of clayey rocks.

Robinet [2008] found that the pores are mainly located inside the clay matrix and that these pores are very small relative to the size of the mineral grains. Pieces of literature have shown that the porosity of clayey rocks is estimated to be 15% to 20%. Figure I .10 shows the results of scanning electron micrographs (SEM) and porosity variation curves for three claystone specimens (i.e., EST21405, EST20659, and EST26095) corresponding to depths ranging from  $-431.10\text{m}$  to  $-507.10\text{m}$ . These test results are available from Robinet [2008].

Figure I .11 is obtained from Andra [2005a] and shows the pore size distribution curve for clayey rocks. It illustrates that most of the pore sizes is  $20\text{nm}$ , and the second one is around  $3 \sim 4\text{nm}$ . This small average pore diameter is one of the reasons for the low permeability of the claystone.

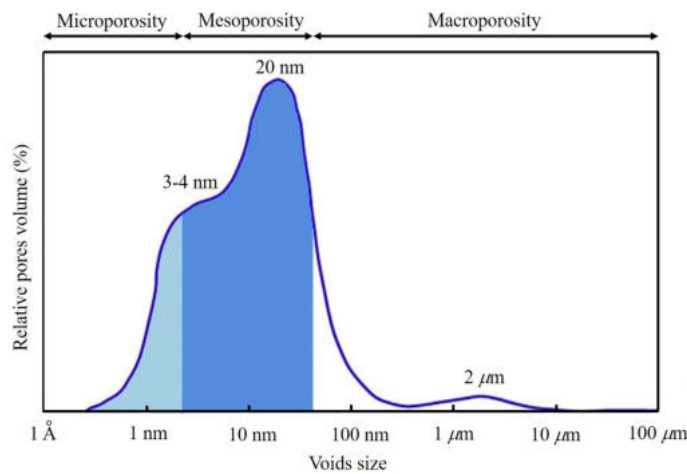


**Figure I .11:** Pore size distribution of the COx argillite [Andra, 2005a]

## 2 Mechanical behavior of the anisotropic material

For linear elastic materials, the stress can be calculated by a linear constitutive equation, as shown in Equation I .1.

$$d\boldsymbol{\sigma} = \mathbb{C} : d\boldsymbol{\varepsilon} \quad (\text{I .1})$$

where  $d\boldsymbol{\sigma}$  and  $d\boldsymbol{\varepsilon}$  denote the stress and strain increments.  $\mathbb{C}$  represents the stiffness tensor of the material. The flexibility matrix  $\mathbb{S}$  is the inverse tensor of the stiffness matrix  $\mathbb{C}$ , which is also frequently encountered in later chapters. The stress  $\boldsymbol{\sigma}$  and strain  $\boldsymbol{\varepsilon}$  in different direction are contained within the stress vector  $\sigma_i$  and strain vector  $\varepsilon_j$ :

$$\begin{aligned}\sigma_i &= [\sigma_x, \sigma_y, \sigma_z, \sigma_{xy}, \sigma_{yz}, \sigma_{zx}]^\top \\ \varepsilon_j &= [\varepsilon_x, \varepsilon_y, \varepsilon_z, \varepsilon_{xy}, \varepsilon_{yz}, \varepsilon_{zx}]^\top\end{aligned}\quad (\text{I.2})$$

Due to the symmetry of stress and strain in space (i.e.,  $\sigma_{xy} = \sigma_{yx}$ ,  $\sigma_{xz} = \sigma_{zx}$ ,  $\sigma_{yz} = \sigma_{zy}$ ,  $\varepsilon_{xy} = \varepsilon_{yx}$ ,  $\varepsilon_{xz} = \varepsilon_{zx}$ ,  $\varepsilon_{yz} = \varepsilon_{zy}$ ), the stiffness matrix  $\mathbb{C}$  and flexibility matrix  $\mathbb{S}$  can be characterized by 36 dependent components in the general form satisfying  $C_{ijkl} = C_{jikl}$  and  $C_{ijkl} = C_{ijlk}$ . The general form of the stiffness matrix  $\mathbb{C}$  can be written as:

$$C_{ijkl} = \begin{bmatrix} C_{1111} & C_{1122} & C_{1133} & \sqrt{2}C_{1123} & \sqrt{2}C_{1113} & \sqrt{2}C_{1112} \\ C_{2211} & C_{2222} & C_{2233} & \sqrt{2}C_{2223} & \sqrt{2}C_{2213} & \sqrt{2}C_{2212} \\ C_{3311} & C_{3322} & C_{3333} & \sqrt{2}C_{3323} & \sqrt{2}C_{3313} & \sqrt{2}C_{3312} \\ \sqrt{2}C_{2311} & \sqrt{2}C_{2322} & \sqrt{2}C_{2333} & 2C_{2323} & 2C_{2313} & 2C_{2312} \\ \sqrt{2}C_{1311} & \sqrt{2}C_{1322} & \sqrt{2}C_{1333} & 2C_{1323} & 2C_{1313} & 2C_{1312} \\ \sqrt{2}C_{1211} & \sqrt{2}C_{1222} & \sqrt{2}C_{1233} & 2C_{1223} & 2C_{1213} & 2C_{1212} \end{bmatrix}\quad (\text{I.3})$$

The flexibility matrix  $\mathbb{S}$  is similar to the stiffness matrix. The anisotropic materials at the macroscopic scale include the following three common types, which can be found in Figure I.12:

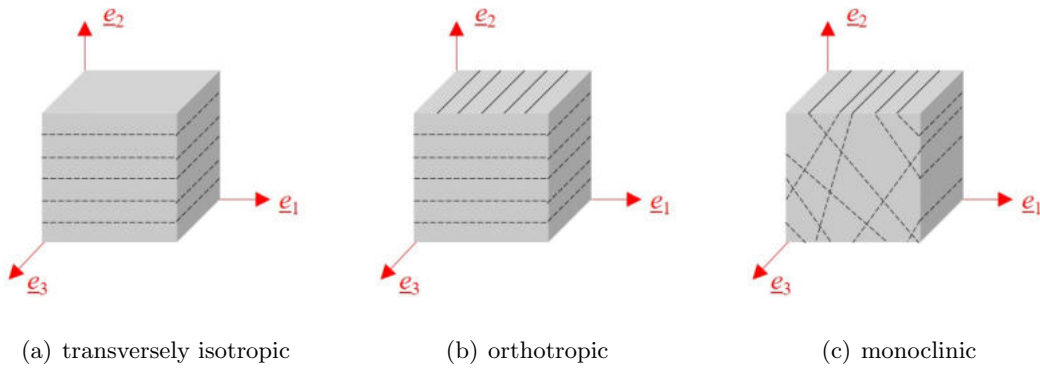


**Figure I.12:** Three typical structural models of anisotropic materials

The first material structural model in Figure I.12(a) is symmetrical in terms of spatial coordinate axis (i.e.,  $\underline{e}_2$ ). This type of material is more common in sedimentary rocks, such as the clayey rocks, which will be analyzed in the following sections. When the load

direction has an angle with the axis of symmetry  $\underline{e}_2$  of the material, a coordinate transformation method is generally required. It will correspond to the transformation matrix  $\tilde{\mathbb{A}}$ , as shown in Equation (I .4). And this structural model is relatively easier to analyze than the other types of structure. The orthotropic material in Figure I .12(b) is a material in which there are two orthogonal planes of symmetry. Their physical and mechanical properties will change when the instrument is measured in different orientations. The third type concerns the monoclinic material. This type is complex and has an axis of symmetry and a perpendicular plane, as shown in Figure I .12(c).

In Voigt notation, the transformation matrix  $\tilde{\mathbb{A}}$  can be expressed as a  $6 \times 6$  tensor, given as follows:

$$\tilde{\mathbb{A}} = \begin{bmatrix} A_{11}^2 & A_{12}^2 & A_{13}^2 & A_{12}A_{13} & A_{11}A_{13} & A_{11}A_{12} \\ A_{21}^2 & A_{22}^2 & A_{23}^2 & A_{22}A_{23} & A_{21}A_{23} & A_{21}A_{22} \\ A_{31}^2 & A_{32}^2 & A_{33}^2 & A_{32}A_{33} & A_{31}A_{33} & A_{31}A_{32} \\ 2A_{21}A_{31} & 2A_{22}A_{32} & 2A_{23}A_{33} & A_{22}A_{33} + A_{23}A_{32} & A_{21}A_{33} + A_{23}A_{31} & A_{21}A_{32} + A_{22}A_{31} \\ 2A_{11}A_{31} & 2A_{12}A_{32} & 2A_{13}A_{33} & A_{12}A_{33} + A_{13}A_{32} & A_{11}A_{33} + A_{13}A_{31} & A_{11}A_{32} + A_{12}A_{31} \\ 2A_{11}A_{21} & 2A_{12}A_{22} & 2A_{13}A_{23} & A_{12}A_{23} + A_{13}A_{22} & A_{11}A_{23} + A_{13}A_{21} & A_{11}A_{22} + A_{12}A_{21} \end{bmatrix} \quad (\text{I .4})$$

Therefore, the stiffness tensor  $\underline{\mathbb{C}}$  for considering matrix transformations can be expressed as follows:

$$\underline{\mathbb{C}} = \tilde{\mathbb{A}}^T : \underline{\mathbb{C}} : \tilde{\mathbb{A}} \quad (\text{I .5})$$

In fact, the geo-materials in nature also include approximately isotropic materials (assumed to be isotropic materials) and rock materials that have no axis of symmetry. As many basic theories are based on isotropic materials, the isotropic materials will also be presented in the third part of this section. Rock materials without an axis of symmetry will not be presented.

## 2.1 Transversely isotropic material

As the studied material in the following chapters is clayey rocks, a detailed analysis of transversely isotropic materials will be presented in this part. In Figure I .12(a), the transversely isotropic material is symmetrical with respect to a certain axis  $\underline{e}_2$ , therefore, a matrix  $\tilde{\mathbb{A}}$  used in Equation I .4 can be written as:

$$\tilde{\mathbb{A}} = \begin{bmatrix} \cos\theta & \sin\theta & 0 \\ -\sin\theta & \cos\theta & 0 \\ 0 & 0 & 1 \end{bmatrix} \quad (\text{I .6})$$

Therefore, the transformation matrix  $\tilde{\mathbb{A}}$  can be written as:

$$\tilde{\mathbb{A}} = \begin{bmatrix} \cos^2\theta & \sin^2\theta & 0 & 0 & 0 & \cos\theta \cdot \sin\theta \\ \sin^2\theta & \cos^2\theta & 0 & 0 & 0 & -\cos\theta \cdot \sin\theta \\ 0 & 0 & 1 & 0 & 0 & 0 \\ 0 & 0 & 0 & \cos\theta & -\sin\theta & 0 \\ 0 & 0 & 0 & \sin\theta & \cos\theta & 0 \\ -2\cos\theta \cdot \sin\theta & 2\cos\theta \cdot \sin\theta & 0 & 0 & 0 & \cos^2\theta - \sin^2\theta \end{bmatrix} \quad (\text{I.7})$$

For transverse isotropic materials, the stiffness matrix is rotated on the  $\underline{e}_2$  axis and the stiffness matrix remains unchanged. So a simplified form of the stiffness matrix is obtained:

$$\mathbb{C} = \begin{bmatrix} C_{1111} & C_{1122} & C_{1133} & 0 & 0 & 0 \\ C_{1122} & C_{2222} & C_{1122} & 0 & 0 & 0 \\ C_{1133} & C_{1122} & C_{1111} & 0 & 0 & 0 \\ 0 & 0 & 0 & 2C_{2323} & 0 & 0 \\ 0 & 0 & 0 & 0 & C_{1111} - C_{1133} & 0 \\ 0 & 0 & 0 & 0 & 0 & 2C_{2323} \end{bmatrix} \quad (\text{I.8})$$

For simplicity, the expression of the stiffness tensor  $\mathbb{C}$  can be expressed in the following way:

$$\begin{aligned} C_{1111} &= C_{3333} = C_{11}, C_{2222} = C_{22}, C_{1313} = C_{55} \\ C_{1122} &= C_{2211} = C_{2233} = C_{3322} = C_{12}, C_{1133} = C_{3311} = C_{13} \\ C_{1212} &= C_{2323} = C_{1221} = C_{2332} = C_{1221} = C_{3223} = C_{2121} = C_{2323} = C_{44} \end{aligned} \quad (\text{I.9})$$

The value of the stiffness matrix can be calculated from the Young's modulus and Poisson's ratio of the material.

$$\begin{aligned} C_{11} &= -\frac{1 - \nu_{21}^2 \frac{\tilde{E}_1}{\tilde{E}_2}}{(1 + \nu_{13}) \left( \frac{2\nu_{21}^2}{\tilde{E}_2} - \frac{1 - \nu_{12}}{\tilde{E}_1} \right)} \\ C_{22} &= -\frac{\tilde{E}_2 \left( \frac{1 - \nu_{13}}{\tilde{E}_1} \right)}{\frac{2\nu_{21}^2}{\tilde{E}_2} - \frac{1 - \nu_{13}}{\tilde{E}_1}} \\ C_{12} &= -\frac{\nu_{21}}{\frac{2\nu_{21}^2}{\tilde{E}_2} - \frac{1 - \nu_{13}}{\tilde{E}_1}} \\ C_{13} &= -\frac{\nu_{13} + \nu_{21}^2 \frac{\tilde{E}_1}{\tilde{E}_2}}{(1 + \nu_{13}) \left( \frac{2\nu_{21}^2}{\tilde{E}_2} - \frac{1 - \nu_{12}}{\tilde{E}_1} \right)} \\ C_{44} &= G_{12} \\ C_{55} &= \frac{C_{11} - C_{13}}{2} \end{aligned} \quad (\text{I.10})$$

The compliance matrix  $\mathbb{S}$  is written as:

$$\begin{aligned} S_{1111} = S_{3333} &= \frac{1}{\tilde{E}_1}, & S_{2222} &= \frac{1}{\tilde{E}_2} \\ S_{1122} &= -\frac{\nu_{21}}{\tilde{E}_2}, & S_{1133} &= -\frac{\nu_{13}}{\tilde{E}_1} \\ S_{1313} &= \frac{1 + \nu_{13}}{2\tilde{E}_1}, & S_{2323} = S_{1212} &= \frac{1}{4G_{12}} \end{aligned} \quad (\text{I .11})$$

where the  $\tilde{E}_1$  and  $\tilde{E}_2$  denote the Young's modulus of transversely isotropic material along the  $\underline{e}_1$  and  $\underline{e}_2$  axes, respectively. The  $\nu_{13}$  and  $\nu_{21}$  are the Poisson's ratio between the  $\underline{e}_1$  and  $\underline{e}_3$  directions and between the  $\underline{e}_1$  and  $\underline{e}_2$  directions, respectively.  $G_{12}$  represents shear modulus. Comparing the Equations I .10 and I .11 reveals that the compliance matrix is simpler, and it will be used frequently in the following chapters.

The Young's modulus and Poisson's ratio along the  $\underline{e}_1$  and  $\underline{e}_2$  are measured by experimental tests in the laboratory.  $\tilde{E}_2$  and  $\nu_{21}$  are determined by uniaxial compression tests which the load along the  $\underline{e}_2$  axis. And the  $\tilde{E}_1$  and  $\nu_{13}$  can be determined by the tests where the load is along the  $\underline{e}_1$  axis. As shown in Figure I .13.

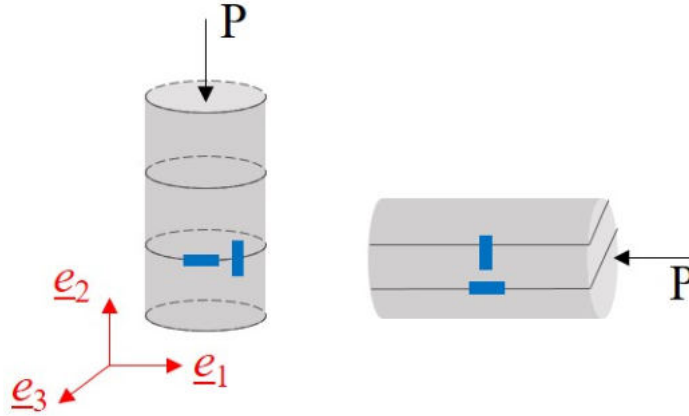


**Figure I .13:** Uniaxial compression tests in different load directions.

## 2.2 Orthotropic materials and Monoclinic materials

Orthotropic materials are often encountered in theoretical analyses. The transversely isotropic material described in the previous section is one of the types of orthotropic materials, as shown in Figure I .12(b), and the transformation matrix  $\tilde{\mathbb{A}}$  can be expressed

as follows:

$$\tilde{\mathbb{A}} = \begin{bmatrix} 1 & 0 & 0 & 0 & 0 & 0 \\ 0 & 1 & 0 & 0 & 0 & 0 \\ 0 & 0 & 1 & 0 & 0 & 0 \\ 0 & 0 & 0 & -1 & 0 & 0 \\ 0 & 0 & 0 & 0 & -1 & 0 \\ 0 & 0 & 0 & 0 & 0 & 1 \end{bmatrix} \quad (\text{I .12})$$

The same method (as shown in Equation I .8) can be used here to simplify the stiffness matrix in Equation I .3 for orthogonal materials.

$$\mathbb{C} = \begin{bmatrix} C_{1111} & C_{1122} & C_{1133} & 0 & 0 & 0 \\ C_{2211} & C_{2222} & C_{2233} & 0 & 0 & 0 \\ C_{3311} & C_{3322} & C_{3333} & 0 & 0 & 0 \\ 0 & 0 & 0 & 2C_{2323} & 0 & 0 \\ 0 & 0 & 0 & 0 & 2C_{3131} & 0 \\ 0 & 0 & 0 & 0 & 0 & 2C_{1212} \end{bmatrix} \quad (\text{I .13})$$

The compliance tensor  $\mathbb{S}$  can be calculated by  $\mathbb{S} = (\mathbb{C})^{-1}$ , and the expression can be written as:

$$\mathbb{S} = \begin{bmatrix} \frac{1}{\bar{E}_1} & \frac{-\nu_{21}}{\bar{E}_2} & \frac{-\nu_{31}}{\bar{E}_3} & 0 & 0 & 0 \\ \frac{-\nu_{12}}{\bar{E}_2} & \frac{1}{\bar{E}_2} & \frac{-\nu_{32}}{\bar{E}_3} & 0 & 0 & 0 \\ \frac{-\nu_{13}}{\bar{E}_3} & \frac{-\nu_{23}}{\bar{E}_2} & \frac{1}{\bar{E}_3} & 0 & 0 & 0 \\ 0 & 0 & 0 & \frac{1}{G_{23}} & 0 & 0 \\ 0 & 0 & 0 & 0 & \frac{1}{G_{31}} & 0 \\ 0 & 0 & 0 & 0 & 0 & \frac{1}{G_{12}} \end{bmatrix} \quad (\text{I .14})$$

For the monoclinic symmetry materials, there is only one plane of material symmetry, as shown in Figure I .12(c). One can consider the case of the monoclinic symmetry with respect to the  $(\underline{e}_1, \underline{e}_2)$  plane. The expression of the transformation matrix is similar to Equation I .12. In addition, considering the symmetry of the monoclinic materials, the relation  $C_{ijkl} = -C_{ijkl}$  can be obtained. According to the contracted notation, one can get:

$$\begin{aligned} C_{1123} &= C_{2311} = C_{2223} = C_{2322} = C_{3323} = C_{2333} = 0 \\ C_{1113} &= C_{1311} = C_{2213} = C_{1322} = C_{3313} = C_{1333} = 0 \\ C_{1223} &= C_{2312} = C_{1213} = C_{1312} \end{aligned} \quad (\text{I .15})$$

Therefore, the stiffness matrix of the monoclinic symmetry materials can be written as:

$$C_{ijkl} = \begin{bmatrix} C_{1111} & C_{1122} & C_{1133} & 0 & 0 & \sqrt{2}C_{1112} \\ C_{2211} & C_{2222} & C_{2233} & 0 & 0 & \sqrt{2}C_{2212} \\ C_{3311} & C_{3322} & C_{3333} & 0 & 0 & \sqrt{2}C_{3312} \\ 0 & 0 & 0 & 2C_{2323} & 2C_{2313} & 0 \\ 0 & 0 & 0 & 2C_{1323} & 2C_{1313} & 0 \\ \sqrt{2}C_{1211} & \sqrt{2}C_{1222} & \sqrt{2}C_{1233} & 0 & 0 & 2C_{1212} \end{bmatrix} \quad (\text{I .16})$$

### 2.3 Isotropic materials

Isotropic materials are the simplest type of material and have the same properties in all directions. Therefore, there is no need to consider the rotation of structural coordinates. The stiffness matrix of the isotropic materials can be written as:

$$C_{ijkl} = \begin{bmatrix} C_{1111} & C_{1122} & C_{1122} & 0 & 0 & 0 \\ C_{1122} & C_{1111} & C_{1122} & 0 & 0 & 0 \\ C_{1122} & C_{1122} & C_{1111} & 0 & 0 & 0 \\ 0 & 0 & 0 & 2C_{2323} & 0 & 0 \\ 0 & 0 & 0 & 0 & 2C_{2323} & 0 \\ 0 & 0 & 0 & 0 & 0 & 2C_{2323} \end{bmatrix} \quad (\text{I .17})$$

The corresponding flexibility matrix can be represented as follows:

$$\mathbb{S} = \begin{bmatrix} \frac{1}{E} & -\frac{\nu}{E} & -\frac{\nu}{E} & 0 & 0 & 0 \\ -\frac{\nu}{E} & \frac{1}{E} & -\frac{\nu}{E} & 0 & 0 & 0 \\ -\frac{\nu}{E} & -\frac{\nu}{E} & \frac{1}{E} & 0 & 0 & 0 \\ 0 & 0 & 0 & \frac{2(1+\nu)}{E} & 0 & 0 \\ 0 & 0 & 0 & 0 & \frac{2(1+\nu)}{E} & 0 \\ 0 & 0 & 0 & 0 & 0 & \frac{2(1+\nu)}{E} \end{bmatrix} \quad (\text{I .18})$$

In general, shear  $k$  and volume modulus  $\mu$  are introduced to represent the stiffness tensor:

$$\mathbb{C} = 3k\mathbb{J} + 2\mu\mathbb{K} \quad (\text{I .19})$$

where  $k = \frac{\tilde{E}}{3(1-2\nu)}$  and  $\mu = \frac{\tilde{E}}{2(1+\nu)}$ .  $\mathbb{J}$  and  $\mathbb{K}$  are fourth-order projections that satisfy:  $\mathbb{J} = \frac{1}{3}\delta_{ij}\delta_{kl}$ ,  $\mathbb{K} = \mathbb{I} - \mathbb{J}$ . The  $\delta_{ij}$  is the Kronecker delta.

## 3 Industrial context and objective of this thesis

Extensive research work has been carried out on clayey rocks, mainly due to their complex structure and relatively stable physical and mechanical properties. For instance, due to

their extremely low permeability, many countries have chosen the hard claystone as a potential geological material for nuclear waste protection. These rocks are characterized by complex mineralogical composition and micro-structure, which has been described in the previous section. In order to study the physical and mechanical properties of clay rocks under multiphysical coupling conditions, a large number of in-situ and laboratory experiments have been carried out. These experiments results are important for analysing the mechanical properties of the clayey rocks at the macroscopic scale.

On the other hand, a number of numerical simulation models have been proposed for clay-rich rocks and the corresponding simulation results have been obtained, including numerical simulations of laboratory tests and structural calculations for underground construction. These numerical simulation models will be presented in the Chapters II and III. However, many of these models for clayey rocks take into account the influence of mineral particles in the clayey rocks on their physics and mechanics, while ignoring the influence of the internal pores inside the clay matrix. In addition, many numerical models haven't considered the anisotropy of clayey rocks and the role of hydro-mechanical coupling in the physical and mechanics of the clayey rocks.

Therefore, the main objective of this thesis is to propose a new constitutive model for describing the elasto-plastic deformation, time-dependent deformation, and the damage in clayey rocks under hydro-mechanical coupling conditions. In order to achieve this objective, the following chapters are organized as follows: Chapter II and Chapter III will present the multi-scale model for calculating the elastic deformation and the plastic-viscoplastic deformation of the clayey rocks, respectively; and Chapters IV and V will show the simulation results of laboratory tests and structure calculations for gallery excavation to verify the correctness of the proposed multi-scale model.

## 4 Conclusions

This chapter focuses on the anisotropy analysis of geo-materials under complex geological conditions. The rock distribution, mineral composition, and pore distribution at a depth of around 490m underground were presented and discussed through extensive literature in this chapter. The effects of hydro-mechanical coupling effects on the physical and mechanical properties of clayey rocks were also presented. In addition, the anisotropic structure of geo-materials, especially the transverse isotropy clayey rocks, was analyzed and illustrated. This chapter was divided into three parts. The first section was a brief introduction to the engineering context of this thesis based on the available literature, focusing on the

CO<sub>x</sub> claystone (one of the nuclear waste repository geomaterials). The anisotropic and hydraulic characteristics of the geomaterial in the actual complex geological environment were presented in terms of the size and distribution of mineral particles and pores and the permeability of the clayey rocks. The second section presented several different anisotropic structures. They are transversely isotropic, orthorhombic, and monoclinic materials. The final section was an introduction to the industrial context and objectives of this thesis.



# Chapter II

## Linear homogenization method considering initial anisotropy and water saturation effect applied to CO<sub>x</sub> claystone

### Contents

---

<b>1</b>	<b>Introduction</b> . . . . .	<b>23</b>
<b>2</b>	<b>Effective elastic property of CO<sub>x</sub> claystone</b> . . . . .	<b>24</b>
2.1	Determination of elastic properties . . . . .	25
2.2	Localization tensor $\mathbb{A}$ . . . . .	27
<b>3</b>	<b>Eshelby's solution for isotropic inclusions</b> . . . . .	<b>29</b>
3.1	Green's function for transversely isotropic matrix . . . . .	30
3.2	Hill's tensor for transversely isotropic matrix . . . . .	32
<b>4</b>	<b>Hydraulic properties of claystone</b> . . . . .	<b>36</b>
<b>5</b>	<b>Conclusions</b> . . . . .	<b>38</b>

---

### 1 Introduction

As discussed in Chapter I , the size and content of mineral particles vary with the depth. The porosity also exhibits a variation in depth. For the clayey rocks, it ranges from about  $-417\text{m}$  to  $-508\text{m}$  underground and has a thickness of about  $90\text{m}$ . It is one of the

geo-materials used as a geological barrier for radionuclides. Its macroscopic properties are strongly influenced by its mineralogy composition [Guéry et al., 2010, Liu et al., 2018a] and porosity conditions. As a common type of sedimentary rock, clayey rocks also contain a layered morphology with parallel bedding planes at the macro- to micro-scale. This generally leads to transversely isotropic behavior at the macroscopic scale [Liu et al., 2015, Niandou et al., 1997, Yang et al., 2013, Zhang et al., 2012]. Therefore, in this chapter, clayey rocks are studied as a transversely isotropic geomaterial, and the influence of mineral particles and pores on their physical and mechanical properties will be considered.

In order to consider the influence of the mineral compositions and pores inside the clayey rocks on their macro-physical mechanics, Eshelby and Hill polarization tensors [Eshelby, 1957] will be introduced in this chapter to establish a link between micro-deformation and macro-deformation.

The purpose of this chapter is to develop a unified micro-mechanics of clayey rocks based constitutive model using the Eshelby and Hill polarization tensors, while also considering the effect of hydro-mechanical coupling effects on their physico-mechanical properties. Therefore, in this chapter, we will first present the macroscopic stress-strain relations of claystone and introduce several different homogenization schemes. Then, the Eshelby and Hill polarization tensors will be introduced, and the Green's function also will be presented. Finally, we will present the hydraulic properties of the clayey rocks.

## 2 Effective elastic property of COx claystone

Clayey rocks are considered to be mixed geological materials consisting of various mineral grains and clay matrix. At the microscopic scale ( $nm \sim \mu m$ ), the clay matrix has many different sized pores (between about  $4nm$  to  $20nm$ ), which are very small compared to the mineral particles. These pores vary with depth. For simplicity, these pores will be considered to be uniformly distributed in the clay matrix for the multiscale anisotropy model. At the mesoscopic scale ( $\mu m \sim cm$ ), the claystone is assumed to be composed of the porous matrix and mineral grains. At the macroscopic scale ( $cm \sim dm$ ), the mixture of porous matrix and mineral grains is considered to be a continuous medium with transverse isotropy. Therefore, a typical simplified Representative Elementary Volume (REV) of clayey rocks is selected and illustrated in Figure II .1.

In generally, different families of mineral particles can be found such as carbonate, quartz, pyrite, etc. For the sake of simplicity, we assume that the different families of

particles are merged into a single inclusion phase, which exhibits a linear elastic behavior. For convenience, let  $\Omega_i$  being the volume of the inclusion phase,  $\Omega_p$  the volume of voids and  $\Omega_s$  that of solid clay phase. The porosity  $f$  and the volumetric fraction of inclusion  $\rho$  are then given by:

$$f = \frac{\Omega_p}{\Omega_s + \Omega_p}, \quad \rho = \frac{\Omega_i}{\Omega_i + \Omega_s + \Omega_p} \quad (\text{II .1})$$

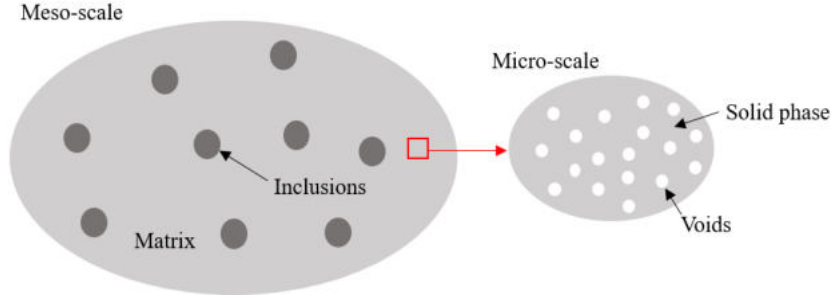


**Figure II .1:** Simplified Representative Elementary Volume (REV) of clayey rocks

## 2.1 Determination of elastic properties

We assume that a macroscopic uniform strain field  $\mathbf{E}$  acts on the boundary of the REV and that the REV achieves equilibrium. The average local stress and strain in the REV can be obtained:

$$\langle \sigma \rangle = \frac{1}{V} \int_V \boldsymbol{\sigma}(z) dz = \boldsymbol{\Sigma}; \quad \langle \varepsilon \rangle = \frac{1}{V} \int_V \boldsymbol{\varepsilon}(z) dz = \mathbf{E} \quad (\text{II .2})$$

where  $V$  denotes the volume of the REV,  $\boldsymbol{\sigma}(z)$  and  $\boldsymbol{\varepsilon}(z)$  denote the local stress and strain for different phases (mainly for the pore matrix and mineral inclusions) corresponding to the position vector  $z$ . The  $\langle \cdot \rangle$  is the average volume of the domain  $\Omega$  for the different phases. The macroscopic stress and macroscopic strain follows a fundamental function:

$$\boldsymbol{\Sigma} = \mathbb{C}^{hom} : \mathbf{E}^e = \mathbb{C}^{hom} : (\mathbf{E} - \mathbf{E}^p) \quad (\text{II .3})$$

where  $\boldsymbol{\Sigma}$  denotes the macroscopic stress tensor,  $\mathbf{E}$  the macroscopic total strain tensor,  $\mathbf{E}^e$  the macroscopic elastic strain tensor and  $\mathbf{E}^p$  the macroscopic plastic strain tensor, which will be mentioned in the next chapter.  $\mathbb{C}^{hom}$  is the macroscopic elastic stiffness tensor. For different phases inside the REV, the local linear elastic constitutive function is satisfied as:

$$\boldsymbol{\sigma}(z) = \mathbb{C}(z) : \boldsymbol{\varepsilon}(z) \quad (\text{II .4})$$

In order to study the mechanical behavior of each phase at the microscopic scale. It is necessary to determine the relations between local strain  $\boldsymbol{\varepsilon}(z)$  (or local stress  $\boldsymbol{\sigma}(z)$ ) and macroscopic strain  $\boldsymbol{E}$  (or macroscopic stress  $\boldsymbol{\Sigma}$ ). Therefore, a localization tensor  $\mathbb{A}$  is introduced to establish a relation between the local strain and macroscopic strain, as shown in following form:

$$\boldsymbol{\varepsilon}(z) = \mathbb{A}(z) : \boldsymbol{E} \quad (\text{II .5})$$

Putting together Equations (II .2), (II .4) and (II .5) delivers the relational equations for the local stiffness tensor of the different phases and macroscopic stiffness tensor.

$$\mathbb{C}^{hom} = \langle \mathbb{C} : \mathbb{A} \rangle \quad (\text{II .6})$$

The clayey rocks, which contain the pore matrix and mineral inclusions. The effect elastic stiffness tensor  $\mathbb{C}^{hom}$  is determined by a two-step homogenization. In this study, we adopt the homogenization approach based on the method of Zaoui [2002].

At the microscopic scale, the elastic behavior of the homogeneous porous medium can be expressed in the following way:

$$\boldsymbol{\sigma} = \mathbb{C}^{pm} : \boldsymbol{\varepsilon}^e \quad (\text{II .7})$$

where  $\boldsymbol{\sigma}$  is the averaged stress tensor of the porous medium and  $\boldsymbol{\varepsilon}^e$  the corresponding elastic strain tensor. The homogenized elastic tensor of the porous medium is denoted as  $\mathbb{C}^{pm}$  and is calculated from the following relation [Giraud et al., 2007]:

$$\mathbb{C}^{pm} = \mathbb{C}^s : (\mathbb{I} - f\mathbb{A}^p) \quad (\text{II .8})$$

In this relation,  $\mathbb{I}$  is the fourth rank unit tensor.  $\mathbb{C}^s$  is the elastic tensor of the solid clay phase.  $\mathbb{A}^p$  represents the strain concentration tensor linking the average strain tensor specified on the homogenized porous medium  $\boldsymbol{\varepsilon}$  to the local strain field inside the solid clay phase.

After the effective elastic tensor of porous clay matrix  $\mathbb{C}^{pm}$  is known, the macroscopic elastic tensor  $\mathbb{C}^{hom}$  can be determined in the second homogenization step by considering the effect of the inclusion phase. Again, by using the same method as above, the macroscopic elastic tensor of the homogenized equivalent medium is given by the following relation:

$$\mathbb{C}^{hom} = \mathbb{C}^{pm} + \rho (\mathbb{C}^i - \mathbb{C}^{pm}) : \mathbb{A}^i \quad (\text{II .9})$$

where  $\mathbb{C}^i$  is the isotropic elastic tensor of the merged inclusion phase.  $\mathbb{A}^i$  is the strain concentration tensor relating the local strain tensor of the inclusion phase to the macroscopic strain tensor.

## 2.2 Localization tensor $\mathbb{A}$

For the Equations II .8 and II .9, the most important thing is to determine the localization tensor  $\mathbb{A}$ . In this section, two widely used schemes will present: the Dilute scheme and the Mori-Tanaka scheme.

### 2.2.1 Dilute scheme

The Dilute scheme is a relatively simple form. The Dilute scheme is mainly used in cases where the mineral particles inside the material are small and relatively sparsely distributed. As mentioned above, this chapter does not distinguish between the different types of minerals and treats them as a single mineral phase. These mineral particles are assumed to have a uniform ellipsoidal shape and their stiffness tensor is denoted by  $\mathbb{C}_i$ . If it is assumed that the mineral particles inside the material are small enough that they have sufficient distance with other mineral particles. The interactions between the mineral particles will not be taken into account.

The localization tensor  $\mathbb{A}^i$  can be written as following form [Eshelby, 1957]:

$$\mathbb{A}^i = (\mathbb{I} + \mathbb{P}^i : (\mathbb{C}^i - \mathbb{C}^{pm}))^{-1} \quad (\text{II .10})$$

where the  $\mathbb{P}^i$  is the fourth-order Hill's tensor for the inclusion-reinforced composite. The components of  $\mathbb{P}^i$  depend on the shape and orientation of inclusions and the elastic properties of porous clay matrix  $\mathbb{C}^{pm}$ .

At the microscopic scale, the porous clay matrix is viewed as consisting of pores and clay particles. For the Dilute scheme, it is assumed that the pores inside the clay matrix are particularly small and uniformly distributed in the clay matrix. Therefore, we assume there is no interaction between the different pores. Similar to the Equation II .10, but here the stiffness tensor of pores is considered to be zero. The localization tensor  $\mathbb{A}^p$  can be expressed as follows:

$$\mathbb{A}^p = (\mathbb{I} - \mathbb{P}^p : \mathbb{C}^s)^{-1} \quad (\text{II .11})$$

where  $\mathbb{P}^p$  represents the Hill tensor of the porous medium. Similar to  $\mathbb{P}^i$ , the components of  $\mathbb{P}^p$  are influenced by the shape and orientation of voids and the elastic properties of solid clay phase  $\mathbb{C}^s$ .

Putting the Equations II .10 and II .11 into the Equations II .9 and II .8, respectively, the macroscopic elastic tensor  $\mathbb{C}^{hom}$  and elastic tensor of the porous medium  $\mathbb{C}^{pm}$  can be obtained:

$$\begin{cases} \mathbb{C}^{hom} = \mathbb{C}^{pm} + \rho (\mathbb{C}^i - \mathbb{C}^{pm}) : (\mathbb{I} + \mathbb{P}^i : (\mathbb{C}^i - \mathbb{C}^{pm}))^{-1} \\ \mathbb{C}^{pm} = \mathbb{C}^s : \left( \mathbb{I} - f (\mathbb{I} - \mathbb{P}^p : \mathbb{C}^s)^{-1} \right) \end{cases} \quad (\text{II .12})$$

### 2.2.2 Mori-Tanaka scheme

In general, the inclusions are not completely isolated inside the clay matrix. The interaction between the different inclusions should be considered. This section will propose the effective stiffness tensor using Mori-Tanaka scheme based on the Mori-Tanaka method [Mori and Tanaka, 1973].

Considering the existence of interactions between the different inclusions, an intermediate prescribed macroscopic strain  $\mathbf{E}^\infty$  is introduced at the external boundary of the REV. The local strain of inclusion is written as follows:

$$\boldsymbol{\varepsilon}^i = \mathbb{A}^i : \mathbf{E}^\infty = (\mathbb{I} + \mathbb{P}^i : (\mathbb{C}^i - \mathbb{C}^{pm}))^{-1} : \mathbf{E}^\infty \quad (\text{II .13})$$

In addition, according to the average condition in Equation II .2, the relations between the intermediate prescribed macroscopic strain  $\mathbf{E}^\infty$  and macroscopic strain  $\mathbf{E}$  can be written as:

$$\mathbf{E}^\infty = \left[ (1 - \rho)\mathbb{I} + \rho (\mathbb{I} + \mathbb{P}^i : (\mathbb{C}^i - \mathbb{C}^{pm}))^{-1} \right]^{-1} : \mathbf{E} \quad (\text{II .14})$$

Substitution the Equation II .14 into the Equation II .13 derives the expression for the localization tensor  $\mathbb{A}^i$ :

$$\mathbb{A}^i = (\mathbb{I} + \mathbb{P}^i : (\mathbb{C}^i - \mathbb{C}^{pm}))^{-1} : \left[ (1 - \rho)\mathbb{I} + \rho (\mathbb{I} + \mathbb{P}^i : (\mathbb{C}^i - \mathbb{C}^{pm}))^{-1} \right]^{-1} \quad (\text{II .15})$$

where  $\mathbb{P}^i$  has the same meaning as that expressed in the Equation II .10. Again, the expression of  $\mathbb{A}^p$  depends on the elastic tensor of the solid clay phase, while the elastic tensor of the void is assumed to be zero. And we can derive the expression of the strain concentration tensor  $\mathbb{A}^p$  with:

$$\mathbb{A}^p = (\mathbb{I} - \mathbb{P}^p : \mathbb{C}^s)^{-1} : \left[ (1 - f)\mathbb{I} + f (\mathbb{I} - \mathbb{P}^p : \mathbb{C}^s)^{-1} \right]^{-1} \quad (\text{II .16})$$

where the components of  $\mathbb{P}^p$  depend on the shape and orientation of the voids and the elastic properties of the solid clay phase, as indicated by  $\mathbb{P}^p$  in Equation II .11.

Putting Equations II .15 and II .16 into Equations II .9 and II .8, respectively, the macroscopic effective elastic tensor  $\mathbb{C}^{hom}$  and effective elastic tensor of porous medium  $\mathbb{C}^{pm}$  corresponding to the Mori-Tanaka scheme can be given by the following equation:

$$\begin{cases} \mathbb{C}^{hom} = \mathbb{C}^{pm} + \rho (\mathbb{C}^i - \mathbb{C}^{pm}) : (\mathbb{I} + \mathbb{P}^i : (\mathbb{C}^i - \mathbb{C}^{pm}))^{-1} : \left[ (1 - \rho)\mathbb{I} + \rho (\mathbb{I} - \mathbb{P}^p : \mathbb{C}^s)^{-1} \right]^{-1} \\ \mathbb{C}^{pm} = \mathbb{C}^s : \left( \mathbb{I} - f (\mathbb{I} - \mathbb{P}^p : \mathbb{C}^s)^{-1} \right) : \left[ (1 - f)\mathbb{I} + f (\mathbb{I} - \mathbb{P}^p : \mathbb{C}^s)^{-1} \right]^{-1} \end{cases} \quad (\text{II .17})$$

For the calculation of the effective elastic tensor, there are other widely used schemes, such as the Self-consistent scheme [Fassi-Fehri et al., 1989] and the PCW model [Castañeda

and Willis, 1995]. These different schemes consider different types of geomaterials, mainly their mineral particle distribution and microstructure.

In this chapter, the Mori-Tanaka scheme is chosen to calculate the macroscopic effective elastic tensor  $\mathbb{C}^{hom}$  and the effective elastic tensor of porous medium  $\mathbb{C}^{pm}$ . As can be seen from Figure I .7, the proportion of minerals in the claystone is not low, and the volume fraction of mineral inclusions is about 40% according to laboratory experiments, which can be presented in Chapter I of this thesis. As can also be seen from Figure I .9, for the claystone layers (−472.5m to −508m), the quartz content starts to increase (quartz has a relatively large particle size). In addition, Figure I .7 shows that the mineral grains are relatively close to each other. Therefore, it is necessary to take into account the interaction effect of mineral grains under external loading. Therefore, in this chapter, the Mori-Tanaka scheme will be more appropriate. Hill's tensor  $\mathbb{P}$  will be described in the next section.

### 3 Eshelby's solution for isotropic inclusions

As shown in the previous section, we assume that the inclusions are linearly elastic, and the Hill's tensor  $\mathbb{P}^i$  will be easily obtained for the case where the porous clay matrix is isotropic. And the Hill's tensor can be expressed as  $\mathbb{P}^i = \mathbb{S}^E : \mathbb{S}^{pm}$ . The  $\mathbb{S}^E$  and  $\mathbb{S}^{pm}$  represent the Eshelby tensor and compliance tensor of the porous matrix. And the Hill's tensor  $\mathbb{P}^i$  can be given as follows:

$$\begin{aligned} \mathbb{P}^i &= \frac{\alpha}{3k} \mathbb{J} + \frac{\beta}{2\mu} \mathbb{K} \\ \alpha &= \frac{3k}{3k + 4\mu}, \quad \beta = \frac{6(k + 2\mu)}{5(3k + 4\mu)} \end{aligned} \quad (\text{II .18})$$

where the shear and bulk moduli ( $k$  and  $\mu$ ) has been expressed in Equation I .19. The fourth-order projections  $\mathbb{J}$  and  $\mathbb{K}$  can be seen in Chapter I .

In the case of anisotropic porous matrix, the Hill's tensor is not easily determined. In this section, a widely used approach [Mura, 1987, Qi, 2016] is presented by defining an inhomogeneous region  $\Omega^*$  inside the porous matrix. As shown in Figure II .2, the initial heterogeneous porous matrix is divided into two domains, a homogeneous matrix region  $\Omega$  and a heterogeneous matrix region  $\Omega^*$ . The elastic stiffness of the homogeneous matrix is denoted by  $\mathbb{C}_{iso}^{pm}$ , and the stress and strain in this homogeneous region are denoted by  $\boldsymbol{\sigma}_{iso}$  and  $\boldsymbol{\varepsilon}_{iso}$ , respectively. The stress and strain of this inhomogeneity are denoted by  $\boldsymbol{\sigma}_*$  and  $\boldsymbol{\varepsilon}_*$ , respectively.

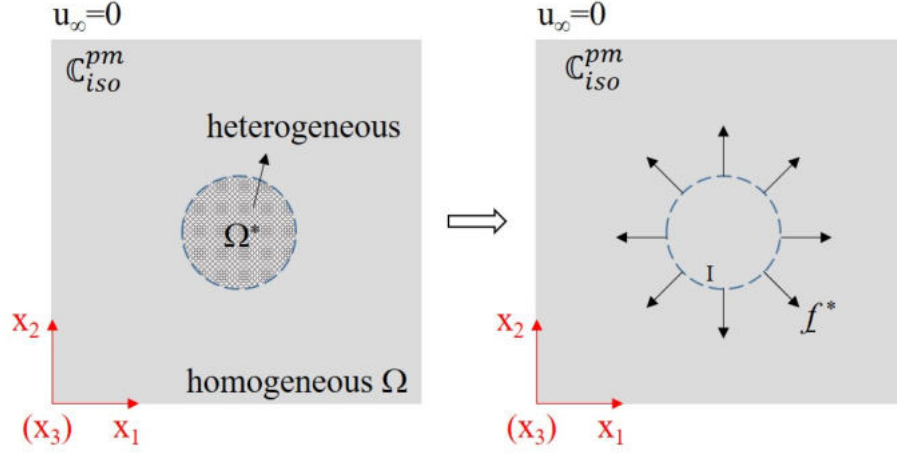


**Figure II .2:** Equivalent problem of anisotropic porous matrix

So the following equations can be obtained:

$$\begin{cases} \sigma_{iso} = \mathbb{C}_{iso}^{pm} : \varepsilon_{iso}, & (X_1, X_2) \in \Omega \\ \sigma_* = \mathbb{C}_{iso}^{pm} : \varepsilon_*, & (X_1, X_2) \in \Omega^* \end{cases} \quad (\text{II .19})$$

For anisotropic materials, the stresses  $\sigma_*$  and  $\sigma_{iso}$  are usually unequal. Therefore, the stresses in the heterogeneous region will affect the surrounding domains. In this section, we can use an equivalent approach. As can be shown in Figure II .2, we assume that an equivalent force  $\underline{f}^*$  is distributed on the boundary surface of the heterogeneous region.

$$\underline{f}^* = -\mathbb{C}_{iso}^{pm} : (\varepsilon_* - \varepsilon_{iso}) \cdot \underline{n}(\partial I) \quad (\text{II .20})$$

where  $\underline{n}$  is a unit vector perpendicular to the boundary surface of the heterogeneous region  $\Omega^*$ .  $\partial I$  is subdomain of the boundary surface of the heterogeneous region.

Since the claystone contains both inclusions and porous matrix, the equivalent treatment of the anisotropic matrix also needs to consider the effect of force  $\underline{f}^*$  on the isotropic inclusions. In this section, Green's function will be introduced to solve this problem.

### 3.1 Green's function for transversely isotropic matrix

The Green's function expresses the displacement at point  $z$  (here the point  $z$  is assumed as an interior-point which inside the elastic inclusion) is induced by a concentrated force  $\underline{f}^*(z')$ . The point  $z'$  here is assumed as an exterior point outside the inclusion. As shown in the following equation:

$$u_i^{int}(z) = G_{ij}(z, z') \cdot f_j^*(z') \quad (\text{II .21})$$

where the subscript in the Equation II .21 denotes the force  $\underline{f}^*$  applied on the point  $z'$  along the  $j$ -direction, which causes displacement components  $u^{int}$  along the  $i$ -direction. When the inclusions are considered to be elliptical shapes, the Equation II .21 can be rewritten in the following form:

$$u_i^{int}(z) = \int_{d\Omega^i} G_{ij}(z, z') \cdot f_j^*(z') (\partial I)^{-1} ds \quad (\text{II .22})$$

where the  $s$  denotes the integral boundary surface of the inclusion  $d\Omega^i$ . The  $\Omega^i$  denotes the ellipsoidal inclusion as seen in Figure II .3.

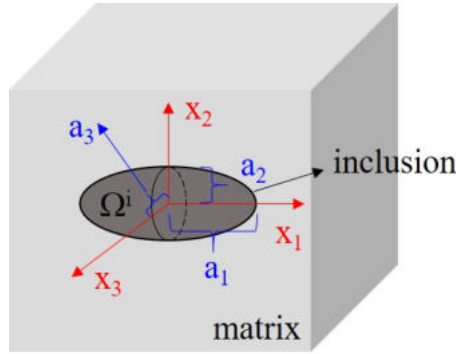


**Figure II .3:** An ellipsoidal inclusion inside the porous matrix

with,

$$\frac{x_1^2}{a_1^2} + \frac{x_2^2}{a_2^2} + \frac{x_3^2}{a_3^2} = 1 \quad (\text{II .23})$$

where  $a_i$  ( $i = 1, 2, 3$ ) denotes the radius of the ellipsoidal inclusion along the three axes.

Putting the Equation II .20 into the Equation II .22, we can get the updated form:

$$\begin{aligned} \underline{u}^{int}(z) &= - \int_{d\Omega^i} \mathbf{G}(z, z') : \mathbb{C}_{iso}^{pm} : (\underline{\varepsilon}_* - \underline{\varepsilon}_{iso}) \cdot \underline{n} ds \\ &= - \frac{\partial}{\partial \underline{n}} \int_{\Omega^i} \mathbf{G}(z, z') d\Omega^i \cdot \mathbb{C}_{iso}^{pm} : (\underline{\varepsilon}_* - \underline{\varepsilon}_{iso}) \end{aligned} \quad (\text{II .24})$$

Therefore, the strain inside the inclusion induced by force  $\underline{f}^*$  can be obtained:

$$\hat{\varepsilon}_{ij}^i = - \frac{\partial}{\partial \underline{n}_k \underline{n}_l} \int_{\Omega^i} G_{ij}(z, z') d\Omega^i : (C_{iso}^{pm})_{klmn} : ((\varepsilon_*)_{mn} - (\varepsilon_{iso})_{mn}) \quad (\text{II .25})$$

In addition, Green's function has two important properties for elastic medium:

$$G_{ij}(x, y) = G_{ij}(x - y) \quad (\text{II .26a})$$

$$G_{ij}(x - y) = G_{ij}(y - x) \quad (\text{II .26b})$$

Therefore, Hill's tensor can be defined in a simple form [Giraud et al., 2007] as follows:

$$P_{ijkl} = - \frac{\partial}{\partial x_k x_l} \left( \int_{\Omega^i} G_{ij}(x - y) dy \right), \quad \forall x \in \Omega^i \quad (\text{II .27})$$

### 3.2 Hill's tensor for transversely isotropic matrix

According to the existing literatures [Mura, 2013, Nemat-Nasser et al., 1996], the Hill's tensor  $\mathbb{P}$  in Equation II .27 can be written in the following form:

$$P_{ijkl}(z) = \frac{1}{4} (M_{kijl}(z) + M_{kjil}(z) + M_{ljik}(z) + M_{ljki}(z)), \quad z \in \Omega^i$$

(II .28)

with

$$M_{ijkl}(z) = -\frac{\partial}{\partial z_l} \int_{\Omega^i} \frac{\partial G_{ij}(z - z')}{\partial z_k} d\Omega^i$$

where the volume integral  $\Omega^i$  can be expressed as a surface integral based on the shape of ellipsoidal inclusion as follows:

$$d\Omega^i = d\Omega^i(r) = drdS = r^2 drd\omega, \quad r = |z' - z|$$

(II .29)

where the point  $z'$  and  $z$  have already been explained above, and they denote the exterior and interior points of inclusion, respectively. The  $d\omega$  denotes the elementary area on the unit ellipsoidal surface. Here, a component  $g_{ijk}$  is introduced to express the derivatives of Green's function [Giraud et al., 2007].

$$g_{ijk}(\underline{\mathbf{l}}) = r^2(\underline{\mathbf{l}}) \frac{\partial}{\partial z_k} G_{ij}(z - z') = -r^2(\underline{\mathbf{l}}) \frac{\partial}{\partial z_k} G_{ij}(r(\underline{\mathbf{l}}))$$

(II .30)

where the unit vector  $\underline{\mathbf{l}}$  is defined as a unit vector from point  $z'$  to point  $z$ :

$$\underline{\mathbf{l}} = \frac{z' - z}{|z' - z|} = (l_1, l_2, l_3)$$

(II .31)

Putting the Equation II .30 into the Equation II .29,  $\mathbb{M}$  can be rewritten as:

$$M_{ijkl}(z) = -\frac{\partial}{\partial z_l} \int_{\Omega^i} r(\underline{\mathbf{l}}) g_{ijk}(\underline{\mathbf{l}}) d\omega$$

(II .32)

The boundary surface of ellipsoidal inclusion  $\Omega^i$  have been expressed by Equation II .23, which can also be written in another form.

$$\frac{(z_1 + rl_1)^2 + (z_3 + rl_3)^2}{a_1^2} + \frac{(z_2 + rl_2)^2}{a_2^2} = 1$$

(II .33)

where  $r(\underline{\mathbf{l}})$  can be shown that:

$$r(\underline{\mathbf{l}}) = -\frac{f}{f_1} + \left( \frac{f^2}{f_1^2} + \frac{e}{f_1} \right)^{1/2}$$

(II .34)

where

$$\begin{aligned} f &= \frac{z_1 l_1 + z_3 l_3}{a_1^2} + \frac{z_2 l_2}{a_2^2} \\ f_1 &= \frac{l_1^2 + l_3^2}{a_1^2} + \frac{l_2^2}{a_2^2} \\ e &= 1 - \left( \frac{z_1^2 + z_3^2}{a_1^2} + \frac{z_2^2}{a_2^2} \right) \end{aligned} \quad (\text{II .35})$$

Combining the Equations II .32 and II .34, the  $\mathbb{M}$  can be updated as follows:

$$M_{ijkl}(z) = \frac{\partial}{\partial z_l} \int_{\Omega^i} \left( \frac{f}{f_1} \right) g_{ijk}(\mathbf{l}) d\omega - \frac{\partial}{\partial z_l} \int_{\Omega^i} \left( \frac{f^2}{f_1^2} + \frac{e}{f_1} \right)^{1/2} g_{ijk}(\mathbf{l}) d\omega \quad (\text{II .36})$$

The latter term in the Equation II .36 can be calculated to be equal to zero, so we get a simpler form:

$$M_{ijkl}(z) = \frac{\partial}{\partial z_l} \int_{\Omega^i} \left( \frac{f}{f_1} \right) g_{ijk}(\mathbf{l}) d\omega \quad (\text{II .37})$$

For simplicity, the inclusion is assumed as an unit sphere. Therefore,  $a_1 = a_2$  in Equation II .33. So, we can get:

$$M_{ijkl}(z) = \frac{\partial}{\partial z_l} \int_{\Omega^i} (z_1 l_1 + z_2 l_2 + z_3 l_3) g_{ijk}(\mathbf{l}) d\omega = \int_{\Omega^i} l_l g_{ijk}(\mathbf{l}) d\omega \quad (\text{II .38})$$

and the Hill's tensor  $\mathbb{P}$  can be written as follows:

$$P_{ijkl} = \frac{1}{4} \int_{\Omega^i} (l_l g_{kij}(\mathbf{l}) + l_l g_{kji}(\mathbf{l}) + l_k g_{lij}(\mathbf{l}) + l_k g_{lji}(\mathbf{l})) d\omega \quad (\text{II .39})$$

In summary, Hill's tensor  $\mathbb{P}$  depends mainly on the shape of the inclusion and the elastic properties of the porous clay matrix. Since the size of inclusion is very small compared to the macroscopic structure, this thesis considers the inclusion to be a spherical shape. The calculation of  $\mathbb{P}$  is based on the previous works [Giraud et al., 2007, Mura, 1987, Pan and Chou, 1976] and will be presented in this section.

The vector  $\mathbf{l}$  in Equation II .39 defines the unit outward normal of the inclusion, and its components can be expressed in terms of two basic angles,  $\psi \in [0, \pi]$ ,  $\zeta \in [0, 2\pi]$ , of the spherical coordinates frame shown as follows:

$$\begin{cases} l_1 = \sin(\psi) \cos(\zeta) \\ l_2 = \cos(\psi) \\ l_3 = \sin(\psi) \sin(\zeta) \end{cases} \quad (\text{II .40})$$

The calculation of Hill's tensor for inclusions can be explicitly calculated after making the following integrals:

$$\begin{aligned}
 C_{12}^{*i} &= (C_{11}^{pm} C_{22}^{pm})^{1/2}, \quad D = \frac{1}{4\pi C_{44}^{pm} \nu_3} \\
 I_1(i) &= 2\pi\nu_i \int_0^1 \frac{1-x^2}{x^2(1-\nu_i^2) + \nu_i^2} dx \\
 I_2(i) &= \frac{4\pi}{\nu_i} \int_0^1 \frac{x^2}{x^2(1-\nu_i^2) + \nu_i^2} dx \\
 I_{12} &= \frac{3\pi\nu_1}{2} \int_0^1 \frac{(1-x^2)^2}{x^2(1-\nu_1^2) + \nu_1^2} dx
 \end{aligned} \tag{II .41}$$

Finally, the components of Hill's tensor are given as follows by considering two different cases:

(a) If  $C_{12}^{*i} - C_{12}^{pm} - 2C_{44}^{pm} = 0$

$$\begin{aligned}
 P_{11}^i &= 3 \left( \frac{C_{12}^{pm}}{C_{12}^{pm} + C_{44}^{pm}} \right) A_1 I_1(1) - 6A_1 I_{12} + \frac{D}{4} I_1(3) \\
 P_{12}^i &= 2A_1 [-3I_1(1) + \nu_1^2 I_2(1) + 4I_{12}] \\
 P_{13}^i &= \left( \frac{C_{13}^{pm}}{C_{12}^{pm} + C_{44}^{pm}} \right) A_1 I_1(1) - 2A_1 I_{12} - \frac{D}{4} I_1(3) \\
 P_{22}^i &= 4\nu_1^2 A_1 \left[ 3I_1(1) - \left( \frac{C_{11}^{pm}}{C_{12}^{pm} + C_{44}^{pm}} \right) I_2(1) - 4I_{12} \right] \\
 P_{44}^i &= -A_1 \left[ 3 + \nu_1^2 \left( 3 + \frac{C_{44}^{pm}}{C_{12}^{pm} + C_{44}^{pm}} \right) \right] I_1(1) + \frac{A_1 \nu_1^2}{2} \left( \frac{C_{12}^{pm}}{C_{12}^{pm} + C_{44}^{pm}} \right) I_2(1) + 4A_1(1 + \nu_1^2) I_{12} + \frac{D}{8} \nu_3^2 I_2(3)
 \end{aligned} \tag{II .42}$$

where:

$$\begin{aligned}
 \nu_1 = \nu_2 &= \left( \frac{C_{11}^{pm}}{C_{22}^{pm}} \right)^{1/4}, \quad \nu_3 = \sqrt{\left( \frac{C_{11}^{pm} - C_{13}^{pm}}{2C_{44}^{pm}} \right)} \\
 k_1 = k_2 &= 1 \\
 B_1 &= -\nu_1 \frac{C_{12}^{pm} + C_{44}^{pm}}{16\pi C_{11}^{pm} C_{44}^{pm}}
 \end{aligned} \tag{II .43}$$

(b) If  $C_{12}^{*i} - C_{12}^{pm} - 2C_{44}^{pm} \neq 0$

$$\begin{aligned}
P_{11}^i &= \frac{3}{2} \sum_{i=1}^2 \nu_i A_i I_1(i) + \frac{DI_1(3)}{4} \\
P_{12}^i &= \sum_{i=1}^2 k_i \nu_i^3 A_i I_2(i) \\
P_{13}^i &= \frac{1}{2} \sum_{i=1}^2 \nu_i A_i I_1(i) - \frac{DI_1(3)}{4} \\
P_{22}^i &= -2 \sum_{i=1}^2 k_i^2 \nu_i^5 A_i I_2(i) \\
P_{44}^i &= \frac{1}{4} \sum_{i=1}^2 (1 + k_i) \nu_i^3 A_i [I_2(i) - 2k_i I_1(i)] + \frac{D\nu_3^2 I_2(3)}{8}
\end{aligned} \tag{II .44}$$

where:

$$\begin{aligned}
\nu_1 &= \sqrt{\frac{(C_{12}^{*i} - C_{12}^{pm})(C_{12}^{*i} + C_{12}^{pm} + 2C_{44}^{pm})}{4C_{22}^{pm} C_{44}^{pm}}} + \sqrt{\frac{(C_{12}^{*i} + C_{12}^{pm})(C_{12}^{*i} - C_{12}^{pm} - 2C_{44}^{pm})}{4C_{22}^{pm} C_{44}^{pm}}} \\
\nu_2 &= \sqrt{\left(\frac{C_{11}^{pm} - C_{13}^{pm}}{2C_{44}^{pm}}\right)} \\
\nu_3 &= \sqrt{\frac{(C_{12}^{*i} - C_{12}^{pm})(C_{12}^{*i} + C_{12}^{pm} + 2C_{44}^{pm})}{4C_{22}^{pm} C_{44}^{pm}}} + \sqrt{\frac{(C_{12}^{*i} + C_{12}^{pm})(C_{12}^{*i} - C_{12}^{pm} - 2C_{44}^{pm})}{4C_{22}^{pm} C_{44}^{pm}}} \\
k_i &= \frac{\frac{C_{11}^{pm}}{\nu_i^2} - C_{44}^{pm}}{C_{12}^{pm} + C_{44}^{pm}} \\
A_1 &= -\frac{C_{44}^{pm} - \nu_1^2 C_{22}^{pm}}{8\pi(\nu_2^2 - \nu_1^2)\nu_1^2 C_{22}^{pm} C_{44}^{pm}} \\
A_2 &= -\frac{C_{44}^{pm} - \nu_2^2 C_{22}^{pm}}{8\pi(\nu_2^2 - \nu_1^2)\nu_2^2 C_{22}^{pm} C_{44}^{pm}}
\end{aligned} \tag{II .45}$$

It is worth noting that the subscript 1, 2 and 3 directions in the above equations are the directions of the  $X_1$ -,  $X_2$ - and  $X_3$ -axes in Figure II .3, respectively. The Hill's tensor can be calculated by Equations II .41 to II .45. This is a simplified calculation method based on the assumption that the shape of the inclusion particle is spherical. In general, when considering the case that the shape of inclusions is an ellipsoid, the Hill's tensor can be calculated according to the basic Equation II .39. More complex cases of the shape of inclusions can be investigated in the future.

For this multi-scale anisotropic model, the pores embedded in the porous matrix also need to be considered at the microscopic scale. Here, the  $\mathbb{P}^p$  (in Equation II .16) will be

calculated using the same calculation method as  $\mathbb{P}^i$ . The pores inside the clayey matrix are also considered to be spherical shape. It is worth noting that the stiffness tensor  $\mathbb{C}^{pm}$  in Equations II .41 to II .45 should be replaced by the stiffness tensor of solid clay phase  $\mathbb{C}^s$ .

## 4 Hydraulic properties of claystone

As described in Chapter I , internal pores are found to exist in the clayey rocks, and the range of internal pore size in the clay-rich rocks is presented in Figure I .11. Besides, the variation of porosity of the clay-rich rocks with depth is presented in Figure I .10. In general, these pores will provide space for groundwater and gases. Therefore, in complex environments, the effect of hydro-mechanical coupling on their properties needs to be considered.

When the geo-materials is unsaturated, capillary forces often need to be considered. The role of capillary forces in the hydro-mechanical coupling of clayey rocks is analyzed by Jia et al. [2010], including three main factors. First, there are similarities between the capillary forces and the confining pressure in the triaxial experiments. The capillary forces will cause the closure of the interface of microcracks inside the clay matrix. This leads to an increase in the strength of the clayey rocks due to the decrease of the water content. Secondly, when these microcracks in clayey rocks are closed due to the presence of capillary forces, the frictional strength of the crack interface will be increased. Finally, these microcracks or pores inside the clay matrix are inhomogeneous in shape and size, which can generate the heterogeneity of capillary force inside the sample. And this is one of the reasons for the anisotropy of the macro-mechanical properties of the clayey rocks. Anisotropic characteristics can affect the physical and mechanical properties of the clayey rocks.

At the macroscopic scale, the clay matrix inside the clayey rocks is considered as a homogenized porous medium, saturated by a liquid fluid (water) and a gas phase which is a mixture of dry air and water vapor. Let  $p_l$  denoting the pressure of liquid and  $p_g$  that of the gas mixture. We also introduce the capillary pressure as  $p_{cp} = p_g - p_l$ . By using the nonlinear poroelastic theory for partially saturated media [Alonso et al., 1990, Coussy, 2004, Coussy et al., 1998, Fredlund and Rahardjo, 1993], the macroscopic poroelastic relations can be expressed as follows:

$$\boldsymbol{\Sigma} = \mathbb{C}^{hom} : \boldsymbol{E}^e - \boldsymbol{B}[p_g - S_l p_{cp}] \quad (\text{II .46})$$

where  $\boldsymbol{B}$  denotes the second order tensor of macroscopic Biot's coefficients and  $S_l$  the

water (liquid) saturation degree. The macroscopic Biot's tensor can be determined by the linear homogenization procedure and can be expressed as a function of the macroscopic elastic stiffness tensor  $\mathbb{C}^{hom}$  [Dormieux et al., 2006, 2002]:

$$\mathbf{B} = (\mathbb{I} - \mathbb{S}^s : \mathbb{C}^{hom}) \quad (\text{II .47})$$

where  $\mathbb{S}^s = (\mathbb{C}^s)^{-1}$  is the elastic compliance tensor of the solid clay phase. It is worth noticing that the Biot's coefficients are functions of the macroscopic elastic tensor  $\mathbb{C}^{hom}$ , which is affected by porosity. Thus, the Biot's coefficients can be affected by the porosity increase induced by the interface-debonding related damage. Further, the capillary pressure  $p_{cp}$  is related to the saturation degree  $S_l$  through the water retention curve. This one can be affected by micro-structural evolution of porous materials including porosity change due to induced damage process. However, this specific issue is not discussed here and can be investigated in future.

As shown in Figure I .5(b), the elastic stiffness of clayey rocks varies with different humidities, so the effect of relative humidity on the elastic stiffness of clayey rocks will be considered. For clayey rocks, the elastic properties of inclusions are almost insensitive to water saturation, so the water sensitivity of elastic properties is attributed to the solid clay phase in the clayey rocks. Moreover, due to the layered micro-structure of solid clay phase, the water saturation change leads to the compaction or opening of inter-layer space. Consequently, among the five elastic parameters (i.e.,  $E_{\perp}^s$ ,  $E_{\parallel}^s$ ,  $\nu_{\perp\parallel}^s$ ,  $\nu_{\parallel\parallel}^s$ ,  $G_{\perp\parallel}^s$ ), the elastic modulus perpendicular to layer planes  $E_{\perp}^s$  is the most sensitive one to water saturation degree. Therefore, it is assumed that this modulus increases with the capillary pressure by the following relation:

$$E_{\perp}^s(p_{cp}) = E_{\perp 0}^s \left( 1 + \beta_1 \frac{p_{cp}}{h} \right) \quad (\text{II .48})$$

where  $E_{\perp 0}^s$  is the value of  $E_{\perp}^s$  for  $p_{cp} = 0$  at the saturated condition. The parameter  $\beta_1$  controls the variation of  $E_{\perp}^s$  and the cohesion coefficient  $h$  is used to normalize the value of  $p_{cp}$ .

On the other hand, the capillary pressure  $p_{cp}$  can be related to the relative humidity  $H_r$  through the Kelvin's law:

$$\ln(H_r) = \frac{M_{vp}^{ol}}{RT_{abs}\rho_{lq}} p_{cp} \quad (\text{II .49})$$

where  $M_{vp}^{ol}$  is the molar mass of vapor,  $R$  the universal gas constant,  $T_{abs}$  the absolute temperature and  $\rho_{lq}$  the volumetric mass of liquid. Further, in some previous studies [Liu and Shao, 2016, Valès et al., 2004, Zhang, 2017], it is found that the macroscopic elastic stiffness of clay-rich rocks can increase with the decrease of water saturation.

In addition, the inherent permeability of the clayey rocks need to be taken into account when considering the hydro-mechanical coupling effect on their physical-mechanical properties. And the variation of permeability can be used to accumulate damage inside the clayey rocks. On the other hand, the flow of fluids inside the rock can also have an effect on the physical and mechanical properties of the rock. The fluid diffusion inside the porous medium is described by using the Darcy's law:

$$\underline{Q} = \underline{K}iA \tag{II .50}$$

where  $\underline{Q}$  is the flow rate through the material,  $i$  and  $A$  denote the hydraulic gradient and cross-sectional area of the material, and  $\underline{K}$  is the hydraulic conductivity in the flow direction. The value of hydraulic conductivity is determined by the permeability of the porous medium:

$$\underline{K} = \frac{k\rho_{lq}\underline{g}}{\mu_{lq}} \tag{II .51}$$

where  $\rho_{lq}$  denotes the volumetric mass of liquid,  $\underline{g}$  denotes the acceleration due to gravity, and  $\mu_{lq}$  is the dynamic viscosity of the fluid mass.

## 5 Conclusions

In this chapter, a homogenization method that can be used to reflect the mechanical and hydraulic properties of clayey rocks was developed based on their physical and mechanical properties and the related theoretical background.

Here, two different homogenization schemes were introduced firstly in this chapter, including the Dilute scheme and the Mori-Tanaka scheme. The Mori-Tanaka scheme was selected to use in the multi-scale anisotropy model described above. The most important aspect of the homogenization method was the calculation of Hill's tensor. For this reason, the second section of this chapter was focused on the detailed solution of Hill's tensor. In addition, this part also presented the basic theory of Green's function. It is worth noting that the Green's function was used in Hill's tensor equation mainly because of the anisotropic characteristics of the porous clay matrix. Finally, the hydro-mechanical coupling behavior of the clayey rocks was considered.

This chapter mainly consider the elastic properties of clayey rocks, whose plastic properties will be presented in the next chapter.

# Chapter III

## Nonlinear homogenization method applied to CO<sub>x</sub> claystone that considers the macroscopic plastic-viscoplastic criterion, hydraulic effects, and damage

### Contents

---

<b>1</b>	<b>Introduction</b> . . . . .	<b>39</b>
<b>2</b>	<b>Description of macroscopic plastic criterion</b> . . . . .	<b>41</b>
<b>3</b>	<b>Extension of the macroscopic yield criterion</b> . . . . .	<b>46</b>
3.1	Macroscopic yield criterion considering anisotropic effects . . . . .	46
3.2	Constitutive model for long-term behavior of clayey rocks . . . . .	53
3.3	Description of damage . . . . .	54
3.4	Effect of hydro-mechanical coupling on plastic deformation of clayey rocks . . . . .	61
<b>4</b>	<b>Conclusions</b> . . . . .	<b>62</b>

---

### 1 Introduction

As mentioned in Chapter I , the mechanical properties of claystone are closely related to their complex structure at the micro-macro scales. Under the application of load,

the position of mineral particles inside the claystone will change, and the pores inside the clay matrix will also change. Some fractures can be induced in this process. And this phenomenon will lead to changes in the mechanical properties of clayey rocks. In addition, their mechanical properties are sensitive to water saturation degree [Liu and Shao, 2016, Valès et al., 2004, Zhang, 2017]. Time-dependent deformation is also an important feature of clayey rocks [Armand et al., 2017b, Fabre and Pellet, 2006, Gasc-Barbier et al., 2004, Liu et al., 2018b]. Two principal mechanisms are often invoked: namely, the viscoplastic deformation and time-dependent cracking between inclusions and clay matrix [Bikong et al., 2015, Farhat et al., 2017]. The mechanical properties of claystone can also be affected by the variation of temperatures, such as the decrease of elastic modulus and failure strength with the rise of temperature [Liu et al., 2019, Masri et al., 2014, Menaceur et al., 2015, Zhang, 2018].

On the other hand, in order to identify the main physical mechanisms of clayey rocks deformation and failure, different kinds of microscopic and mesoscopic experimental studies have been performed. Both post-mortem analysis of tested samples and *in situ* tests have been carried out by using different kinds of imaging techniques such as X-ray tomography [Bornert, 2010, Desbois et al., 2017, Lenoir et al., 2007]. According to those results, plastic deformation and damage of clayey rocks are two principal inelastic mechanisms. Plastic deformation occurs mainly inside the clay matrix, while damage is due to micro-cracks around stiff mineral particles and inside the clay phase [Bornert et al., 2010, Wang et al., 2015].

Based on the literature mentioned above, macroscopic constitutive models should first be formulated for different types of clay-rich rocks [Chiarelli et al., 2003, Hoxha et al., 2007, Jia et al., 2010, Shao et al., 2006]. The structural anisotropy has been taken into account in some models [Pietruszczak et al., 2002], as well as the water saturation degree [Jia et al., 2010] and the creep deformation [Farhat et al., 2017, Pietruszczak et al., 2004]. These phenomenological models are generally fitted from macroscopic laboratory tests and not able to systematically incorporate the effects of mineralogy. In order to improve and enrich the macroscopic modeling, micro-mechanics based models have recently been developed. For instance, various homogenization schemes have been used to estimate the macroscopic elastic properties [Giraud et al., 2007, Guéry et al., 2010, Shen and Shao, 2015b]. With the help of limit analysis technique and variational principles, analytical macroscopic plastic yield criteria have been established for porous and inclusions-reinforced geological materials [Barthélémy and Dormieux, 2004, Guo et al., 2008, He et al., 2013, Jeong, 2002, Maghous et al., 2009, Shen et al., 2020, 2014, 2013b, 2012a, 2017]. These

criteria are explicitly dependent on the porosity and content of mineral particles and take the form of the yield functions to formulate complete micro-mechanics based plastic models for clayey rocks, mostly with the isotropic assumption [Bignonnet et al., 2016, Shen et al., 2013a, 2012b, 2018].

The objective of this chapter is to develop a unified micromechanics-based constitutive model, dealing with plastic, viscoplastic strain, and damage evolution of anisotropic clayey rocks. And the effect of hydro-mechanical coupling on the performance of clayey rocks will be also considered. For this purpose, two homogenization steps will be considered:

- ★ The first step of homogenization is to propose an effective plastic criterion for the porous matrix by considering the effect of pores;
- ★ The second step is to estimate the macroscopic mechanical properties and formulate the macroscopic plasticity criterion for the inclusion-reinforced clay composites. The effects of the structural anisotropy of the solid clay phase and the influence of water saturation on the mechanical properties are considered.

## 2 Description of macroscopic plastic criterion

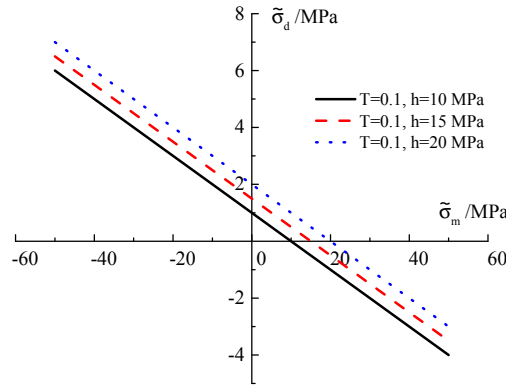
As for the elastic behavior, the plastic strains are affected by pores and inclusions at the two scales. For this purpose, the macroscopic plastic criterion is first determined by conducting two steps of homogenization. The obtained criterion is then used as the plastic yield function. However, unlike the homogenization of elastic tensor including directly the anisotropy of solid clay phase, the homogenization of the macroscopic plastic criterion is realized in a simplified way. Indeed, it is very hard to analytically complete the two steps of nonlinear homogenization by considering a transversely isotropic solid clay phase at the microscopic scale. Therefore, the macroscopic plastic criterion is first determined analytically for an isotropic solid clay phase. The obtained macroscopic criterion is then heuristically modified to include the anisotropy of the solid clay phase.

The macroscopic plastic strain of clay-rich rocks is usually attributed to the irreversible sliding of clay particles at the microscopic scale. The plastic yield function is characterized by the linear Drucker-Prager criterion written as:

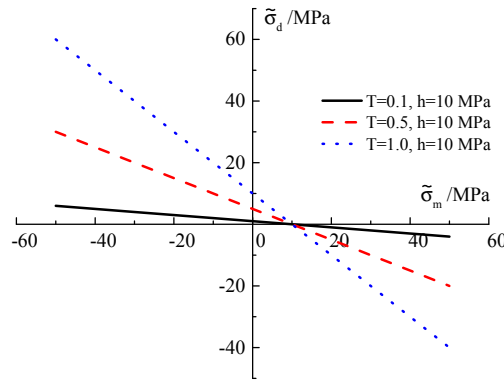
$$\phi^m(\tilde{\boldsymbol{\sigma}}) = \tilde{\sigma}_d + T(\tilde{\sigma}_m - h) \leq 0 \quad (\text{III .1})$$

where  $\tilde{\boldsymbol{\sigma}}$  denotes the local stress tensor in the solid clay phase,  $\tilde{\sigma}_m = \text{tr}\tilde{\boldsymbol{\sigma}}/3$  is the mean stress, and  $\tilde{\sigma}_d = \sqrt{\tilde{\boldsymbol{\sigma}}' : \tilde{\boldsymbol{\sigma}}'}$  the equivalent stress, with  $\tilde{\boldsymbol{\sigma}}' = \tilde{\boldsymbol{\sigma}} - \tilde{\sigma}_m \mathbf{1}$ . The  $\mathbf{1}$  is the second-

order unit tensor. The parameter  $h$  defines the hydrostatic tensile yield stress while  $T$  corresponds to the frictional coefficient of the solid clay phase. The two strength parameters can be related to the frictional angle  $\varphi$  and cohesion  $c$  in the sense of Mohr-Coulomb criterion:  $T = \frac{2\sqrt{6}\sin\varphi}{3\pm\sin\varphi}$  and  $h = c \arctan\varphi$ . The Drucker-Prager surface subscribes or inscribes the Mohr-Coulomb's one if the positive or negative sign is taken in the calculation of  $T$ .



(a) Different  $h$



(b) Different  $T$

**Figure III .1:** Effect of parameters of  $h$  and  $T$  on the Drucker-Prager criterion

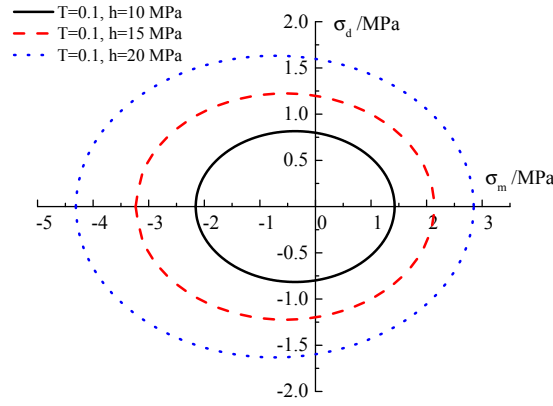
Here, we evaluate the effect of two parameters ( $T$  and  $h$ ) on the mechanical response of the solid clay phase. Figures III .1(a) and III .1(b) show that  $T$  affects the slope of the plastic yield criterion and  $h$  affects the extension of the plastic yield criterion, respectively.

By using the modified secant method proposed by [Maghous et al., 2009], the effective plasticity criterion for homogenized porous media at the microscopic scale is established

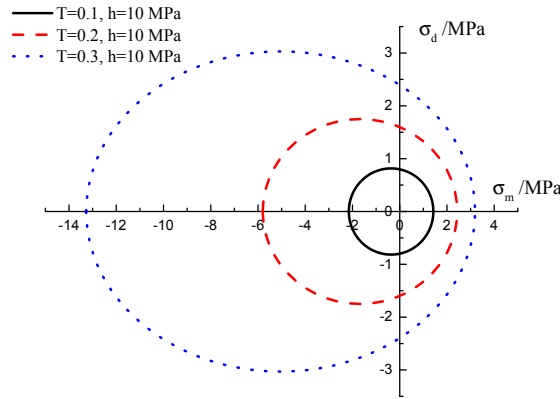
and express as follows:

$$\phi^{pm}(\boldsymbol{\sigma}, f, T) = \frac{1 + 2f/3}{T^2} \sigma_d^2 + \left( \frac{3f}{2T^2} - 1 \right) \sigma_m^2 + 2(1-f)h\sigma_m - (1-f)^2 h^2 = 0 \quad (\text{III .2})$$

where  $\sigma_m = \text{tr}\boldsymbol{\sigma}/3$  is the local mean stress of the homogenized porous medium while  $\sigma_d = \sqrt{\boldsymbol{\sigma}' : \boldsymbol{\sigma}'}$  is the deviatoric stress, with  $\boldsymbol{\sigma}' = \boldsymbol{\sigma} - \sigma_m \mathbf{1}$ . One can see that the effective plastic criterion of homogenized porous medium (as shown in Equation III .2) depends explicitly on the porosity  $f$ . This effective plastic criterion is already used by several researchers [Farhat et al., 2017, Huang et al., 2014, Shen et al., 2013a].



(a) Different  $h$



(b) Different  $T$

**Figure III .2:** Effect of parameters of  $h$  and  $T$  on the effective plasticity criterion of the porous clay matrix

Again, we evaluate the effect of two parameters (i.e.,  $T$  and  $h$ ) on the effective plasticity

criterion of the porous clay matrix, as shown in Figure III .2. And the reference value of the parameter used is:  $f = 0.16$ . It can be seen that these two parameters have different degrees of influence on the yield surface of the porous clay matrix.

According to the plasticity criterion Equation III .2 for porous media, the strain rate of porous matrix can be expressed as follows [Shen and Shao, 2015b]:

$$\begin{aligned} \mathbf{d} &= \dot{\chi} \frac{\partial \Phi^{pm}}{\partial \boldsymbol{\sigma}} \\ &= \frac{T^2 d_d}{(1 + 2f/3)2\sigma_d} \left[ \frac{1 + 2f/3}{T^2} 2\boldsymbol{\sigma}' + \left( \frac{3f}{2T^2} - 1 \right) \frac{2}{3} \sigma_m \mathbf{1} + \frac{2(1-f)h}{3} \mathbf{1} \right] \end{aligned} \quad (\text{III .3})$$

where  $d_d = \sqrt{\mathbf{d}' : \mathbf{d}'}$ , and  $\mathbf{d}' = \mathbf{d} - d_m \mathbf{1}$ . The multiplier of porous medium is  $\dot{\chi} = \mathbf{d}' / \left( \frac{\partial \Phi^{pm}}{\partial \boldsymbol{\sigma}'} \right)$ . The convex and closed surface of strength domain  $\Phi^{pm}$  can be characterized by its support function as follows:

$$\begin{aligned} \pi^{pm} &= \mathbf{d} : \boldsymbol{\sigma} \\ &= \frac{T^2 d_d}{(1 + 2f/3)2\sigma_d} \left[ \frac{1 + 2f/3}{T^2} 2\sigma_d^2 + \left( \frac{3f}{2T^2} - 1 \right) 2\sigma_m^2 + 2(1-f)h\sigma_m \right] \end{aligned} \quad (\text{III .4})$$

In combination with the Equations III .2 and III .3, the local stress of porous clay matrix in Equation III .4 can be replaced. The support function can be rewritten as follows:

$$\pi^{pm} = (1-f)h \sqrt{\left( \frac{3fT^2}{(3f-2T^2)(1+2f/3)} \right) \left( d_d^2 + \frac{1+2f/3}{3f/2-T^2} \text{tr} \mathbf{d}^2 \right)} - (1-f)h \frac{2T^2}{3f-2T^2} \text{tr} \mathbf{d} \quad (\text{III .5})$$

With the help of the support function  $\pi^{pm}$  expression, the local stress in the porous clay matrix can be obtained in the following form:

$$\begin{aligned} \boldsymbol{\sigma} &= \frac{\partial \pi^{pm}}{\partial \mathbf{d}} = \mathbb{C}^{pm}(d_d, \text{tr} \mathbf{d}) : \mathbf{d} - (1-f)h \frac{2T^2}{3f-2T^2} \mathbf{1} \\ \mathbb{C}^{pm}(d_d, \text{tr} \mathbf{d}) &= 3k^{pm}(d_d, \text{tr} \mathbf{d}) \mathbb{J} + 2\mu^{pm}(d_d, \text{tr} \mathbf{d}) \mathbb{K} \\ k^{pm} &= \frac{1+2f/3}{3f/2-T^2} \frac{N}{M}, \quad \mu^{pm} = \frac{N}{2M} \\ N &= (1-f)h \sqrt{\frac{3fT^2}{(1+2f/3)(3f-2T^2)}}, \quad M = \sqrt{d_d^2 + \frac{1+2f/3}{3f/2-T^2} \text{tr} \mathbf{d}} \end{aligned} \quad (\text{III .6})$$

As the strain rate  $\mathbf{d}$  is non-uniform, the mean value of  $\mathbf{d}$  can be chosen as the effective strain rate [Maghous et al., 2009]:

$$d_d^{eff} = \sqrt{\langle d_d^2 \rangle}, \quad (\text{tr} \mathbf{d})^{eff} = \sqrt{\langle (\text{tr} \mathbf{d}^{eff})^2 \rangle} \quad (\text{III .7})$$

Therefore, the local stress of porous clay matrix in Equation III .6 can be rewritten as:

$$\begin{aligned}\boldsymbol{\sigma} &= \mathbb{C}^{pm}(d_d^{eff}, (tr\mathbf{d})^{eff}) : \mathbf{d} - (1-f)h \frac{2T^2}{3f-2T^2} \mathbf{1} \\ \mathbb{C}^{pm}(d_d^{eff}, (tr\mathbf{d})^{eff}) &= 3k_{eq}^{pm}(d_d^{eff}, (tr\mathbf{d})^{eff})\mathbb{J} + 2\mu_{eq}^{pm}(d_d^{eff}, (tr\mathbf{d})^{eff})\mathbb{K}\end{aligned}\quad (\text{III .8})$$

Since the clayey rocks are composed of porous matrix and mineral inclusions as shown in the Figure II .1. The macroscopic stress of clayey rocks (without considering the hydraulic effect) can be expressed as:

$$\begin{aligned}\boldsymbol{\Sigma} &= \mathbb{C}^{hom} : \mathbf{D} - (1-f)h \frac{2T^2}{3f-2T^2} \mathbf{1} \\ \mathbb{C}^{hom} &= 3k^{hom}\mathbb{J} + 2\mu^{hom}\mathbb{K}\end{aligned}\quad (\text{III .9})$$

According to the Barthélemy and Dormieux [2004] research, the effective strain rate is related to the bulk and shear modulus of the macroscopic claystone and the porous matrix. This can be expressed as:

$$\begin{aligned}\frac{1}{2}(1-\rho)((tr\mathbf{d})^{eff})^2 &= \frac{1}{2} \frac{\partial k^{hom}}{\partial k_{eq}^{pm}} (tr\mathbf{D})^2 + \frac{\partial \mu^{hom}}{\partial k_{eq}^{pm}} D_d^2 \\ (1-\rho)(d_d^{eff})^2 &= \frac{1}{2} \frac{\partial k^{hom}}{\partial \mu_{eq}^{pm}} (tr\mathbf{D})^2 + \frac{\partial \mu^{hom}}{\partial \mu_{eq}^{pm}} D_d^2\end{aligned}\quad (\text{III .10})$$

where  $D_d = \sqrt{\mathbf{D}' : \mathbf{D}'}$  with  $\mathbf{D}' = \mathbf{D} - D_m \mathbf{1}$ . As for the isotropic porous medium, the homogenized secant moduli  $k^{hom}$  and  $\mu^{hom}$  can be determined by Equation III .11, which can be shown as follows:

$$\begin{aligned}k^{hom} &= \frac{3k_{eq}^{pm} + 4\rho\mu_{eq}^{pm}}{3(1-\rho)} \\ \mu^{hom} &= \mu_{eq}^{pm} \frac{k_{eq}^{pm}(6+9\mu) + \mu_{eq}^{pm}(12+8\rho)}{6(1-\rho)(k_{eq}^{pm} + 2\mu_{eq}^{pm})}\end{aligned}\quad (\text{III .11})$$

By substituting the local stress  $\boldsymbol{\sigma}$  of the porous matrix into the macroscopic stress  $\boldsymbol{\Sigma}$  and combining the Equations III .9, III .10 and III .11, an analytical macroscopic plastic criterion for the clayey rocks can be obtained as follows:

$$\Phi(\boldsymbol{\Sigma}, f, \rho, T) = \Theta \Sigma_d^2 + \left( \frac{3f}{2T^2} - 1 \right) \Sigma_m^2 + 2(1-f)h \Sigma_m - \frac{3+2f+3f\rho}{3+2f} (1-f)^2 h^2 = 0$$

with

$$\Theta = \frac{\frac{1+2f/3}{T^2} + \frac{2}{3}\rho \left( \frac{3f}{2T^2} - 1 \right)}{\frac{4T^2-12f-9}{6T^2-13f-6}\rho + 1}\quad (\text{III .12})$$

where  $\Sigma_m = tr\Sigma/3$  and  $\Sigma_d = \sqrt{\Sigma' : \Sigma'}$ , with  $\Sigma' = \Sigma - \Sigma_m \mathbf{1}$ , are respectively the macroscopic mean and deviatoric stresses.

As the main advantage with respect to classical phenomenological plastic criterion, the micro-mechanics based macroscopic plastic criterion [Bornert, 2010] explicitly takes into account the effects of porosity  $f$  and of inclusions  $\rho$ . During plastic deformation, the values of  $f$  and  $\rho$  can change, and this result in the variation of yield stress. For instance, when the porosity decreases, the yield stress increases and one gets plastic hardening. Inversely, the increase of porosity leads to plastic softening. Therefore, the use of micro-mechanics based plastic criterion allows naturally considering plastic hardening or softening due to the evolution of porosity and inclusion fraction. However, according to previous studies [Shen et al., 2013a, Shen and Shao, 2016, Shen et al., 2012b], the evolutions of porosity and inclusion fraction alone cannot fully describe the plastic hardening or softening. It is found that the frictional coefficient of the solid clay phase  $T$  evolves with plastic deformation history. We assume that  $T$  is a function of the equivalent plastic strain of the solid clay phase denoted by the variable  $\tilde{\epsilon}^p$ :

$$T = T_m - (T_m - T_0)e^{-b_1\tilde{\epsilon}^p} \quad (\text{III .13})$$

where  $T_0$  and  $T_m$  define the initial threshold and asymptotic value of the frictional coefficient respectively.  $b_1$  is the parameters that controls the kinetics of hardening. The evolution of  $\tilde{\epsilon}^p$  is related to that of macroscopic plastic strain and is detailed below.

It is noting that the theory of the macroscopic yield criterion for isotropic clay-rich rocks presented above is based on the research results of Shen et al. [2013a].

### 3 Extension of the macroscopic yield criterion

#### 3.1 Macroscopic yield criterion considering anisotropic effects

The effect of anisotropy of the solid clay phase is now introduced into the homogenized macroscopic plasticity criterion [Bornert, 2010]. For the sake of clarity, the solid clay phase is assumed to have an transversely isotropic structure. As randomly distributed pores and inclusions are considered here, the transversely isotropic structure is assumed to be conserved at the macroscopic scale. For the sake of convenience, a second-order fabric tensor  $\mathbf{a}$  is introduced to characterize the transversely isotropic material structure [Pietruszczak et al., 2002, Pietruszczak and Mroz, 2000, 2001]. The principal frame of  $\mathbf{a}$  coincide with that of the transversely isotropic material and is specified by the unit vectors

$e^k (k = 1, 2, 3)$ . The components of  $a_{ij}$  are then given by:

$$a_{ij} = \tilde{a}_1 e_i^1 e_j^1 + \tilde{a}_2 e_i^2 e_j^2 + \tilde{a}_3 e_i^3 e_j^3 \quad (\text{III .14})$$

where  $\tilde{a}_1$ ,  $\tilde{a}_2$  and  $\tilde{a}_3$  are the principal values of the fabric tensor, as shown in Figure III .3. On the other hand, for any macroscopic stress tensor  $\Sigma$  projected onto the principal frame of  $\mathbf{a}$ , one can calculate the magnitudes of the stress traction along the three frame vectors,  $L_k (k = 1, 2, 3)$ :

$$\begin{cases} L_1 = (\Sigma_{11}^2 + \Sigma_{12}^2 + \Sigma_{13}^2)^{1/2} \\ L_2 = (\Sigma_{21}^2 + \Sigma_{22}^2 + \Sigma_{23}^2)^{1/2} \\ L_3 = (\Sigma_{31}^2 + \Sigma_{32}^2 + \Sigma_{33}^2)^{1/2} \end{cases} \quad (\text{III .15})$$

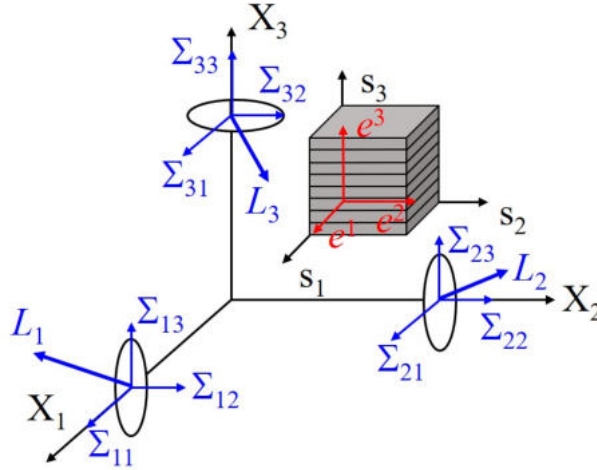


**Figure III .3:** The microstructure tensor  $\mathbf{a}$  and the loading vector  $\mathbf{L}$

Then, one defines a normalized loading orientation vector  $\mathbf{l}$  with the following components  $l_i (i = 1, 2, 3)$ :

$$l_i = \frac{L_i}{(L_k L_k)^{1/2}} \quad (\text{III .16})$$

With these components in hand, the following scalar parameter  $\eta$  is introduced [Pietruszczak et al., 2002, Pietruszczak and Mroz, 2000, 2001]:

$$\eta = a_{ij} l_i l_j \quad (\text{III .17})$$

$\eta$  physically represents the projection of the fabric tensor  $\mathbf{a}$  onto the loading orientation  $\mathbf{l}$ . Its value changes with the loading orientation. In practice, like any second rank tensor,

the fabric tensor can be decomposed into a spherical part and a deviatoric part:

$$\hat{\eta} = \frac{a_{kk}}{3}, \quad \hat{a}_{ij} = (a_{ij} - \hat{\eta}\delta_{ij})/\hat{\eta} \quad (\text{III .18})$$

$\delta_{ij}$  is the Kronecker delta. Physically,  $\hat{\eta}$  is the mean value of  $\tilde{a}_k (k = 1, 2, 3)$  while  $\hat{a}_{ij}$  represents the deviations from the mean value.

With this decomposition, the scalar parameter  $\eta$  can be approximated by the following polynomial form:

$$\eta = a_{ij}l_i l_j = \hat{\eta} [1 + \hat{a}_{ij}l_i l_j + c_1(\hat{a}_{ij}l_i l_j)^2 + c_2(\hat{a}_{ij}l_i l_j)^3 + \dots] \quad (\text{III .19})$$

The coefficients  $c_k (k = 1, 2, \dots)$  are introduced to characterize the degree of material anisotropy. It is noticed that for an isotropic material, the fabric tensor reduces to a spherical tensor and one gets  $\hat{a}_{ij} = 0$ . Consequently, the parameter  $\eta = \hat{\eta}$  is constant and independent of loading orientation.

For the clay-rich rocks studies here, it is assumed that the maximum value of frictional coefficient of the solid clay phase  $T_m$ , controlling the macroscopic failure strength, is dependent on loading orientation [Shen and Shao, 2015b]. Therefore,  $T_m$  is taken as a function of the loading parameter  $\eta$  in the following form:

$$T_m(\eta) = \hat{T}_m [1 + \hat{a}_{ij}l_i l_j + c_1(\hat{a}_{ij}l_i l_j)^2 + c_2(\hat{a}_{ij}l_i l_j)^3 + \dots] \quad (\text{III .20})$$

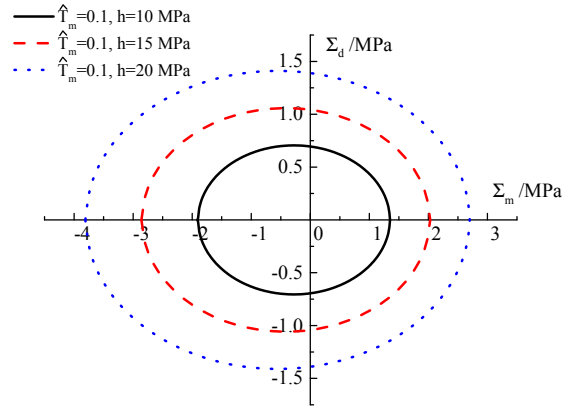
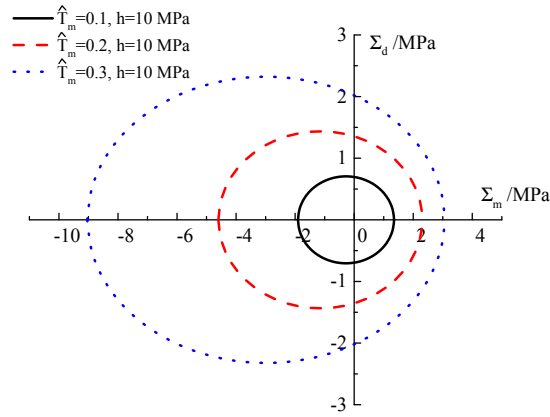
where  $\hat{T}_m$  represents the mean value of  $T_m$ .

Accordingly, the macroscopic plastic yield function is now dependent on the loading parameter  $\eta$  and then extended to anisotropic materials:

$$\Phi_p(\Sigma, f, \rho, T, \eta) = \Theta \Sigma_d^2 + \left( \frac{3f}{2T(\eta)^2} - 1 \right) \Sigma_m^2 + 2(1-f)h\Sigma_m - \frac{3+2f+3f\rho}{3+2f}(1-f)^2 h^2 = 0$$

with

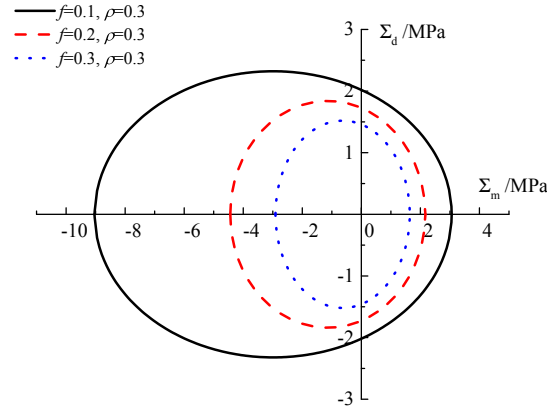
$$\Theta = \frac{\frac{1+2f/3}{T(\eta)^2} + \frac{2}{3}\rho \left( \frac{3f}{2T(\eta)^2} - 1 \right)}{\frac{4T(\eta)^2 - 12f - 9}{6T(\eta)^2 - 13f - 6}\rho + 1} \quad (\text{III .21})$$

(a) Different  $h$ (b) Different  $\hat{T}_m$ **Figure III .4:** Effect of parameters of  $h$  and  $\hat{T}_m$  on the macroscopic plasticity criterion

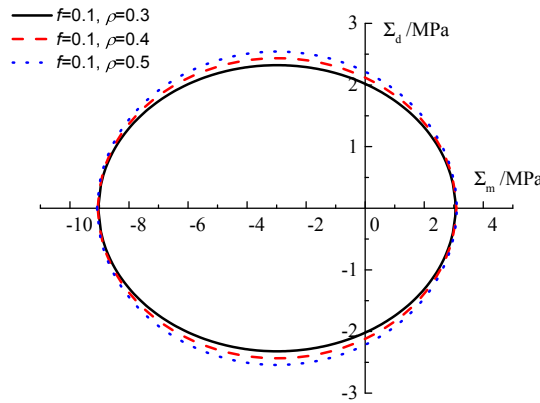
As shown in Figure III .4, we investigate the effect of the parameters of  $h$  and  $\hat{T}_m$  on the macroscopic mechanical behavior of clayey rocks. The used plasticity parameters of clayey rocks are:  $T_0 = 0.01$ ,  $b_1 = 100$ , and the equivalent plastic strain of solid clay phase  $\tilde{\epsilon}^p = 0.01$ . The porosity and volume fraction of the inclusions are defined as:  $f = 0.1$  and  $\rho = 0.3$ , respectively. It can be seen from Figure III .4(a) that the increase in  $h$  causes the plastic yield surface to expand approximately isotropically. The difference is that in the Figure III .4(b), the expansion of the elliptical yield surface in the negative direction of the horizontal axis (i.e.,  $\Sigma_m$ ) is greater than the expansion in the positive direction, which indicates that the effect of  $\hat{T}_m$  on the yield surface is mainly to enhance the compressive strength.

In addition, this section also considers the effect of porosity  $f$  and  $\rho$  on the macroscopic

plasticity criterion of the clayey rocks, as shown in Figure III .5. The parameters used are the same as in Figure III .4 above, i.e.,  $T_0 = 0.01$ ,  $b_1 = 100$ , and  $\tilde{\epsilon}^p = 0.01$ .  $\hat{T}_m$  and  $h$  are kept constant at 0.3 and 10 MPa, respectively.



(a) Porosity



(b) volume fraction of inclusions  $\rho$

**Figure III .5:** Effect of porosity  $f$  and volume fraction of inclusions  $\rho$  on the macroscopic plasticity criterion

From Figure III .5(a), it can be seen that with the increase in porosity, there is a clear pattern of smaller yield surfaces. This phenomenon is mainly due to the increase in porosity, which weakens the strength of the claystone and makes it easier to produce plastic deformation under the same stress conditions. In addition, the change in the value of  $\rho$  has little effect on the macroscopic plastic yield surface, as can be shown in Figure III .5(b).

On the other hand, for most geological materials, a non-associative plastic flow rule may be necessary to better describe the plastic volumetric strain, for instance, the compressibility-dilatancy transition. Therefore, a non-associative macroscopic plastic potential should be determined, ideally by rigorous homogenization procedures as for the homogenized macroscopic plastic criterion III .21. However, this is a very delicate task for materials containing heterogeneities at two different scales like clay-rich rocks studied here. Therefore, a heuristic approach is here adopted. Indeed, in the previous study [Maghous et al., 2009] devoted to plastic homogenization of porous materials composed of a solid matrix obeying the Drucker-Prager criterion and a non-associated flow rule, an effective plastic potential of homogenized porous media was obtained by using a rigorous modified secant method (corresponding to the homogenized porous matrix at the mesoscopic scale in this study, see Figure II .1). The expression of the obtained potential is very similar to that of the effective plastic criterion III .21, just by replacing the term  $T^2$  by  $Tt$  with  $t$  being the microscopic dilatancy coefficient. As the same homogenization method (the modified secant method) is used for the second step of homogenization here to consider the effect of mineral inclusions, it is assumed that this property is conserved for the macroscopic plastic potential. That allows postulating that the macroscopic plastic potential can be heuristically deduced from the macroscopic plastic yield function III .21 replacing the term  $T^2$  by  $Tt$ . Therefore, the heuristic macroscopic plastic potential is given by:

$$G_p(\Sigma, f, \rho, T, t, \eta) = \Theta \Sigma_d^2 + \left( \frac{3f}{2T(\eta)t(\eta)} - 1 \right) \Sigma_m^2 + 2(1-f)h\Sigma_m - \frac{3+2f+3f\rho}{3+2f}(1-f)^2 h^2$$

with

$$\Theta = \frac{\frac{1+2f/3}{T(\eta)t(\eta)} + \frac{2}{3}\rho \left( \frac{3f}{2T(\eta)t(\eta)} - 1 \right)}{\frac{4T(\eta)t(\eta)-12f-9}{6T(\eta)t(\eta)-13f-6}\rho + 1} \quad (\text{III .22})$$

Similar to the frictional coefficient  $T$ , the dilatancy coefficient  $t$  is also a function of the equivalent plastic strain of the solid clay phase  $\tilde{\epsilon}^p$ :

$$t = t_m - (t_m - t_0)e^{-b_2\tilde{\epsilon}^p} \quad (\text{III .23})$$

where  $b_2$  is the parameter controlling the evolution of  $t$  from its initial value  $t_0$  to the maximum one  $t_m$ . Further, the macroscopic plastic flow rule should also depend on loading orientation for anisotropic materials. Therefore, in a similar way as for the frictional coefficient, it is assumed that the maximum value of the coefficient  $t$ ,  $t_m$ , is a function of the loading parameter  $\eta$ :

$$t_m(\eta) = \hat{t}_m \left[ 1 + \hat{a}_{ij}l_i l_j + c_1(\hat{a}_{ij}l_i l_j)^2 + c_2(\hat{a}_{ij}l_i l_j)^3 + \dots \right] \quad (\text{III .24})$$

With the macroscopic plastic yield function and potential in hand, the macroscopic instantaneous plastic strain rates can be determined by the following non-associated flow rule:

$$\dot{\mathbf{E}}^p = \dot{\lambda}_p \frac{\partial G_p}{\partial \boldsymbol{\Sigma}} \quad (\text{III .25})$$

The plastic multiplier  $\dot{\lambda}_p$  can be classically calculated from the plastic consistency condition:  $\dot{\Phi}_p = 0$ . And its expression can be written as follows:

$$\dot{\lambda}_p = \frac{\frac{\partial \Phi_p}{\partial \boldsymbol{\Sigma}} : \mathbb{C}^{hom} : \dot{\mathbf{E}}}{H_{ep}}$$

with

$$H_{ep} = \frac{\partial \Phi_p}{\partial \boldsymbol{\Sigma}} : \mathbb{C}^{hom} : \frac{\partial G_p}{\partial \boldsymbol{\Sigma}} - \frac{\partial \Phi_p}{\partial f} \left( \frac{\partial G_p}{\partial \Sigma_m} \frac{1-f}{\rho} - t \frac{\boldsymbol{\Sigma} : \frac{\partial G_p}{\partial \boldsymbol{\Sigma}}}{(1-\rho) \left( Th + (t-T) \frac{\Sigma_m}{1-f} \right)} \right) + \frac{\partial \Phi_p}{\partial \rho} \rho \frac{\partial G_p}{\partial \Sigma_m} - \frac{\partial \Phi_p}{\partial T} \frac{\partial T}{\partial \tilde{\epsilon}^p} \frac{\boldsymbol{\Sigma} : \frac{\partial G_p}{\partial \boldsymbol{\Sigma}}}{(1-f)(1-\rho) \left( Th + (t-T) \frac{\Sigma_m}{1-f} \right)} \quad (\text{III .26})$$

After calculating the plastic multiplier, the macroscopic tangent elastic-plastic stiffness tensor  $\mathbb{C}^{tan}$  can also be determined such as  $\dot{\boldsymbol{\Sigma}} = \mathbb{C}^{tan} : \dot{\mathbf{E}}$ . Considering the plastic loading-unloading conditions, the expression for the tangent elastic-plastic stiffness tensor  $\mathbb{C}^{tan}$  can be calculated as:

$$\mathbb{C}^{tan} = \begin{cases} \mathbb{C}^{hom} & \text{if } \Phi_p < 0 \text{ or } \Phi_p = 0 \cup \dot{\Phi}_p < 0 \\ \mathbb{C}^{hom} - \frac{\mathbb{C}^{hom} : \frac{\partial G_p}{\partial \boldsymbol{\Sigma}} \otimes \frac{\partial \Phi_p}{\partial \boldsymbol{\Sigma}} : \mathbb{C}^{hom}}{H_{ep}} & \text{if } \Phi_p = 0 \cup \dot{\Phi}_p = 0 \end{cases} \quad (\text{III .27})$$

The equivalent plastic strain  $\dot{\tilde{\epsilon}}^p$  of the solid clay phase is finally calculated by considering the energy equivalence condition:

$$\dot{\tilde{\epsilon}}^p = \frac{\boldsymbol{\Sigma} : \dot{\mathbf{E}}^p}{(1-f)(1-\rho) \left[ Th + (t-T) \frac{\Sigma_m}{1-f} \right]} \quad (\text{III .28})$$

The evolution of porosity is determined by making use of the Kinematic condition [Shen et al., 2013a]:

$$\dot{f} = \frac{1-f}{1-\rho} \text{tr} \dot{\mathbf{E}}^p - (1-f) t \dot{\tilde{\epsilon}}^p \quad (\text{III .29})$$

It is found that the evolution of porosity is either related to the macroscopic plastic volumetric strain and the equivalent plastic strain of the solid clay phase at the microscopic scale.

### 3.2 Constitutive model for long-term behavior of clayey rocks

When clayey rocks are subjected to stress changes, a part of plastic deformation occurs instantaneously as described above. But another part evolves in time. Therefore, the time-dependent plastic deformation is seen as the delayed plastic one and here described in the viscoplastic theory. Both instantaneous and delayed plastic strains are described by a unified formulation [Farhat et al., 2017, Zhou et al., 2008]. The evolution of viscoplastic loading surface is delayed with respect to the plastic yielding surface. In order to describe this process, a specific viscoplastic hardening function is introduced and its evolution is lower than that of the instantaneous plastic hardening function given in III .13. Consequently, the viscoplastic loading function is expressed as follows:

$$\Phi_{vp}(\boldsymbol{\Sigma}, f, \rho, T_{vp}, \eta) = \Theta \Sigma_d^2 + \left( \frac{3f}{2T_{vp}^2} - 1 \right) \Sigma_m^2 + 2(1-f)h\Sigma_m - \frac{3+2f+3f\rho}{3+2f}(1-f)^2 h^2 \geq 0$$

with

$$\Theta = \frac{\frac{1+2f/3}{T_{vp}^2} + \frac{2}{3}\rho \left( \frac{3f}{2T_{vp}^2} - 1 \right)}{\frac{4T_{vp}^2 - 12f - 9}{6T_{vp}^2 - 13f - 6}\rho + 1} \quad (\text{III .30})$$

The viscoplastic hardening function  $T_{vp}$  verifies the condition  $T_{vp}(\tilde{\varepsilon}^p) \leq T(\tilde{\varepsilon}^p)$ . The evolution of  $T_{vp}(\tilde{\varepsilon}^p)$  is described by the same function as that for  $T(\tilde{\varepsilon}^p)$ :

$$T_{vp} = T_m(\eta) - (T_m(\eta) - T_0)e^{-b_{vp}\tilde{\varepsilon}^p} \quad (\text{III .31})$$

It is worth noticing that the viscoplastic hardening function is bounded by the maximum friction coefficient  $T_m(\eta)$ , given in III .20 as a function of loading orientation parameter  $\eta$ . Therefore, it is here assumed that the viscoplastic loading function exhibits the same anisotropic property as the plastic yield function. The parameter  $b_{vp}$  controls the evolution of viscoplastic hardening and fits the condition  $b_{vp} \leq b_1$ .

Under a constant stress state like in a creep test, the instantaneous plastic strains do not evolve. But the time-dependent plastic strains can evolve if  $\Phi_{vp} > 0$ . The value of  $T_{vp}$  increases with time and progressively approaches that of  $T$ . When  $T_{vp} = T$ , the plastic yield and viscoplastic loading surfaces coincide and the viscoplastic flow vanishes. One reaches the stationary state of viscoplastic flow. Similarly, the non-associated plastic potential III .22 is adapted for the viscoplastic deformation. Further, it is also assumed that the viscoplastic flow rule exhibits the same anisotropy than that of plastic one. The same dilatancy coefficient  $t$  is used for the viscoplastic potential. Thus, the viscoplastic

potential is given by:

$$G_{vp}(\boldsymbol{\Sigma}, f, \rho, T_{vp}, t, \eta) = \Theta \Sigma_d^2 + \left( \frac{3f}{2T_{vp}(\eta)t(\eta)} - 1 \right) \Sigma_m^2 + 2(1-f)h\Sigma_m - \frac{3+2f+3f\rho}{3+2f}(1-f)^2 h^2$$

with

$$\Theta = \frac{\frac{1+2f/3}{T_{vp}(\eta)t(\eta)} + \frac{2}{3}\rho \left( \frac{3f}{2T_{vp}(\eta)t(\eta)} - 1 \right)}{\frac{4T_{vp}(\eta)t(\eta)-12f-9}{6T_{vp}(\eta)t(\eta)-13f-6}\rho + 1} \quad (\text{III .32})$$

Thus the viscoplastic strains rates are given by:

$$\dot{\mathbf{E}}^{vp} = \dot{\lambda}_{vp} \frac{\partial G_{vp}}{\partial \boldsymbol{\Sigma}} \quad (\text{III .33})$$

The viscoplastic multiplier  $\dot{\lambda}_{vp}$  (in  $1/(Pa \cdot s)$ ) is here calculated by using the overstress concept and Perzyna formulation. The viscoplastic flow occurs only if  $\Phi_{vp} > 0$ . The viscoplastic multiplier is a function of the positive value of  $\Phi_{vp}$ . The following power is proposed:

$$\dot{\lambda}_{vp} = \frac{1}{\eta_1} \left( \frac{\langle \Phi_{vp} \rangle}{h^2} \right)^2 \quad (\text{III .34})$$

The parameter  $\eta_1$  (in  $Pa \cdot s$ ) represents the coefficient of viscosity controlling the initial creep rate while  $m$  is a parameter controlling the evolution of viscoplastic strain rate. The hydrostatic tensile yield stress  $h$  is here used to normalize the value of the loading function  $\Phi_{vp}$  in the power term. When the instantaneous plastic and time-dependent viscoplastic flows occur simultaneously, the equivalent plastic strain in the solid clay phase becomes:

$$\dot{\tilde{\epsilon}}^p = \frac{\boldsymbol{\Sigma} : \dot{\mathbf{E}}^p}{(1-f)(1-\rho) \left[ Th + (t-T) \frac{\Sigma_m}{1-f} \right]} + \frac{\boldsymbol{\Sigma} : \dot{\mathbf{E}}^{vp}}{(1-f)(1-\rho) \left[ T_{vp}h + (t-T_{vp}) \frac{\Sigma_m}{1-f} \right]} \quad (\text{III .35})$$

The evolution of porosity is accordingly given by:

$$\dot{f} = \frac{1-f}{1-\rho} \left( tr \dot{\mathbf{E}}^p + tr \dot{\mathbf{E}}^{vp} \right) - (1-f)t \dot{\tilde{\epsilon}}^p \quad (\text{III .36})$$

### 3.3 Description of damage

As mentioned above, clayey rocks are also susceptible to damage process due to the nucleation and propagation of micro-cracks [Bornert et al., 2010, Wang et al., 2015]. In this study, a micro-structure based modeling strategy is adopted. Damage is seen as a mechanism of microstructure evolution. More precisely, damage is directly related to interface debonding between mineral inclusions and porous clayey matrix at the meso-scopic scale. When an initially perfectly bonded inclusion is debonded, it is assumed to be completely

detached from the surrounding clayey matrix and behaves like a void, as shown in Figure III .6. Therefore, the debonding process leads to the increase of porosity and decrease of inclusion volume fraction. As a consequence, both the macroscopic elastic stiffness and plastic yield strength are weakened by the debonding-related damage process.

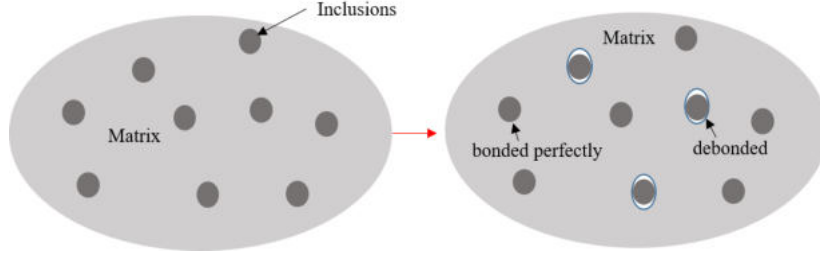


**Figure III .6:** Schematic representation of interfacial debonding process at the mesoscopic scale

Further, according to some previous studies [Shen and Shao, 2015a, Wang et al., 2015], the interface debonding is usually due to the strong strain and stress concentration around stiff inclusions. It is therefore reasonable to assume that the debonding-related damage process is driven by the strain difference (or contrast) between the inclusions and clayey matrix. For this purpose, the following scalar variable  $\hat{\epsilon}^{im}$  is introduced to represent the strain contrast:

$$\hat{\epsilon}^{im} = \sqrt{(\hat{\epsilon}^i - \hat{\epsilon}^m) : (\hat{\epsilon}^i - \hat{\epsilon}^m)} \quad (\text{III .37})$$

As defined above,  $\hat{\epsilon}^i$  and  $\hat{\epsilon}^m$  are respectively the local strain tensors of the merged inclusion phase and porous clayey matrix at the mesoscopic scale.

Further, it is assumed that the Kinetics of debonding process is controlled by the following Weibull's probability distribution function [Weibull, 1951]:

$$P_d = 1 - \exp \left[ - \left( \frac{\hat{\epsilon}^{im}}{S_0} \right)^M \right] \quad (\text{III .38})$$

$S_0$  and  $M$  are two parameters controlling the evolution of  $P_d$  from the perfectly bonded state ( $P_d = 0$ ) to fully debonded state ( $P_d = 1$ ). Then, the volume fraction of debonded inclusions  $\rho_d$  is given by:

$$\rho_d = \rho^{ini} P_d = \rho^{ini} \left\{ 1 - \exp \left[ - \left( \frac{\hat{\epsilon}^{im}}{S_0} \right)^M \right] \right\} \quad (\text{III .39})$$

$\rho^{ini}$  denotes the initial volume fraction of bonded inclusions. Accordingly, the current volume fraction of remaining bonded inclusions  $\rho$  and porosity  $f$  are calculated by:

$$\rho = \rho^{ini} - \rho_d, \quad f = \frac{f^{ini} + \rho_d}{1 - \rho} \quad (\text{III .40})$$

where  $f^{ini}$  denotes the initial value of porosity.

The key step here is the calculation of local strain tensors of the inclusion and porous clayey matrix,  $\hat{\boldsymbol{\varepsilon}}^i$  and  $\hat{\boldsymbol{\varepsilon}}^m$ . To this end and being consistent with the homogenization method used above for the macroscopic elastic properties, the two local strain fields are calculated by making use of strain concentration tensor. However, as a basic difference with the strain concentration tensor given in II .10 for the elastic homogenization, the repartition of macroscopic strain increment between the porous clayey matrix and inclusion phase is now affected by the plastic strain. In order to account for the plastic strain effect, the concept developed in the Hill's incremental method [Hill, 1965] for nonlinear composite materials is here employed. For this purpose, the rate form of constitutive model of the homogenized porous clayey matrix is expressed as follows:

$$\dot{\boldsymbol{\sigma}} = \mathbb{L}^{pm} : \dot{\boldsymbol{\varepsilon}} \quad (\text{III .41})$$

The fourth rank tensor  $\mathbb{L}^{pm}$  denotes the tangent elastic-plastic operator of the porous matrix, depending on plastic deformation history. This tensor can be strongly anisotropic. The calculation of the corresponding Hill's tensor becomes delicate. For the sake of efficiency for numerical implementation of the proposed model, and inspired by the previous studies devoted to incremental modeling of rock-like materials [Guéry et al., 2008, Shen and Shao, 2016, Shen et al., 2012b], the so-called isotropization procedure is here used. The basic idea is to extract an isotropic part from  $\mathbb{L}^{pm}$  so that the Hill's tensor can be easily calculated by using analytical formula and the extracted isotropic part. Among different isotropization methods available, the method proposed in [Bornert et al., 2001] is adopted here due to its mathematical and computing simplicity. Therefore, the isotropic part denoted as  $\mathbb{L}_{iso}^{pm}$  is extracted from  $\mathbb{L}^{pm}$  through the following operation:

$$\mathbb{L}_{iso}^{pm} = (\mathbb{J} :: \mathbb{L}^{pm}) \mathbb{J} + \frac{1}{5} (\mathbb{K} :: \mathbb{L}^{pm}) \mathbb{K} = 3k_t^{pm} \mathbb{J} + 2\mu_t^{pm} \mathbb{K} \quad (\text{III .42})$$

with

$$k_t^{pm} = \frac{1}{3} (\mathbb{J} :: \mathbb{L}^{pm}), \quad \mu_t^{pm} = \frac{1}{10} (\mathbb{K} :: \mathbb{L}^{pm})$$

By using this isotropic part  $\mathbb{L}_{iso}^{pm}$ , it is now possible to analytically calculate the Eshelby's tensor  $\mathbb{S}^{iso}$  and Hill's tensor  $\mathbb{P}^{iso}$  by the following relations:

$$\begin{aligned} \mathbb{S}^{iso} &= \frac{3k_t^{pm}}{3k_t^{pm} + 4\mu_t^{pm}} \mathbb{J} + \frac{6(k_t^{pm} + 2\mu_t^{pm})}{15k_t^{pm} + 20\mu_t^{pm}} \mathbb{K} \\ \mathbb{P}^{iso} &= \mathbb{S}^{iso} : (\mathbb{L}_{iso}^{pm})^{-1} \end{aligned} \quad (\text{III .43})$$

It is worth noticing that the isotropization method used here is similar to propositions of volumetric/deviatoric decompositions of anisotropic tensors reported in the literature,

for instance [Lebensohn et al., 2004]. Finally, by using again the Mori-Tanaka scheme, the rates of local strain tensors in the porous matrix and inclusion phase are calculated explicitly:

$$\dot{\boldsymbol{\varepsilon}}^m = \left[ (1 - \rho)\mathbb{I} + \rho \left( \mathbb{I} + \mathbb{P}^{iso} : (\mathbb{C}^i - \mathbb{L}_{iso}^{pm}) \right)^{-1} \right]^{-1} : \dot{\boldsymbol{E}} \quad (\text{III .44})$$

$$\dot{\boldsymbol{\varepsilon}}^i = \frac{1}{\rho} \left[ \dot{\boldsymbol{E}} - (1 - \rho)\dot{\boldsymbol{\varepsilon}}^m \right] \quad (\text{III .45})$$

Finally, the tangent elastic-plastic operator  $\mathbb{L}^{pm}$  can be calculated from the plastic flow rule of the homogenized porous matrix with the yield criterion (III .2). In consistency with the non-associative macroscopic plastic flow rule, the plastic flow rule of the homogenized porous matrix is also non-associative. The corresponding effective plastic potential is issued from the first step of homogenization with the modified secant method [Maghous et al., 2009]. It is expressed in the following form:

$$g^{pm}(\boldsymbol{\sigma}, f, T, t) = \frac{1 + 2f/3}{Tt} \sigma_d^2 + \left( \frac{3f}{2Tt} - 1 \right) \sigma_m^2 + 2(1 - f)h\sigma_m \quad (\text{III .46})$$

Accordingly, the evolution of equivalent plastic strain of the solid clay phase and that of porosity can be related to the plastic strain tensor of the homogenized porous matrix by:

$$\dot{\boldsymbol{\varepsilon}}^p = \frac{\boldsymbol{\sigma} : \dot{\boldsymbol{\varepsilon}}^p}{(1 - f) \left[ Th + (t - T) \frac{\sigma_m}{1 - f} \right]} \quad (\text{III .47})$$

$$\dot{f} = (1 - f) [tr\dot{\boldsymbol{\varepsilon}}^p - t\dot{\boldsymbol{\varepsilon}}^p] \quad (\text{III .48})$$

By using the plastic consistency condition  $\dot{\phi}^{pm} = 0$ , one can readily get:

$$\mathbb{L}^{pm} = \begin{cases} \mathbb{C}^{pm} & \text{if } \phi^{pm} < 0 \text{ or } \phi^{pm} = 0 \cup \dot{\phi}^{pm} < 0 \\ \mathbb{C}^{pm} - \frac{\mathbb{C}^{pm} : \frac{\partial g^{pm}}{\partial \boldsymbol{\sigma}} \otimes \frac{\partial \phi^{pm}}{\partial \boldsymbol{\sigma}} : \mathbb{C}^{pm}}{H_{ep}^{pm}} & \text{if } \phi^{pm} = 0 \cup \dot{\phi}^{pm} = 0 \end{cases}$$

with

$$H_{ep}^{pm} = \frac{\partial \phi^{pm}}{\partial \boldsymbol{\sigma}} : \mathbb{C}^{pm} : \frac{\partial g^{pm}}{\partial \boldsymbol{\sigma}} - \frac{\partial \phi^{pm}}{\partial f} \left( \frac{\partial g^{pm}}{\partial \sigma_m} (1 - f) - t \frac{\boldsymbol{\sigma} : \frac{\partial g^{pm}}{\partial \boldsymbol{\sigma}}}{\left( Th + (t - T) \frac{\sigma_m}{1 - f} \right)} \right) - \frac{\partial \phi^{pm}}{\partial T} \frac{\partial T}{\partial \varepsilon^p} \frac{\boldsymbol{\sigma} : \frac{\partial g^{pm}}{\partial \boldsymbol{\sigma}}}{(1 - f) \left( Th + (t - T) \frac{\sigma_m}{1 - f} \right)} \quad (\text{III .49})$$

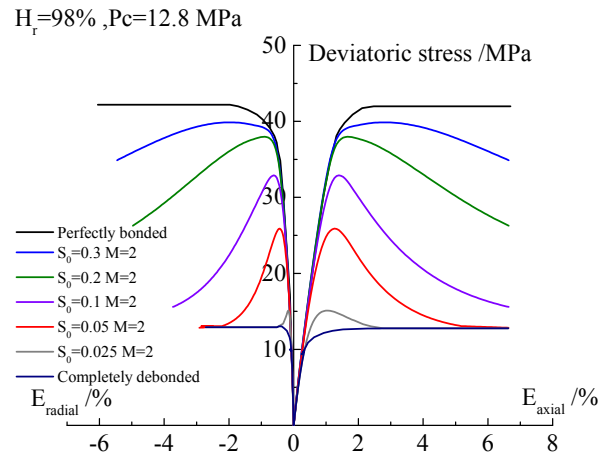
Macroscopic elastic stiffness tensor  $\mathbb{C}^{hom}$  varies with the value of porosity  $f$  and volume fraction of inclusion  $\rho$  (as shown in equation (II .9)). Therefore, the debonding process can change the macroscopic elasticity of clay rock. Thus, after the debonding process, we

need to put the updated macroscopic stiffness tensor  $\mathbb{C}^{hom}$  into the constitutive relation function to update the macroscopic stress and strain. The flowchart of the debonding calculation algorithm can be seen in Table III .1.

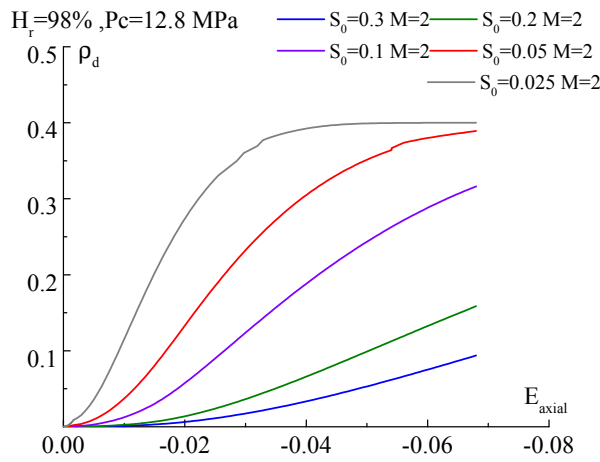
<b>Input</b>	$f^{ini}, \rho^{ini}, \mathbb{C}^i, \mathbb{C}^{pm} _n, \mathbb{C}^{hom} _n$
<b>Output</b>	$f _{n+1}, \rho _{n+1}, \mathbb{C}^{pm} _{n+1}, \mathbb{C}^{hom} _{n+1}$
(I)	Initialization: set $z = 0$ ; $\rho_d _{n+1}^z = \rho_d _n$ ; $\rho_p _{n+1}^z = \rho_p _n$
(II)	Calculate the deviatoric strain $\hat{\epsilon}^{im} _{n+1}^z$
(III)	Calculate distribution function: $P_d _{n+1}^z = 1 - \exp \left[ - \left( \frac{\hat{\epsilon}^{im} _{n+1}^z}{S_0} \right)^M \right]$
(IV)	Update $\rho_p _{n+1}^z$ : $\rho_p _{n+1}^z = \rho^{ini} (1 - P_d _{n+1}^z)$
(V)	Perform convergence chacking: If $ (\rho_p _{n+1}^z - \rho_p _{n+1}^{z-1}) / \rho_p _{n+1}^{z-1}  \leq TOL (i.e. 10^{-8})$ then   update the following parameters:   $\rho_d _{n+1} = \rho_d _{n+1}^z$ ; $\rho_p _{n+1} = \rho_p _{n+1}^z$ ;   $\hat{\epsilon}^{im} _{n+1} = \hat{\epsilon}^{im} _{n+1}^z$   $\rho _{n+1} = \rho^{ini} - \rho_d _{n+1}$ ; $f _{n+1} = \frac{f^{ini} + \rho_d _{n+1}}{1 - \rho}$ ;   Else   set $z=z+1$ , goto step (II)   End if
(VI)	Update the $\mathbb{C}^{pm} _{n+1}, \mathbb{C}^{hom} _{n+1}$
(VII)	End

Table III .1: Flowchart of debonding calculation algorithm

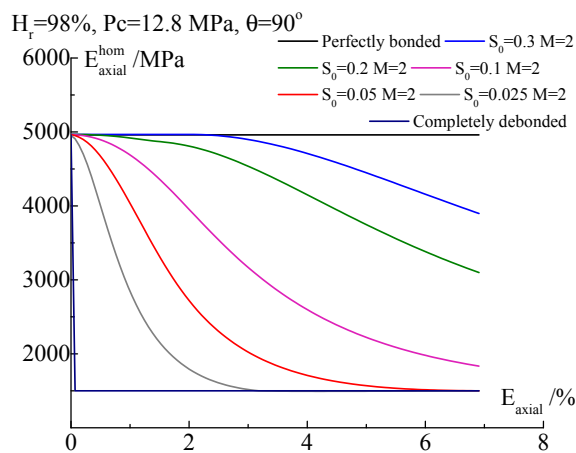
In order to show the influences of the damage parameters  $S_0$  and  $M$  on the overall mechanical behavior, in Figures III .7 and III .8, one shows the stress-strain curves, the volume fraction evolutions of debonded inclusions and Young's modulus in a triaxial compression test with different values of  $S_0$  and  $M$ .



(a) Stress-strain curves

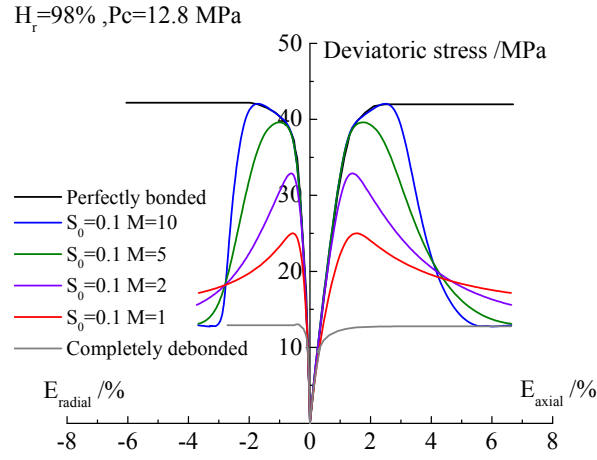


(b) Volume fraction of debonded inclusions  $\rho_d$

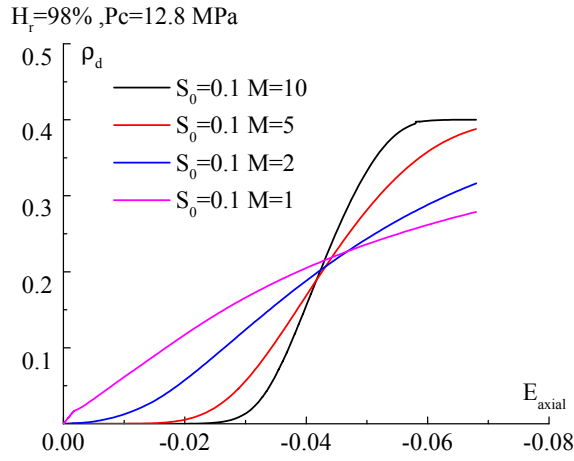


(c) Variation of macroscopic axial modulus

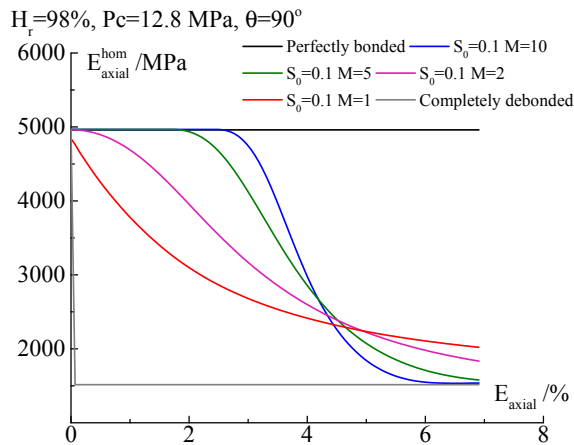
**Figure III .7:** Stress-strain curves and damage evolutions in triaxial compression test for different values of damage parameter  $S_0$



(a) Stress-strain curves



(b) Volume fraction of debonded inclusions  $\rho_d$



(c) Variation of macroscopic axial modulus

**Figure III .8:** Stress-strain curves and damage evolutions in triaxial compression test for different values of damage parameter  $M$

Due to the large number of parameters involved in this sensitivity simulation, the selected parameters are from Tables IV .1 and IV .2,  $S_0$  and  $M$  are not included in these Tables.

It is found that for a given value of  $M$ , a smaller value of  $S_0$  enhances the kinetics of interface debonding and thus damage process. With the progressive increase of debonded inclusion fraction, the material stiffness and strength are weakened, leading to the progressive softening of material. A more intuitive representation can be seen in the variation law of Young's modulus with different value of  $S_0$ . There is a transition from the perfectly bonded state to completely debonded state. The value of  $S_0$  largely affects the peak strength but almost not the post-peak softening rate.

On the other hand, for a given value of  $S_0$ , the change of  $M$  affects the evolution form of the debonded inclusion fraction. For a high value of  $M$ , the debonding starts very slowly but then increases suddenly to its maximum value, while for a low value of  $M$ , the debonding starts rapidly and then its evolution rate decreases. The value of  $M$  significantly affects both the peak strength value and the softening rate in the post-peak regime. In the same figures, we also show the variations of macroscopic axial elastic modulus, denoted as  $E_{axial}^{hom}$ , as functions of prescribed axial strain. One can see that the macroscopic elastic modulus is progressively deteriorated by the interface-debonding related damage evolution.

### 3.4 Effect of hydro-mechanical coupling on plastic deformation of clayey rocks

Due to the presence of clay minerals, the mechanical behavior of clay-rich rocks is generally sensitive to water saturation degree [Liu and Shao, 2016, Shen et al., 2014, Valès et al., 2004, Zhang, 2017]. At the same time, in many engineering applications, there exist both saturated and partially zones. For instance, during the excavation of an underground cavity in an initially saturated geological formation, a desaturated (or partially saturated) zone is created around the cavity. This zone can be further resaturated due to the water flow from the far-field. Therefore, the water saturation degree can vary in space and evolve in time. It is needed to take into account the influence of water saturation change on the mechanical behavior of clay-rich rocks.

In addition, the effects of hydro-mechanical coupling on the elastic properties of the anisotropic clayey rocks have been described in Chapter II . Therefore, this chapter will focus on the effect of hydraulic and mechanical coupling on the plastic deformation part.

The plastic behavior of clay-rich rocks is influenced by water saturation. Different

kinds of approaches have been proposed for modeling partially saturated soils and rocks, for instance by introducing extended effective stress [Coussy, 2004, Coussy et al., 1998] or using the so-called net stress concept [Alonso et al., 1990]. This concept has been successively applied to clays and clay-rich rocks [Jia et al., 2010] and it is also employed in this study. It is assumed that the plastic yield function  $\Phi_p$  in III .21 and potential  $G_p$  III .22 can be expressed in terms of the net stress tensor  $\Sigma'$  defined by:

$$\Sigma' = \Sigma + Bp_g \quad (\text{III .50})$$

Further, the plastic functions are also influenced by the capillary pressure or saturation degree. This dependency is usually identified from experimental evidences. For clay-rich rocks, as the water sensitivity of mechanical behavior is mainly attributed to the clay phase. Therefore, it is here assumed that the average value of maximum frictional coefficient  $\hat{T}_m$  is a function of the capillary pressure [Jia et al., 2010]:

$$\hat{T}_m(p_{cp}) = \hat{T}_{m0} \left( 1 + \beta_2 \frac{p_{cp}}{h} \right) \quad (\text{III .51})$$

where  $\hat{T}_{m0}$  is the value of  $\hat{T}_m$  for  $p_{cp} = 0$  at the saturated condition. The parameter  $\beta_2$  controls the variation  $\hat{T}_m$  and the cohesion  $h$  is again used to normalize the value of  $p_{cp}$ .

In a similar manner, the value of the dilatancy coefficient  $\hat{t}_m$  also depends on the capillary pressure through the same variation law:

$$\hat{t}_m(p_{cp}) = \hat{t}_{m0} \left( 1 + \beta_2 \frac{p_{cp}}{h} \right) \quad (\text{III .52})$$

where  $\hat{t}_{m0}$  is the value of  $\hat{t}_m$  for  $p_{cp} = 0$  at the saturated condition.

## 4 Conclusions

In combination with the previous Chapter II and this chapter, an anisotropic macroscopic elasto-plastic model was established for simulating the mechanical behavior of clayey rocks. In this chapter, both anisotropy and damage during loading were taken into account. In addition, viscoplastic parameters were introduced in this chapter to consider the time-dependent deformation. Also, the effects of hydro-mechanical coupling were also considered.

The macroscopic plastic criterion in this model can reflect the anisotropic deformation by assuming the maximum value of the frictional coefficient of the solid clay phase varies with the loading orientation. On the other hand, a non-associative macroscopic plasticity potential was established mainly to better describe the plastic volume strain. As for the

time-dependent deformation, the parameter  $b_{vp}$  was introduced to control the evolution of the viscoplastic hardening.

In the initial state, the mineral inclusions and the clay matrix were considered bonded perfectly. This model introduced Weibull's probability distribution function to estimate the damage degree. When the difference strain between the inclusions and porous matrix exceeded a certain value, it was considered that the inclusions have been separated from the porous matrix and it will no longer be loaded.

For the hydro-mechanical coupling of clay rock, this chapter established the relations between pore pressure with the maximum frictional coefficient  $\hat{T}_m$  of the clay rock.

The next Chapter IV will present several numerical simulation works. It will be shown that the simulation results have a good agreement with the experiments.



# Chapter IV

## Abaqus implementation, simulations of CO<sub>x</sub> claystone laboratory tests

### Contents

---

<b>1</b>	<b>Introduction</b>	<b>65</b>
<b>2</b>	<b>Identification of model's parameters</b>	<b>66</b>
2.1	Elastic parameters	66
2.2	Plastic, viscoplastic and damage parameters	68
2.3	Hydro-mechanical coupling parameters for partially saturated media	71
<b>3</b>	<b>Comparisons between numerical and experimental results</b>	<b>75</b>
3.1	Lateral decompression test	76
3.2	Triaxial compression tests with different water saturation	77
3.3	Time-dependent plastic deformation simulation results	80
<b>4</b>	<b>Conclusions</b>	<b>81</b>

---

### 1 Introduction

In France, clayey rocks are investigated as potential geological formations for underground waste disposal. Numerous experimental studies have been carried out on these clayey rocks. According to the mineralogical analysis [Robinet et al., 2012], the CO<sub>x</sub> claystone consists of 40% to 50% clay phase, 20% to 30% carbonate, and 20% to 30% quartz. The overall porosity varies from 11% to 14%. The majority of the pores are embedded in the

porous clay matrix. The local porosity can be calculated by dividing the volume of the pores by the volume of the porous clay matrix. The typical value is about  $f = 15\%$  to  $20\%$ . The detailed description of the distribution of mineral inclusions in the deep subsurface has been presented in Chapter I .

This chapter aims to simulate the laboratory experiments based on the multi-scale multi-physics anisotropic model (as shown in Chapters II and III ) and will analyze the influence of model parameters on the simulation results. For this chapter, two parts will be presented. The first part will focus on the determination of the model parameters. This part will be divided into the determination of the elastic-plastic parameters and the hydro-mechanical coupling parameters. The second part will deal with three different experimental tests, including the lateral decompression tests with different loading orientations, normal triaxial compression tests with different relative humidity, and creep tests.

## 2 Identification of model's parameters

The laboratory experiments of the specimens of COx claystone collected by ANDRA from the underground research laboratory (URL) at Bure in France at a depth of approximately 490m. And these specimens have an initial water content of 6.2%, an initial saturation of 90.4%, and an initial density of  $2.69g/cm^3$  in the laboratory environment.

### 2.1 Elastic parameters

According to the homogenization scheme employed in this thesis, the macroscopic elastic tensor in Equation II .9 is calculated based on the local elastic properties of the solid clay phase and inclusions, porosity, and the volume fraction of inclusions. For simplicity, it is assumed that the mineral particles consist of a mixed inclusion phase of quartz and carbonate with isotropic elastic behavior. The elastic properties of the inclusion phases can be estimated from literature [Guéry et al., 2008, Lide, 2004, Panet et al., 1976]. For instance, the typical values of Young's modulus and Poisson's ratio for calcite and quartz are equal to  $E_{calcite} = 95000MPa$ ,  $\nu_{calcite} = 0.27$  and  $E_{quartz} = 101000MPa$ ,  $\nu_{quartz} = 0.06$ , respectively. For simplicity, the equivalent inclusion phase is chosen with  $E_i = 98000MPa$  and  $\nu_i = 0.15$ , respectively [Shen et al., 2013a].

The values of porosity and volume fraction of inclusions are measured by the mineralogical analysis. The key issue in the calculation of macroscopic elastic stiffness tensor of clayey rocks of the anisotropic model is to determine the local elastic behavior of the solid

clay phase at the microscopic scale. The solid clay phase is considered to be transversely isotropic, and its elastic parameter values need to be determined. It is generally very difficult to measure these elastic parameters directly using microscopic tests. An alternative indirect method is usually adopted.

For this chapter, the values of five macroscopic elastic parameters (i.e.,  $E_1^{hom}$ ,  $E_3^{hom}$ ,  $\nu_{12}^{hom}$ ,  $\nu_{31}^{hom}$ ,  $G_{13}^{hom}$ ) are determined from the linear parts of stress-strain curves obtained from the macroscopic triaxial compression test (or other equivalent test). These tests take into account the different drilling orientations of the specimen relative to the bedding plane. Then, the average porosity and volume fraction of inclusion are measured. With these data mentioned above, the five elastic parameters of the solid clay phase (i.e.,  $E_1^s$ ,  $E_3^s$ ,  $\nu_{12}^s$ ,  $\nu_{31}^s$ ,  $G_{13}^s$ ) can be determined by numerically inverting of the relations II .8 and II .9.

$f = 0.16, \rho = 0.4, E^i = 98000MPa, \nu^i = 0.15, S_{lq} = 90.4\%$					
<b>Elastic</b>	$E_1^{hom}(MPa)$	$E_3^{hom}(MPa)$	$\nu_{12}^{hom}$	$\nu_{31}^{hom}$	$G_{13}^{hom}(MPa)$
Measured macroscopic value	8128	4919	0.34	0.27	1294
Solid clay phase	5160	2820	0.35	0.33	1060
Calculated macroscopic value	8275	4960	0.29	0.27	1273

**Table IV .1:** List of elastic parameters for transversely isotropic COx claystone

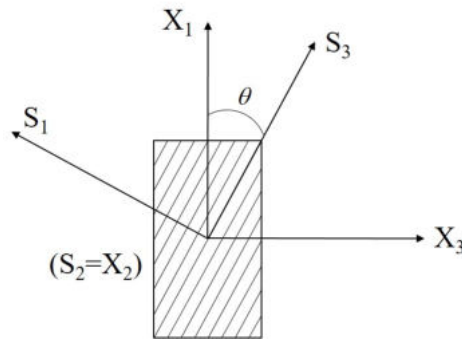


**Figure IV .1:** Definition of structural and global frames and loading orientation angle  $\theta$

Table IV .1 gives the typical elastic parameters values (corresponding to a relative humidity of 96%) for the samples in the laboratory conditions, including the measured experimental values of the macroscopic elasticity and the values calculated using the Equations II .8 and II .9. A quite good agreement is observed. The five elastic parameters

are defined in the structural frame  $(0, S_1, S_2, S_3)$ , as shown in Figure IV .1. The isotropic bedding plane is represented by the axis  $0S_2S_3$ , while the axis  $S_1$  is perpendicular to the bedding plane. In this figure, the loading orientation for the triaxial compression test  $\theta$  is defined by the angle between the axial stress ( $X_1$ -axis) and the bedding plane.

With the five elastic parameters (as shown in Table IV .1) in hand, it is possible to calculate the axial elastic modulus in any triaxial compression test by using the following relation [Niandou et al., 1997]:

$$\frac{1}{E_{axial}^{hom}(\theta)} = \frac{\sin^4\theta}{E_3^{hom}} + \left( \frac{1}{G_{13}^{hom}} - 2\frac{\nu_{12}^{hom}}{E_3^{hom}} \right) \sin^2\theta \cos^2\theta + \frac{\cos^4\theta}{E_1^{hom}} \quad (\text{IV .1})$$

It worth noting that the Equation IV .1 is derived from the Equation  $\mathbb{C}^{hom}(\theta) = \mathbb{A}^T : \mathbb{C}^{hom} : \mathbb{A}$ . Where the  $\mathbb{A}$  has already been described in Equation I .7.  $\mathbb{A}^T$  is the transpose matrix of  $\mathbb{A}$ .

In Figure IV .2, one compares the experimental values of the axial elastic modulus measured by triaxial compression tests under five different loading angles at a constant mean stress of  $12\text{MPa}$  with the values calculated by the Equation IV .1. The initial elasticity parameters are taken from the Table IV .1. As can be seen, the variation of axial modulus with loading orientation is correctly described.

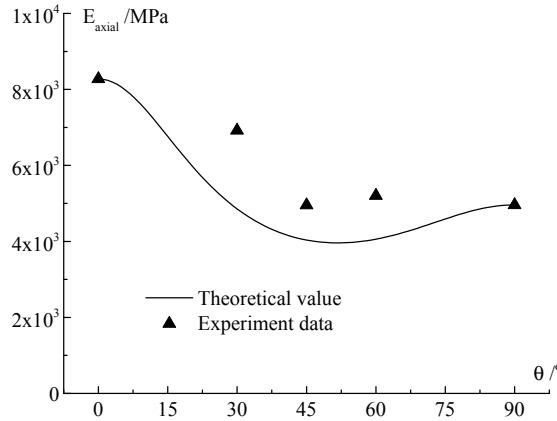


**Figure IV .2:** Variation of axial elastic modulus  $E_{axial}$ : comparison between theoretical values and experimental data ( $f = 0.16$ ,  $\rho = 0.4$ ,  $H_r = 96\%$ )

## 2.2 Plastic, viscoplastic and damage parameters

The plastic parameters in the proposed model include the initial and maximum frictional coefficients  $T_0$  and  $T_m$ , the hydrostatic tensile strength  $h$  and the plastic hardening

coefficient  $b_1$ . All these parameters are related to the solid clay phase. Like the elastic parameters, it is very difficult to carry out microscopic tests directly on the clay phase. The plastic parameters are also numerically fitted from macroscopic laboratory tests. It is well known that most clay materials have a very small initial plastic yield stress, and its value does not significantly affect the overall mechanical responses. Therefore a constant small value is here taken for the parameter  $T_0$ . For a given loading orientation (a given value of angle  $\theta$ ), the values of  $T_m$  and  $h$  can be conveniently calibrated from the peak stresses of triaxial compression tests. It is noticed that in the present study, the value of  $h$  is assumed to be independent of  $\theta$ . Only the value of  $T_m$  is dependent on  $\theta$ . As an example, one considers uniaxial compression tests along the axis  $X_1$  as shown in Figure IV .1, with the corresponding stress  $\Sigma_2 = \Sigma_3 = 0$ ,  $\Sigma_1 = \Sigma_{axial} < 0$ . Due to the transversely isotropy of material, the principal values of the fabric tensor verify  $\hat{a}_2 = \hat{a}_3 = -0.5\hat{a}_1$ . Thus, one gets:

$$\hat{a}_{ij}l_i l_j = \hat{a}_3(1 - 3l_1^2), \quad l_1^2 = \sin^2\theta \quad (\text{IV .2})$$

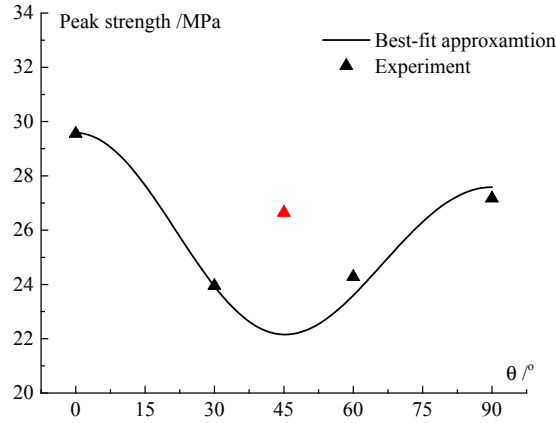
According to III .20, the variation of  $T_m$  with the loading angle  $\theta$  is given by:

$$T_m(\theta) = \hat{T}_m [1 + \hat{a}_3(1 - 3\sin^2\theta) + c_1(\hat{a}_2(1 - 3\sin^2\theta))^2 + c_2(\hat{a}_3(1 - 3\sin^2\theta))^3 + \dots] \quad (\text{IV .3})$$

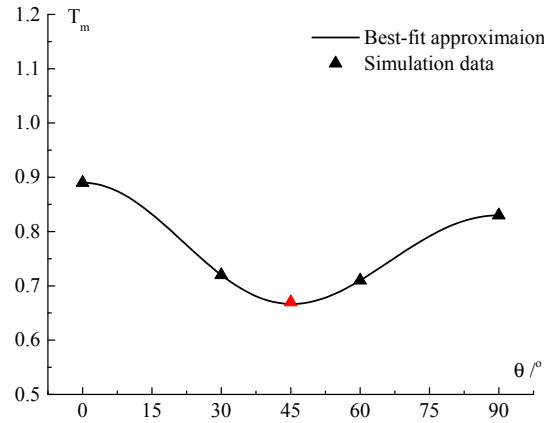
In practice, from the value of  $T_m$  identified from different values of  $\theta$ , it is possible to calibrate the values of  $\hat{T}_m$ ,  $\hat{a}_3$ ,  $c_1$  and  $c_2$ . For the COx claystone, in Figure IV .3(a), one shows the evolution of peak differential stress with loading orientation in triaxial compression tests with constant mean stress on the samples under  $H_r = 96\%$ . One can see that the maximum strength is obtained for  $\theta = 0^\circ$  (parallel to bedding planes) while the minimum one is found between  $\theta = 30^\circ$  and  $\theta = 60^\circ$ . However, the value for  $\theta = 45^\circ$  is abnormally high compared with those of  $\theta = 30^\circ$  and  $\theta = 60^\circ$ . This may be related to experimental artifact or a high volume fraction of quartz and carbonate in that sample (note that the mineralogy was not measured individually on each sample but on each batch drilled at a given depth). Thus, the value of peak strength for  $\theta = 45^\circ$  was not used for the calibration of the anisotropy parameters. In Figure IV .3(b), the variation of  $T_m$  with  $\theta$  is presented. It is found that the third-order approximation provides a good description of material anisotropy. Therefore, the values of  $\hat{T}_m$ ,  $\hat{a}_3$ ,  $c_1$  and  $c_2$  are calibrated and presented in Table IV .2.

Plastic	$T_0 = t_0 = 0.01, b_1 = b_2 = 150, h = 16MPa$
Viscoplastic	$\eta_1 = 10^{15}Pa.s, b_{vp} = 60, m = 2$
Debonding	$S_0 = 0.1, M = 2$
Anisotropy	$\hat{T}_m = \hat{t}_m = 0.69, \hat{a}_3 = 0.1362, c_1 = 7.63, c_2 = 4.52$

**Table IV .2:** Typical set of parameters for anisotropic COx claystone ( $f^{ini} = 0.16$ ,  $\rho^{ini} = 0.40$ ,  $H_r = 96\%$ )



(a) Peak strength



(b)  $T_m$

**Figure IV .3:** Variation of peak differential stress and corresponding  $T_m$

The hardening parameter  $b_1$  can be calibrated from the pre-peak parts of axial strain versus differential stress curves of triaxial compression tests. The parameters involved

in the plastic potential, namely  $t_0$ ,  $b_2$  and  $\hat{t}_m$  control the plastic volumetric strains. In practice, an associated plastic flow rule is first adopted by taking  $t_0 = T_0$ ,  $b_2 = b_1$  and  $\hat{t}_m = \hat{T}_m$ . Then, by comparing numerical results with experimental data in terms of volumetric or lateral strain, the values of these parameters can be eventually readjusted. For the case of COx claystone, it seems that the associated plastic flow rule provides satisfactory predictions. Finally, the damage parameters  $S_0$  and  $M$  mainly control the post-peak stress-strain curves. Their values are then calibrated from the post-peak parts in triaxial compression tests.

In Table IV .2, the typical set of parameters for the COx claystone is presented for the samples under the relative humidity of 96%. Finally, three parameters (i.e.,  $\eta_1$ ,  $b_{vp}$ ,  $m$ ) are involved in the viscoplastic law. They are generally fitted from the variation of strains during creep tests.

It should be noted that the determination of the model parameters in this chapter is based on the experimental results, and it is difficult to maintain the same saturation in laboratory experiments as *in situ* environment. Therefore, the initial saturation of experimental specimens in the laboratory often uses special methods to maintain a constant value of saturation close to that of the *in situ* environment.

### 2.3 Hydro-mechanical coupling parameters for partially saturated media

As mentioned above (Equations II .48, III .51 and III .52), the effect of water saturation on the mechanical behavior of clay-rich rocks is explained here in terms of the variation of the mean frictional coefficient  $\hat{T}_m$  and the perpendicular elastic modulus  $E_{\perp}^s$  of the solid clay phase at the microscopic scale. Their values are related to the macroscopic elastic modulus and peak strength.

Therefore, five triaxial compression tests are performed on the samples with different water contents obtained by the equilibrium with the different values of the relative humidity of salt solution around the samples (i.e. 15%, 59%, 70%, 85% and 98%). All the samples were drilled in the perpendicular direction with  $\theta = 90^\circ$ .

From these tests, the values of macroscopic axial modulus and different peak strengths were measured. By using the analytical relations issued from homogenization for the elastic stiffness tensor and peak strength presented above, the corresponding values of  $E_{\perp}^s$  and  $\hat{T}_m$  are calculated for each value of relative humidity, as shown in Table IV .3. The values from the triaxial tests with constant mean stress and under  $H_r = 96\%$  are also added. From all these values, it is now readily to calibrate the values of the parameters

( $E_{\perp}^s$ ,  $\hat{T}_{m0}$ ,  $\beta_1$  and  $\beta_2$ ), as given in Table IV .3.

$H_r/\%$	15	59	70	85	96	98
$E_{\perp}^s/MPa$	3950	3084	2964	2956	2820	2781
$\hat{T}_m = \hat{t}_m$	1.18	0.79	0.76	0.70	0.69	0.62
$E_{\perp 0}^s = 2769MPa$ , $\hat{T}_{m0} = \hat{t}_{m0} = 0.62$ , $\beta_1 = -0.025$ , $\beta_2 = -0.061$						

**Table IV .3:** Typical values of parameters for partially saturated materials

In Figure IV .4, one shows the fitting of the variations of  $E_{\perp}^s$  and  $\hat{T}_m$  with capillary pressure. In order to appreciate the effect of water saturation on the macroscopic mechanical behavior, in Figure IV .5, one shows the stress-strain curves for triaxial compression tests on samples under different values of relative humidity. And the parameters of the model for this simulation test are taken from the Tables IV .1 and IV .3. It is found that the saturation degree significantly affects the peak strength, the pre- and post-peak responses. There is a transition from ductile to brittle behavior when the samples are dried.

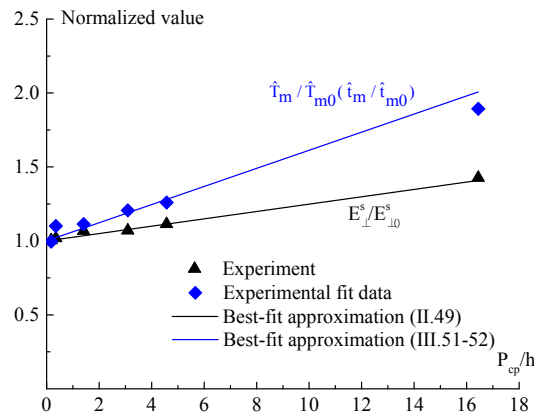


**Figure IV .4:** Evolution of  $\hat{T}_m$  and  $E_{\perp}^s$  with capillary pressure calculated from relative humidity

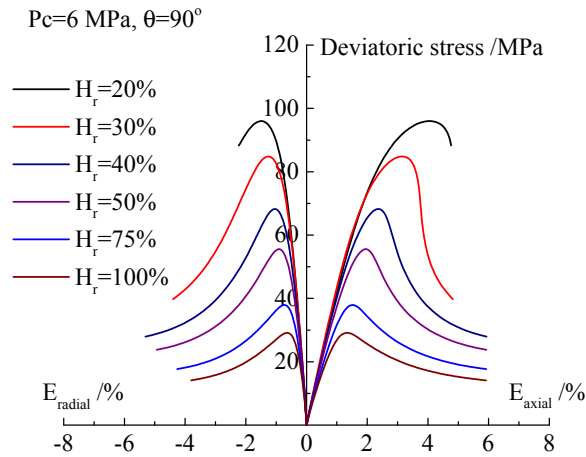


**Figure IV .5:** Influence of relative humidity or water content on macroscopic stress-strain responses in triaxial compression tests on perpendicular samples ( $\theta = 90^\circ$ )

In order to verify the correctness of the ABAQUS simulation of hydro-mechanical coupling, two different classical consolidation tests are simulated.

**Consolidation test simulation**

This section presents a one-dimensional consolidation test simulation. As shown in Figure IV .6, the deformation of the sides and bottom of the cubic column is fixed, and then a load is applied to the top surface.

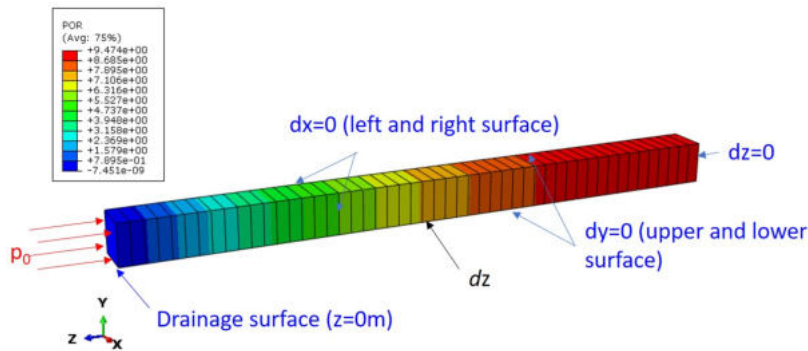


**Figure IV .6:** Schematic of one dimensional consolidation

The Young's modulus and Poisson's ratio are provided as  $100MPa$  and  $0.33$ , respectively. The hydraulic conductivity is equal to  $9.996 \times 10^{-6}m/s$ , with the initial void ratio of  $0.556$ . It is assumed that the fluid is incompressible and therefore, the Biot's coefficient

is equal to 1.

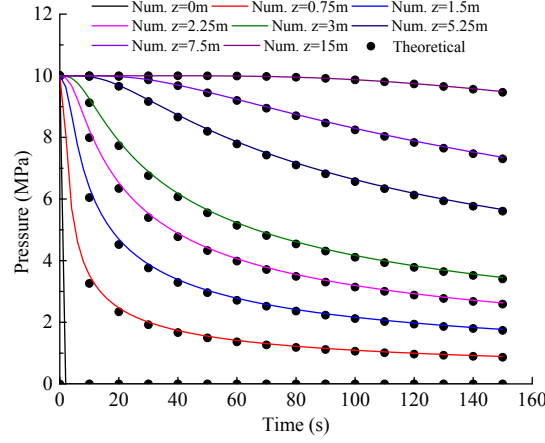


**Figure IV .7:** Pore pressure dissipation law with boundary drainage

As in Figure IV .7, a good agreement is attained between the consolidation simulation results with the theoretical values. The theoretical values of pore pressure at any position ( $z$ ) and any time ( $t$ ) are derived from [Biot, 1941] by the following equation:

$$p_l(z, t) = \frac{4P_0}{\pi} \sum_{n=0}^{\infty} \frac{1}{2n+1} \sin\left(\frac{(2n+1)\pi \cdot z}{2n}\right) \cdot \exp\left(-\frac{(2n+1)^2 \pi^2}{4} T_v\right) \quad (\text{IV .4})$$

with

$$T_v = \frac{C_v \cdot t}{n^2}, \quad C_v = \frac{K \cdot E_s}{\gamma_l}, \quad E_s = E / \left(1 - \frac{2\nu^2}{1-\nu}\right) \quad (\text{IV .5})$$

where  $T_v$  represents the time factor,  $C_v$  ( $m/s$ ) represents the consolidation coefficient, and  $E_s$  ( $Pa$ ) represents the compression modulus of soil.

### Consolidation test simulation considering different Biot's coefficient

Biot's coefficient in ABAQUS is equal to 1 in the initial state. For soil materials, the Biot's coefficient is close to 1. In the case of rocks, the Biot's coefficient is often less than 1. Therefore, the condition of  $b < 1$  needs to be considered.

As shown in Figure IV .8, triaxial compression simulations are performed on the units with different Biot's coefficient values. The Young's modulus and Poisson's ratio of this isotropic material are equal to  $E = 10000MPa$  and  $\nu = 0.25$ , and hydraulic conductive  $K = 10^{-9}m/s$ . By adjusting the bulk modulus of solid, the simulation results for different Biot's coefficient conditions are obtained (as shown in Figure IV .9).

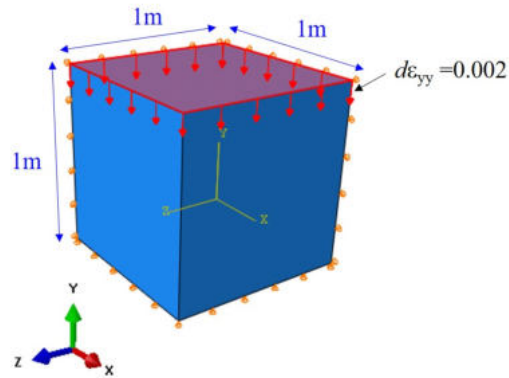


Figure IV .8: Schematic of one unit for different Biot's coefficient conditions

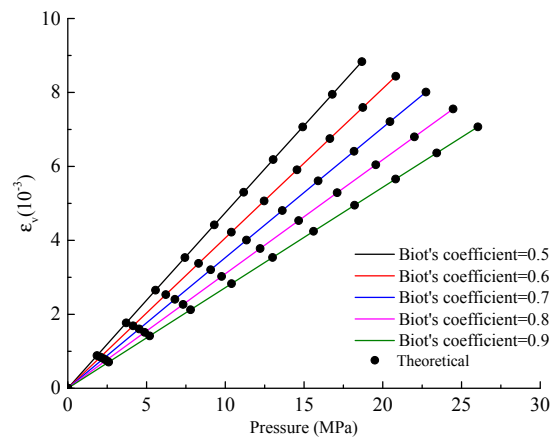
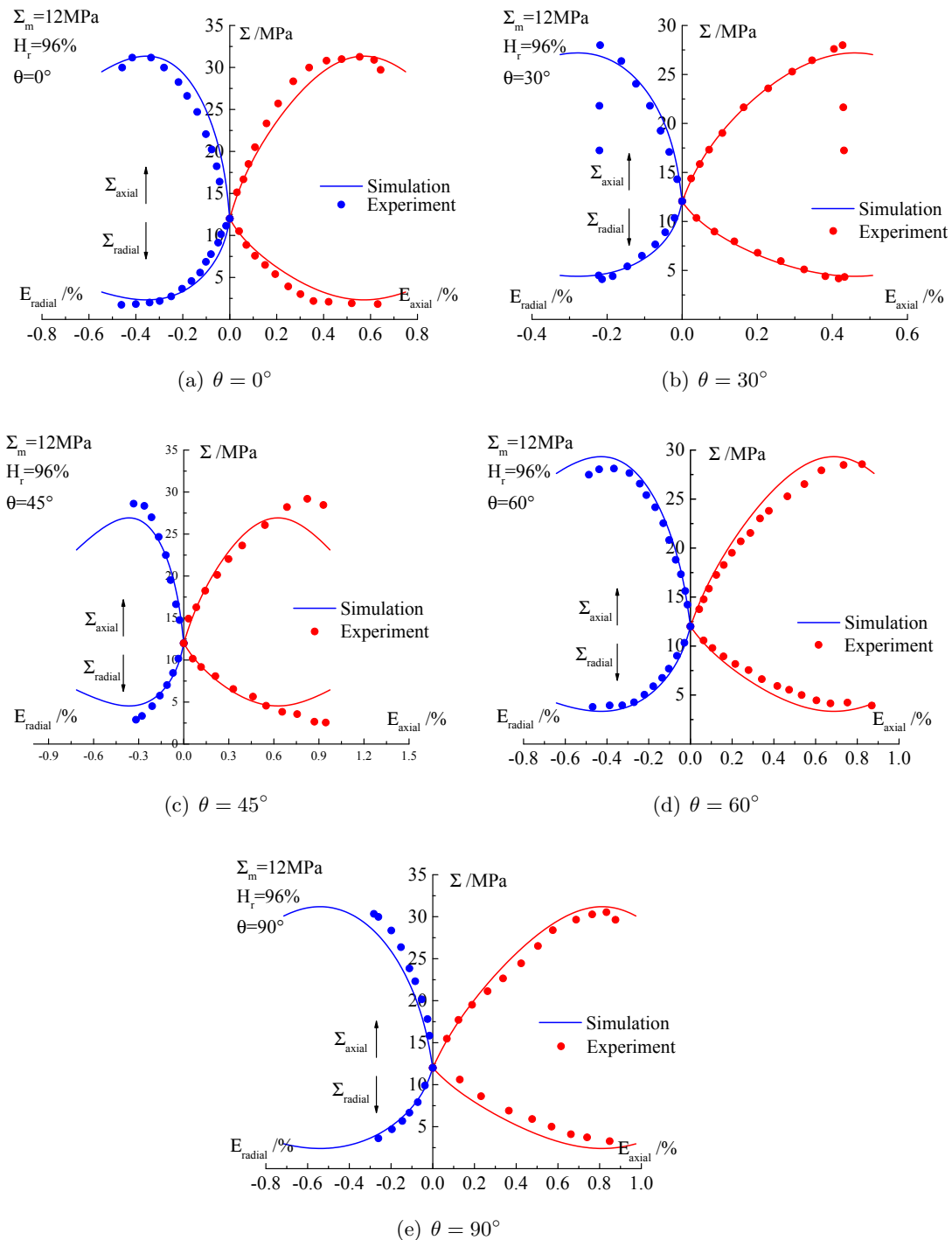


Figure IV .9: Consolidation consider different Biot's coefficient considtions

### 3 Comparisons between numerical and experimental results

In this section, a series of laboratory experimental tests on the COx claystone, including lateral decompression tests, triaxial compression tests with different water saturation, and creep tests, are carried out by using the multi-scale mechanical model and the parameters determined above. The comparisons of the numerical simulation results with the experiments are also presented.

## 3.1 Lateral decompression test



**Figure IV .10:** Stress-strain curves in lateral decompression tests with different loading angles  $\theta$ : comparison between model's predictions and experimental data

This part is about the lateral decompression test. The lateral decompression test is a particular triaxial compression test with a constant mean stress. In this test, the sample is first subjected to a hydrostatic stress or confining pressure. Then, the axial stress is increased while the lateral stress or confining pressure is decreased by keeping the mean stress unchanged. This stress path is seen as relevant for representing stress changes around a cavity during excavation.

In the present study, five tests are performed on the samples with different drilling orientations, i.e.  $\theta = 0^\circ, 30^\circ, 45^\circ, 60^\circ$  and  $90^\circ$ . All the samples are equilibrated with a relative humidity of 96%. The values of the elastic and plastic parameters are selected from Tables IV .1, IV .2, and IV .3. The constant mean stress used is  $P_c = 12MPa$ . The comparisons between model's simulations and test data are presented in Figure IV .10.

In a general way, one observes a good concordance. The main features of COx claystone behavior are correctly reproduced by the proposed model. In particular, the influence of structural anisotropy or loading orientation on the claystone behavior is well taken into account. The material softening due to induced damage is also properly described.

### 3.2 Triaxial compression tests with different water saturation

The influence of water content on the mechanical behavior of COx claystone is now considered. For this purpose, five triaxial compression tests are performed on the perpendicular samples with  $\theta = 90^\circ$ , and which are equilibrated with different values of relative humidity, namely 15%, 59%, 70%, 85% and 98%. The confining pressure used in these tests is  $12.8MPa$ . And the values of the elastic and plastic parameters are selected from Tables IV .1, IV .2, and IV .3.

In Figure IV .11, the macroscopic stress-strain curves are presented. One can see that the model's predictions are globally in good agreement with the experimental data for all the tests. It seems that the influences of water content on the elastic and plastic properties of the claystone are correctly taken into account by the proposed model. Moreover, in order to verify the impact of confining stress, two other tests are carried out on the nearly saturated samples with  $H_r = 98\%$ , and respectively under a confining pressure of  $8MPa$  and  $4.5MPa$ . The comparisons between the numerical and experimental results are provided in Figure IV .12. Again, a quite good concordance is observed. The proposed model is able to consider the effect of confining pressure on the macroscopic mechanical behavior of the claystone. However, in some tests, quite large scatters are observed between the numerical and experimental results in the pos-peak regime. It should be pointed out that the mechanical response of tested sample in the pos-peak regime is driven by several

factors.

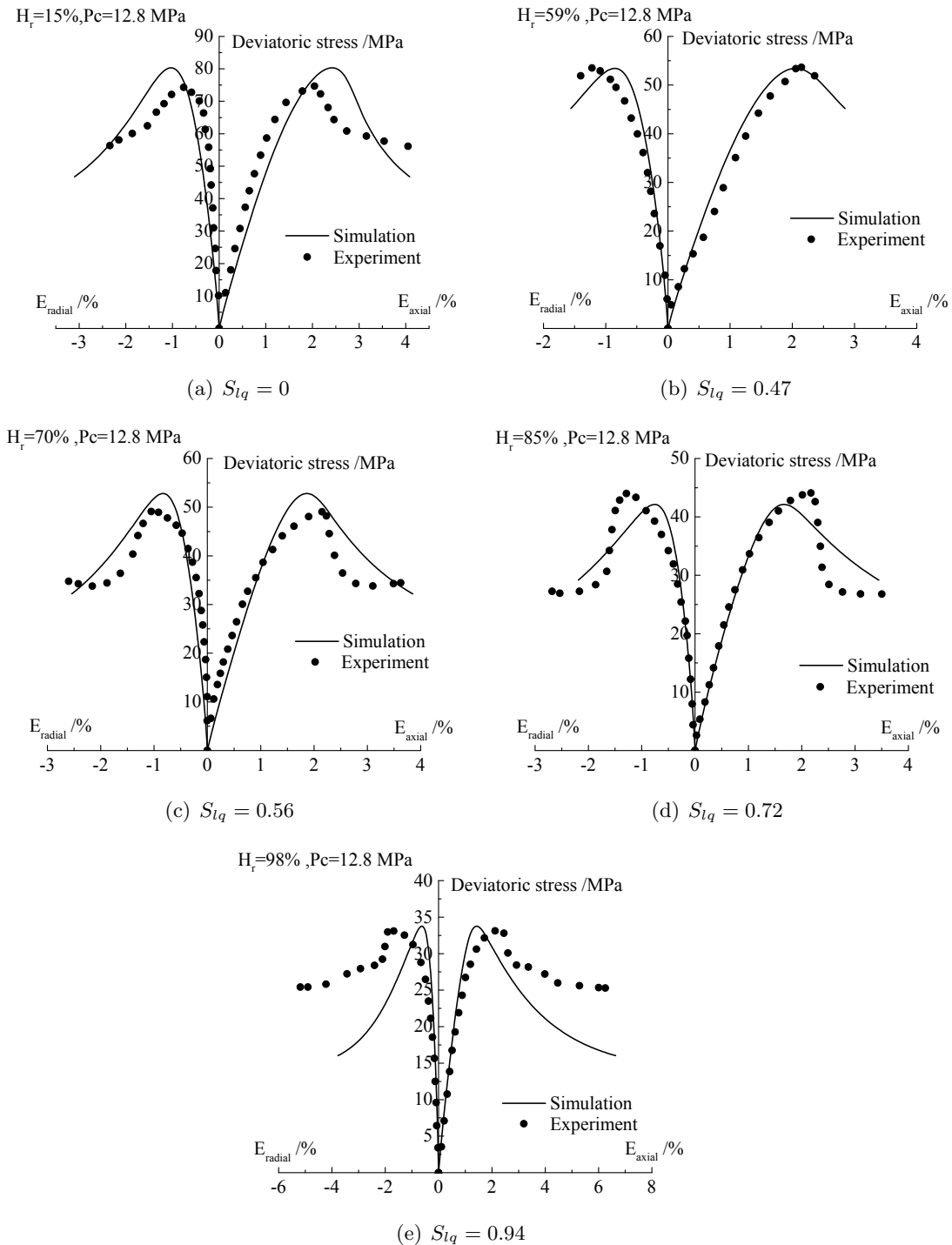
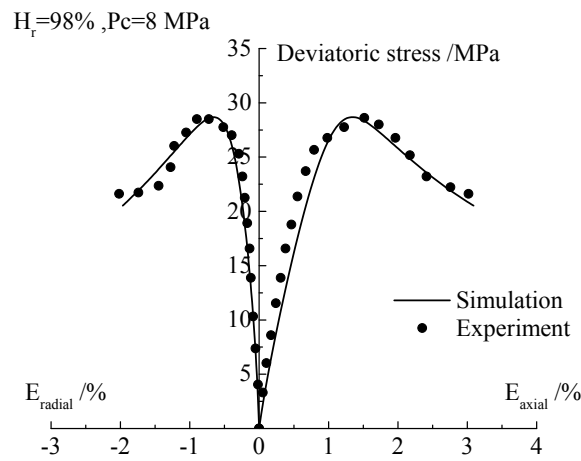
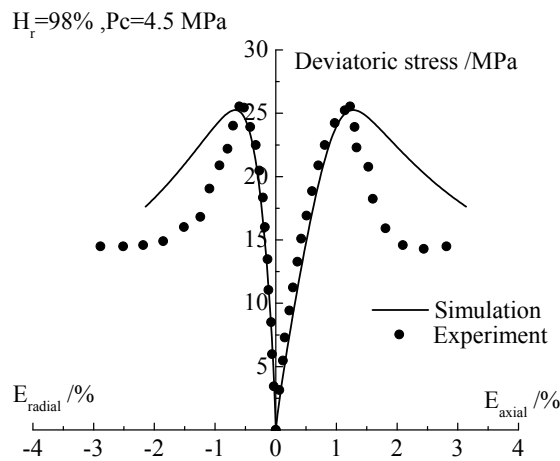


**Figure IV .11:** Mechanical responses in triaxial compression tests on perpendicular samples ( $\theta = 90^\circ$ ) equilibrated with values of relative humidity

In general, there is the onset of strain localization bands or macroscopic fractures. After the onset of such discontinuity surfaces, the tested sample cannot be any longer considered as a representative material volume, but it behaves rather like a small structure subjected to specific boundary conditions. The macroscopic responses of this structure should be determined by solving an appropriate boundary values problem by using a suitable numerical method able to deal with discontinuous fields. This feature will be considered in future studies.



(a)  $P_c = 8 \text{ MPa}$

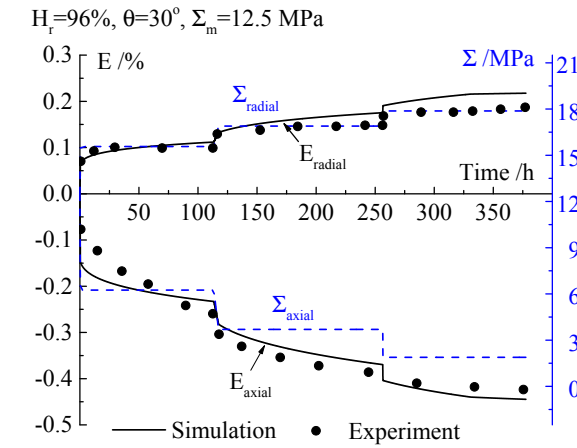
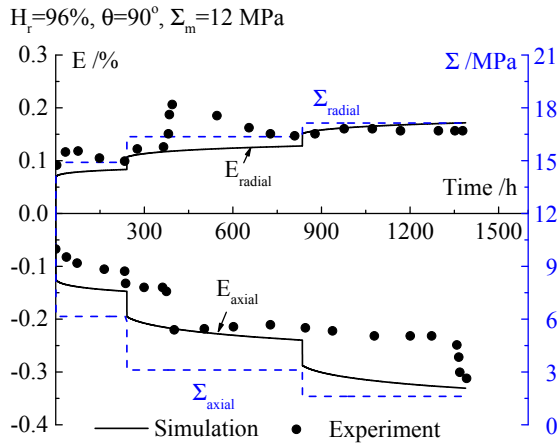


(b)  $P_c = 4.5 \text{ MPa}$

**Figure IV .12:** Mechanical responses on triaxial compression tests under two different confining pressure and on perpendicular samples ( $\theta = 90^\circ$ ) equilibrated with  $H_r = 90\%$

### 3.3 Time-dependent plastic deformation simulation results

Finally, the time-dependent strain of claystone is investigated. For this purpose, creep tests under different stress levels are performed on the samples respectively drilled in  $\theta = 30^\circ$  and  $\theta = 90^\circ$ , and with a water saturation degree corresponding to  $H_r = 96\%$ . All the creep tests are performed under a constant mean stress. In practice, the samples are first subjected to an initial confining stress, namely  $12\text{MPa}$  or  $12.5\text{MPa}$ . The axial stress is then decreased to a desired value while the radial one is accordingly increased so that the mean stress remains unchanged. The stresses are then kept constant for a period and the variations of axial and radial strains are measured.

(a)  $\theta = 30^\circ$ (b)  $\theta = 90^\circ$ 

**Figure IV .13:** Evolution of axial strain and radial strain in two creep tests with different loading orientation angles  $\theta$  and  $H_r = 96\%$

The stress steps adopted in two creep tests are detailed in Table IV .4. And the model's parameters are selected from Tables IV .1, IV .2, and IV .3.

The evolutions of strains predicted by using the proposed model are compared with experimental data in Figures IV .13(a) and IV .13(b). The sharp changes of strains in the figures correspond to the instantaneous variations induced by the stress increases. Despite some scatters, in particular for  $\theta = 90^\circ$ , one can observe a quite good agreement between the numerical results and experimental data. It is noted that important fluctuations are obtained in experimental data. This is mainly due to the disturbances of environmental conditions such as temperature variation. More creep tests will be welcome in order to get a deep validation of the proposed model.

$\theta(^{\circ}) = 30$	$\Sigma_{axial}(MPa) = 12.5 \xrightarrow{\text{moment}} 6.25 \xrightarrow{\text{creep}} 6.25 \xrightarrow{\text{moment}} 3.69 \xrightarrow{\text{creep}} 3.69 \xrightarrow{\text{moment}}$ $1.88 \xrightarrow{\text{creep}} 1.88$ $\Sigma_{radial}(MPa) = 12.5 \xrightarrow{\text{moment}} 15.63 \xrightarrow{\text{creep}} 15.63 \xrightarrow{\text{moment}} 16.91 \xrightarrow{\text{creep}} 16.91 \xrightarrow{\text{moment}}$ $17.81 \xrightarrow{\text{creep}} 17.81$ total creep time=377.44h
$\theta(^{\circ}) = 90$	$\Sigma_{axial}(MPa) = 12.0 \xrightarrow{\text{moment}} 6.15 \xrightarrow{\text{creep}} 6.15 \xrightarrow{\text{moment}} 3.11 \xrightarrow{\text{creep}} 3.11 \xrightarrow{\text{moment}}$ $1.62 \xrightarrow{\text{creep}} 1.62$ $\Sigma_{radial}(MPa) = 12.0 \xrightarrow{\text{moment}} 14.90 \xrightarrow{\text{creep}} 14.90 \xrightarrow{\text{moment}} 16.36 \xrightarrow{\text{creep}} 16.36 \xrightarrow{\text{moment}}$ $17.14 \xrightarrow{\text{creep}} 17.14$ total creep time=1389.78h

**Table IV .4:** Condition of the creep test ( $H_r = 96\%$ )

## 4 Conclusions

In this chapter, several experiments were simulated using the multi-scale anisotropy model presented in previous chapters. The performance between the simulation results and the experimental results showed a good agreement.

The experimental simulations in this chapter considered the features of multi-scale anisotropic model proposed in the previous chapters, and the effects of the sample loading orientation and water saturation on its physical-mechanical properties were considered during the simulations. In addition, viscoplastic parameters were introduced in this chapter to account for the time-dependent deformation. The simulations include moment triaxial compression tests and creep tests, and there were good agreement between the simulation and experimental results. And some conclusions were obtained: Firstly, water

saturation weakens the strength of clay rocks. Secondly, the elasticity of clay rocks does not change much with increasing water saturation when the water saturation exceeds a certain value. Plasticity increases significantly with increasing water saturation. Finally, the viscoplastic deformation has a delayed character and increases with creep time.

# Chapter V

## Simulations of in-situ experiments

### Contents

---

<b>1</b>	<b>Introduction</b>	<b>83</b>
<b>2</b>	<b>Background and research objectives</b>	<b>84</b>
<b>3</b>	<b>Presentation of excavation model</b>	<b>88</b>
3.1	Identification of elastic, plastic and viscoplastic parameters	88
3.2	Boundary conditions	90
3.3	Verification of numerical accuracy	94
<b>4</b>	<b>Numerical modeling of excavation deformation zones</b>	<b>95</b>
4.1	Excavation simulations under purely mechanical conditions	95
4.2	Excavation simulations under hydro-mechanical coupling conditions	99
<b>5</b>	<b>Conclusions</b>	<b>105</b>

---

### 1 Introduction

For the disposal of nuclear waste, deep burial is now recognized as one of the reliable methods to prevent pollution of the surrounding environment. It is important to study the stability of the surrounding rocks around the gallery. As shown in Figure I .1, different galleries are excavated at a certain depth to study the deformation and stress distribution around the gallery.

This chapter is mainly to simulate the stresses and deformations in the clayey rocks around the gallery caused by the excavation. These simulations are based on the multi-scale model presented in previous chapters. The model's parameters have been determined in Chapter IV , except for the elastic parameters and the frictional coefficient (i.e.,  $\hat{T}_m$

and  $\hat{t}_m$ ), which need to be updated. In this chapter, three sections will be presented. The first section will present the background of gallery excavation construction and the research objectives of this chapter. The second section will present the simulation model, including parameter determination, introduction of the boundary conditions of the excavation model, and verification of the model's accuracy. The last section will present the simulation results on the clayey rocks surrounding the excavation gallery, including stress and deformation distribution. This chapter will also consider the effects of hydraulic and mechanical coupling on the clayey rocks.

## 2 Background and research objectives

For the excavation simulations in this chapter, it is important to characterise the mechanical and hydraulic coupling properties of rocks (i.e., clay-rich rocks) and their response to different excavation directions. ANDRA has conducted many *in situ* and laboratory experiments on gallery at depths of 445m and 490m (as shown in Figure I .1). And many investigations have been completed on the development of fracture zones near the gallery wall.

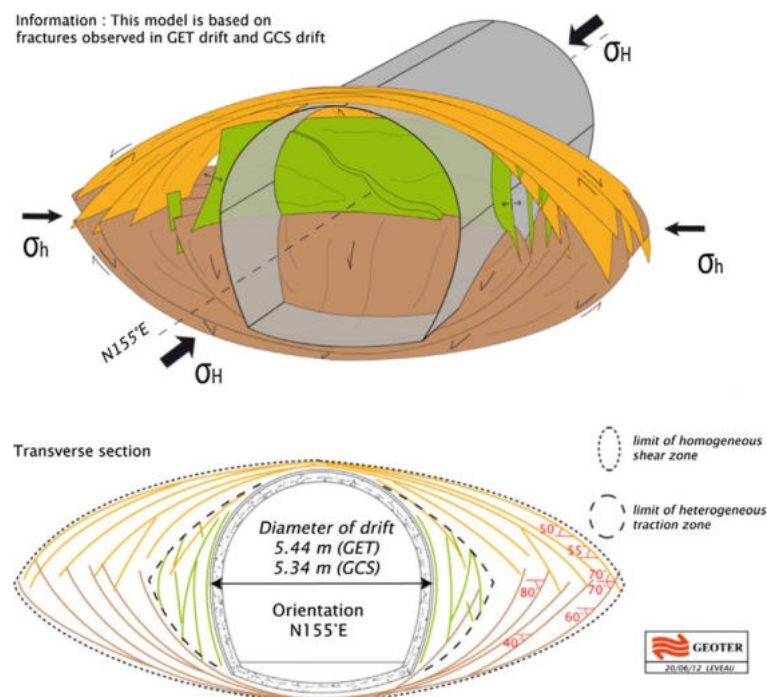


**Figure V .1:** Conceptual model of the fracture networks around the gallery along the major stress  $\sigma_H$  direction (Armand et al. [2014])

According to the mineralogical analysis of the COx claystone by Armand et al. [2014], the minerals include 55% of I/S (illite–smectite interstratified minerals), 30% of illite, and 15% of kaolinite and chlorite. The average porosity of claystone is equal to  $18 \pm 1\%$  at the main level (490m depth). In the *in situ* experiments of Wileveau et al. [2007], the anisotropy of the clay-rich rocks in the excavation layer was verified. The results shown that the orientation range of the major principal stress ( $\sigma_H$ ) is N150E $\pm$ 10° at a depth of 490m, which is greater than the stress in the other directions. The horizontal minor principal stress ( $\sigma_h$ ) is almost equal to the vertical stress ( $\sigma_v$ ). The ratio of the major stress to the minor stress is close to 1.3.

Due to the anisotropy of the claystone, the types of fractures and displacements caused by excavation in different directions are theoretically different. Figures V .1 and V .2 show the development of fractures around the gallery caused by excavation along  $\sigma_H$  and  $\sigma_h$ , respectively.

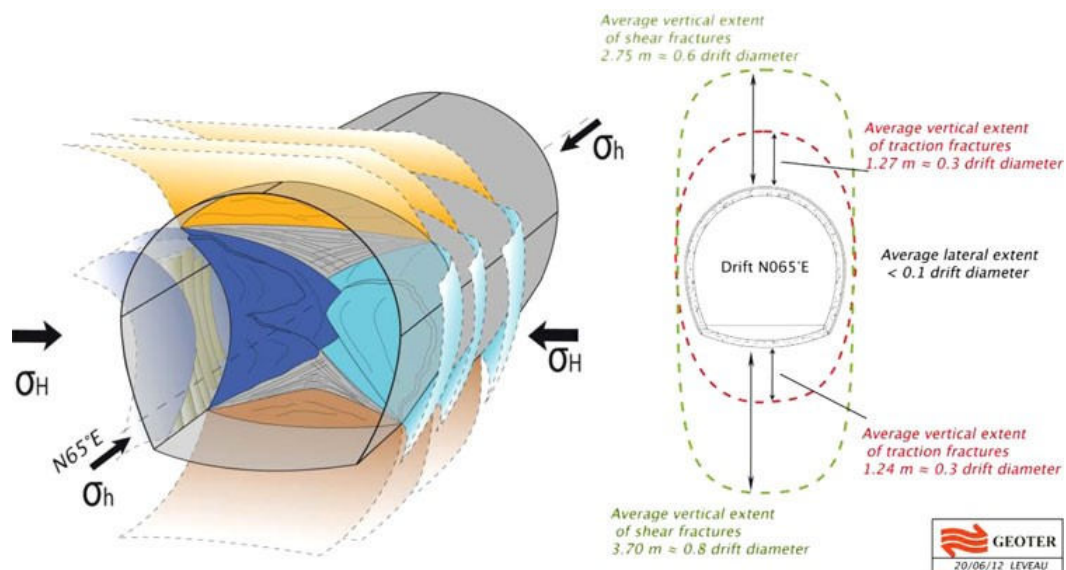


**Figure V .2:** Conceptual model of the fracture networks around the gallery along the minor stress direction. (Armand et al. [2014])

It can be found that shear and traction fracture zones occur mainly in the horizontal direction when the excavation direction is along with the major stress ( $\sigma_H$ ). The shear fractures extend over about 0.8 times of drift diameter. The traction fractures zone is relatively small. When the excavation direction is along with the minor stress ( $\sigma_h$ ), the shear and tensile fractures occur mainly in the vertical direction. And the extent of the impact of excavation is shown in Figure V .2.

In order to quantify the changes in pore pressure and deformation of the clayey rocks around the gallery wall, many different types of test instruments were fixed around the tested gallery at least two months before excavation. And these instrumentations are used to record the displacement field, stress field, and pore pressure field of the clay-rich rocks around the gallery. As shown in Figure V .3, there are 15 instrumentation boreholes that are drilled in the surrounding drifts (i.e., GAT and GLS). As shown in this figure, nine boreholes are used to measure the pore pressure around the GCS drift, covering an area from the GCS gallery wall to 50m away. These boreholes are marked in blue color as OHZ1521, OHZ1522, OHZ1523, OHZ1524, OHZ1525, OHZ1526, OHZ1121, OHZ1122, OHZ1123. In addition, there are three extensometers to measure radial and axial displacements in the horizontal plane and three inclinometers to measure vertical displacements. They are OHZ1501, OHZ1502, OHZ1701, OHZ1111, OHZ1511, and OHZ1512. In addition, there are a number of boreholes that are not shown in this figure.

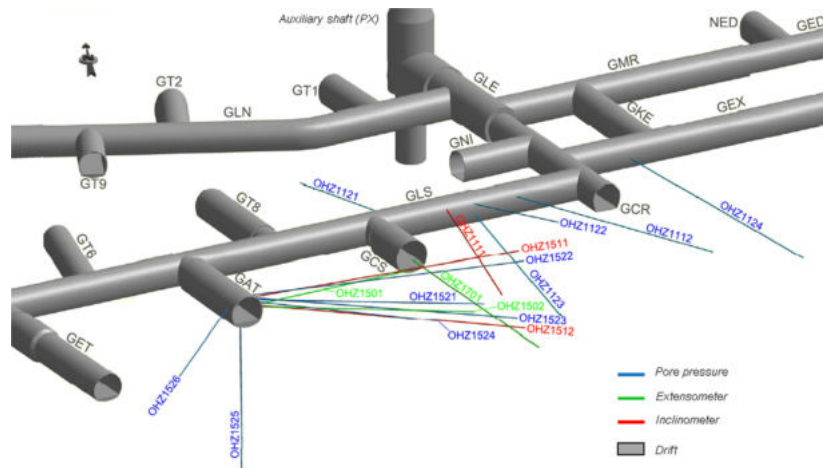


**Figure V .3:** Schematic diagram of the boreholes for GCS gallery experimental testing ([Armand and Su, 2006])

The hydraulic conductivity of the GCS gallery was measured by several boreholes with a length of 6m from gallery wall, as shown in Figure V .4. In Figure V .4(a) shows that the maximum vertical hydraulic conductivity of clayey rocks near the gallery wall reaches about  $8 \times 10^{-8} \text{m/s}$ . The vertical hydraulic conductivity decreases from  $7 \times 10^{-12} \text{m/s}$  to  $2 \times 10^{-13} \text{m/s}$  in the area ranges from 0.5m to 6m to the gallery wall. In Figure V .4(b), the maximum horizontal hydraulic conductivity of clay rocks is about  $1.7 \times 10^{-9} \text{m/s}$ . In the area ranges form 0.5m to 6m to the gallery wall, the horizontal hydraulic conductivity varies from  $1 \times 10^{-11} \text{m/s}$  to  $1 \times 10^{-12} \text{m/s}$ . It can be seen that the hydraulic conductivity

is larger in the horizontal direction than in the vertical direction. This is mainly due to the development of fractures.

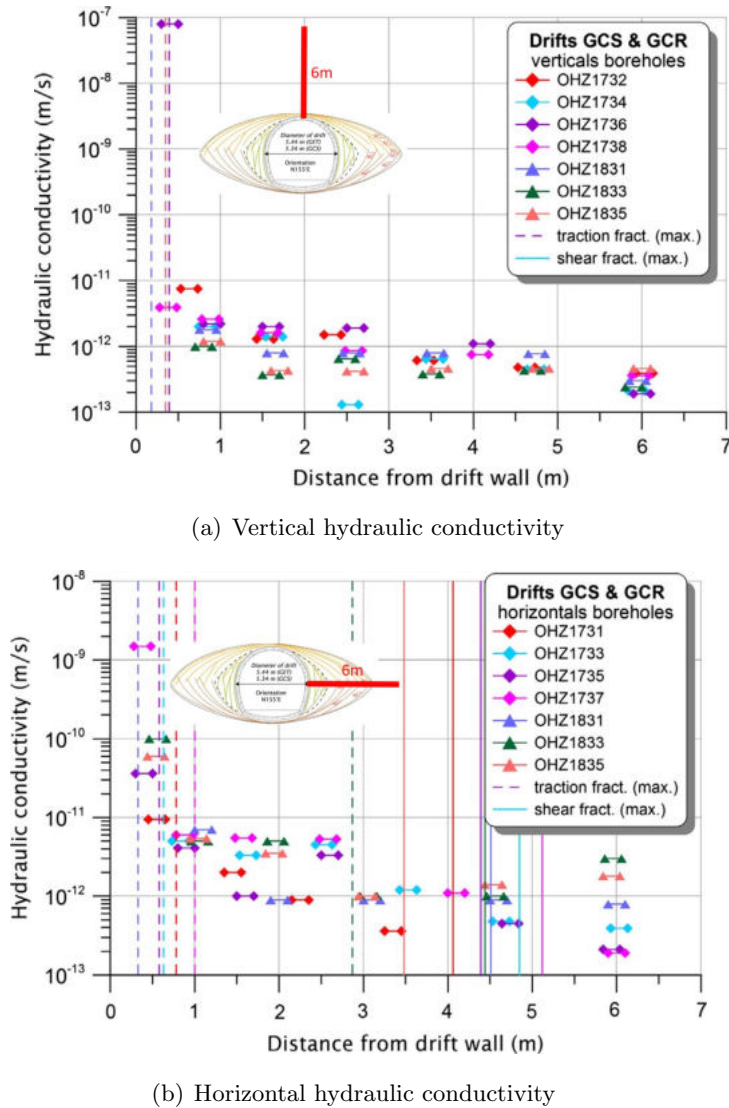


**Figure V .4:** Hydraulic conductivity in GCS gallery [Armand et al., 2014]

Since the implementation of the ANDRA project, a number of constitutive models have been used to study the deformation and stress distribution of the clayey rocks around the gallery during excavation [Bian et al., 2017, Cuvilliez et al., 2017, Mánica et al., 2017, Pardoen and Collin, 2017, Souley et al., 2017, Van den Eijnden et al., 2017, Yao et al., 2017]. These simulation models have many advantages to be learned. However, most of the research models are based on isotropic materials. And some research models only consider deformation and damage under purely mechanical conditions.

Therefore, this chapter aims to simulate the deformation and pore pressure changes in the rocks around the gallery caused by the gallery excavation using the anisotropic multi-scale model that considers the effects of anisotropy and hydro-mechanical coupling proposed in previous chapters, with the hope of obtaining good simulation results.

### 3 Presentation of excavation model

#### 3.1 Identification of elastic, plastic and viscoplastic parameters

For this chapter, the elastic parameters (mainly representing Young's modulus and Poisson ratio) of the clayey rocks (i.e., undisturbed COx argillite) around the excavated gallery at a depth of 490m are derived from the extensive literature [Andra, 2005a, Charlier et al., 2013], as shown in Table V .1. The elastic parameters of the solid clay phase are calculated by the Equation II .9 in a reverse way. And the calculated macroscopic elastic parameters are also presented in Table V .1. Other unchanged parameters are shown in Table IV .1.

<i>Physical parameters</i>	$f = 0.173$				
<i>Elastic</i>	$E_1^{hom}(MPa)$	$E_3^{hom}(MPa)$	$\nu_{12}^{hom}$	$\nu_{31}^{hom}$	$G_{13}^{hom}(MPa)$
Measured macroscopic value	5000	4000	0.30	0.24	1920
Solid clay phase	3158.78	2506.51	0.35	0.28	1003.6
Calculated macroscopic value	5002.84	4028.21	0.30	0.23	1728

**Table V .1:** List of elastic parameters for transversely isotropic COx claystone in the undisturbed state

In the same way as the plasticity parameters were determined in Chapter IV , the plasticity parameters for the excavation model in this chapter can also be obtained by fitting the results of macroscopic laboratory tests. All of the experimental data comes from the Armand et al. [2017b]. Due to the deconfinement and sample preparation, the specimens in the Armand et al. [2017b] experiment become unsaturated, corresponding to a relative humidity of 90%. It is worth noting that for the plasticity parameters, only the frictional coefficient  $\hat{T}_m$  and  $\hat{t}_m$  need to be updated. The other plastic parameters are the same as in Chapter IV .

In order to determine the values of  $\hat{T}_m$  and  $\hat{t}_m$ , two triaxial compression tests at confining pressure of 6MPa and 12MPa are used. The rest of the model parameters are taken from Tables V .1 and IV .3. And the simulation results are shown as follows:

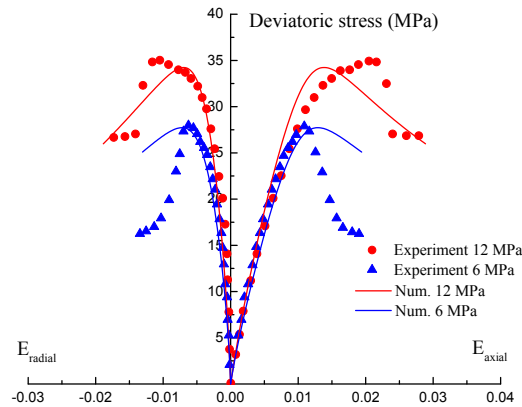


**Figure V .5:** Triaxial compression tests with different confining pressure under the  $H_r = 90\%$

It's worth noting that the axial axis is perpendicular to the bedding plane ( $\theta = 90^\circ$ ). A good performance is obtained between the simulation results and the experimental data, as shown in Figure V .5. Therefore, the parameters  $\hat{T}_m = \hat{t}_m = 0.527$  for the excavation model are determined.

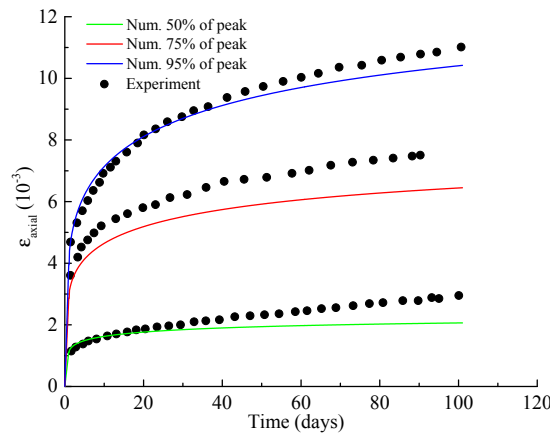


**Figure V .6:** Creep tests at stress levels of 50%, 75% and 90% of peak strength under the  $H_r = 90\%$

In addition, for excavation construction, the time-dependent deformation of the rocks near the gallery must be taken into account to predict the stability of the gallery wall. In order to determine the model parameters of the viscoplastic strain (i.e.,  $\eta_1$ ,  $b_{vp}$ , and  $m$ ), three simulations will be performed in this section using experimental data from Armand

et al. [2017b]. And the elastic and plastic parameters are taken from Tables V .1 and IV .3 (here  $\hat{T}_m = \hat{t}_m = 0.527$ ).

Figure V .6 shows the simulation results of the creep test. The creep stresses are equal to 50%, 75%, and 90% of the peak strength. The load direction is parallel to the bedding plane, which is the same as the situation in Figure V .5. The simulation results perform relatively well, thus, the viscoplastic parameters can be determined as  $\eta_1 = 10^{15} Pa \cdot s$ ,  $b_{vp} = 60$ ,  $m = 2$ . And the values of these parameters are also shown in Table IV .3.

On the other hand, it is often necessary to consider the hydraulic properties of the rocks around the excavation gallery when carrying out excavation simulations. To this end, the permeability and Biot's coefficient are important parameters that should be taken into account. According to Figure V .4, except for the hydraulic conductivity near the gallery wall, the hydraulic conductivity is  $1 \times 10^{-11} m/s$  to  $1 \times 10^{-12} m/s$  in the horizontal direction and  $7 \times 10^{-12} m/s$  to  $2 \times 10^{-13} m/s$  in the vertical direction. In addition, by referring to the existing literature [Andra, 2005a, Charlier et al., 2013], hydraulic parameters can be obtained for clayey rocks at a depth of 490m. These parameters are shown in Table V .2.

Permeability ( $m^2$ )	$k_1 = 4 \times 10^{-20}$ , $k_3 = 1.33 \times 10^{-20}$
Biot's coefficient	$B_1 = 0.6$ , $B_3 = 0.67$

**Table V .2:** Typical values of permeability and Biot's coefficient

## 3.2 Boundary conditions

### 3.2.1 Model size and mesh distribution

As the geo-material near the gallery is transversely isotropic, a quarter of the gallery section is selected. Under the assumption of small disturbances, the presented excavation model is assumed to be a plane-strain model. The radius of the gallery is 2.6m. For the mesh of this model, a higher density is used in a ring of 7.8m width contiguous with the gallery wall in order to more accurately simulate the deformation of the rocks around the gallery wall, as shown in Figure V .7.

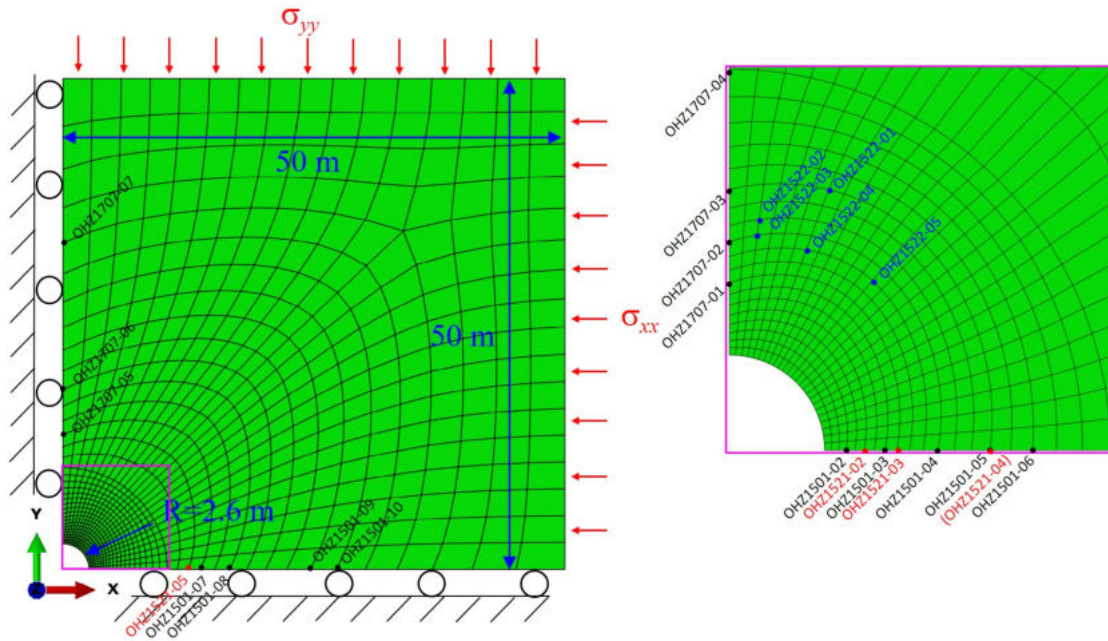


Figure V .7: Mesh and boundary conditions

OHZ1501 borehole (horizontal displacement)			OHZ1707 borehole (vertical displacement)			OHZ1521,1522 boreholes (pore pressure)		
Name	X(m)	Y(m)	Name	X(m)	Y(m)	Name	X(m)	Y(m)
1501-02	3.21	0	1707-01	0	4.84	1521-02	3.7	0
1501-03	4.21	0	1707-02	0	6.34	1521-03	4.5	0
1501-04	5.71	0	1707-03	0	7.84	1521-04	7.2	0
1501-05	7.21	0	1707-04	0	10.84	1521-05	12.5	0
1501-06	8.21	0	1707-05	0	13.84	1522-01	2.8	7.4
1501-07	13.21	0	1707-06	0	17.84	1522-02	0.8	6.9
1501-08	17.21	0	1707-07	0	32.47	1522-03	-0.6	6.5
1501-09	21.21	0				1522-04	-2.1	6.0
1501-10	27.21	0				1522-05	-4.1	5.5

Table V .3: Coordinates of the measurement points in the surrounding rock

As can be seen from the introduction of gallery in the previous section, many different types of test instruments were fixed in advance around the tested gallery to measure the deformation of the rocks around the gallery and the changes in pore pressure caused by

excavation. And the coordinates of each measurement point in the coordinate system (as shown in Figure V .7) are given in Table V .3.

### 3.2.2 Stress distributions

For this excavation model, the most important thing is to determine the stress distribution of the gallery wall. For anisotropic material, the analysis of the stress distribution on the gallery wall is relatively complex. In addition, the stress path of the element located on the gallery wall is not as simple as that of the ordinary element. In fact, as the excavation progresses, the radial stress in the element located on the gallery wall decrease. At the same time, the hoop stress increases to keep the mean stress constant. It can be seen from Figure V .8 that in the unsupported case, the vertical component stress at point *A* decreases to zero after excavation, while the horizontal component stress increases. And the situation at the point *B* is opposition, where the component stress along the horizontal direction decreases to zero and the component stress along with the vertical direction increases. The stress at the point *C* varies with the  $\theta$ .

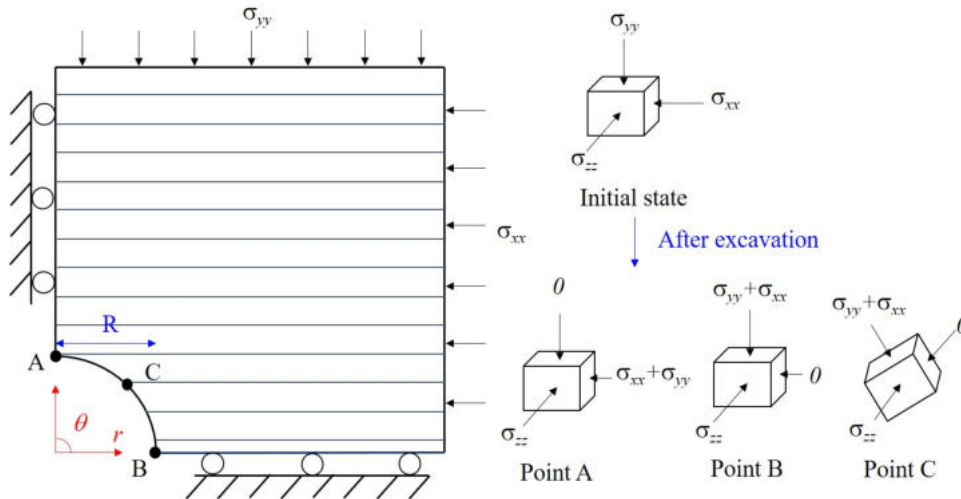


**Figure V .8:** The loading paths at three different points in the excavation process [Bian et al., 2017]

In this chapter, a local coordinate is established with the center (i.e.,  $(X, Y) = (0, 0)$ ) of the gallery as the coordinate origin, as shown in Figure V .8. The horizontal axis is the  $r$ -axis, and the vertical direction represents  $\theta = 90^\circ$ , as shown in Figure V .8. The load

on the gallery wall in this chapter can be expressed as follows:

$$\begin{aligned}\sigma_r &= \sigma_{xx}(\cos\theta)^2 + \sigma_{yy}(\sin\theta)^2 \\ \sigma_\theta &= (\sigma_{yy} - \sigma_{xx})\cos\theta\sin\theta\end{aligned}\tag{V .1}$$

For the anisotropy of the clayey rocks near the gallery, several factors should be considered in the anisotropic multi-scale model described above. The first factor is  $\theta$  (as shown in Figure IV .1), which defines the angle between the structural coordinates and the direction of the load. Since the excavation direction is along the major stress  $\sigma_H$  (or minor stress  $\sigma_h$ ), the load direction is consistent with the structural coordinates. Therefore, the angle  $\theta$  can be ignored. The second factor involves the anisotropic properties of the plastic deformation caused by excavation, which in this case mainly refers to the frictional coefficients  $T_m(\eta)$  and  $t_m(\eta)$ . The scalar parameter  $\eta$  (in Equation III .19) is different for each Gaussian integration point of the excavation model. Therefore, the loading orientation vector  $\boldsymbol{l}$  must be calculated using the Equation III .16 instead of the Equation IV .2.

In this excavation simulation works, the entire excavation process is carried out over 28 days. And the excavation front through the study section is at 14th day. The type of support at the gallery wall is flexible support. The radial support stress at the gallery wall is constant at 0.3MPa after the 25th day of excavation. In addition, the initial pore pressure is equal to 4.7MPa. Here, the gravity-induced gradient is neglected in this section. The pore pressure decreases sharply from 4.7MPa to zero between the 13th day and 15th day with a linear curve to consider the excavation front through the study section. The external boundaries of the model are in the drained state (i.e., the pore pressure is constant and equal to 4.7MPa) in this section.

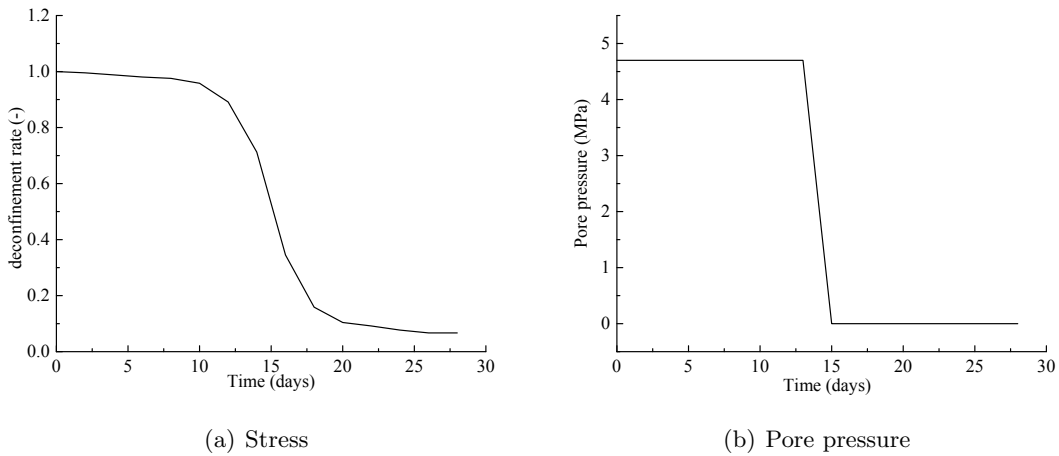


**Figure V .9:** Deconfinement curve

The excavation is modeled by reducing the stresses applied on the gallery wall and pore pressure with a deconfinement curve [Seyedi et al., 2017] (as shown in Figure V .9). In addition, the total stress at the boundary in the normal direction is constant. These details are consistent with the actual project [Souley et al., 2017]. In this section, the stress distribution of the excavation model includes two cases: galleries GCS and GED.

#### ★ Gallery *GCS*

The gallery GCS is excavated along the major stress  $\sigma_H$ , with horizontal and vertical stresses equal to  $\sigma_{xx} = \sigma_h = 12.4MPa$  and  $\sigma_{yy} = \sigma_v = 12.7MPa$ , respectively. The direction of the gallery axis is parallel to the  $Z$ -axis. The stress on the gallery axis is equal to  $16.12MPa$ . For simplicity, the gravity-induced body forces are ignored.

#### ★ Gallery *GED*

The GED gallery is excavated along the minor stress axis  $\sigma_h$ , which differs from the GCS gallery. The horizontal and vertical stresses are  $\sigma_{xx} = \sigma_H = 16.12MPa$  and  $\sigma_{yy} = \sigma_v = 12.7MPa$ , respectively. The stress along the GED gallery axis (i.e.,  $Z$ -axis) is  $12.4MPa$ .

### 3.3 Verification of numerical accuracy

The purpose of this part is to verify the correctness of the stress distribution on the excavation model presented above. For simplicity, it is assumed that these transversely isotropic clayey rocks are isotropic with Young's modulus  $E = 5000MPa$  and Poisson's ratio  $\nu = 0.33$ . The external stress along the  $X$ -axis is  $\sigma_{xx} = 12.4MPa$  and along the  $Y$ -axis is  $\sigma_{yy} = 12.7MPa$ . The stress on the gallery wall is calculated by the Equation V .1, which decreases with the deconfinement curve (as shown in Figure V .9(a)).

Therefore, the stress distributed on the gallery wall can be calculated using the theoretical Equation V .2, as shown below:

$$\begin{aligned}\sigma_r &= \frac{\sigma_{xx} + \sigma_{yy}}{2} \left(1 - \frac{R^2}{r^2}\right) + \frac{\sigma_{xx} - \sigma_{yy}}{2} \cos(2\theta) \left(1 - \frac{R^2}{r^2}\right) \left(1 - 3\frac{R^2}{r^2}\right) \\ \sigma_\theta &= \frac{\sigma_{xx} + \sigma_{yy}}{2} \left(1 + \frac{R^2}{r^2}\right) - \frac{\sigma_{xx} - \sigma_{yy}}{2} \cos(2\theta) \left(1 + 3\frac{R^2}{r^2}\right)\end{aligned}\tag{V .2}$$

where  $r$  represents the distance from the measurement point to the coordinate origin. Figures V .10(a) and V .10(b) show the comparison of simulation and theoretical stress values of measurement points along the horizontal and vertical directions. The stress distributions for the excavation model used in this part follows the stress distribution method described in the previous section.

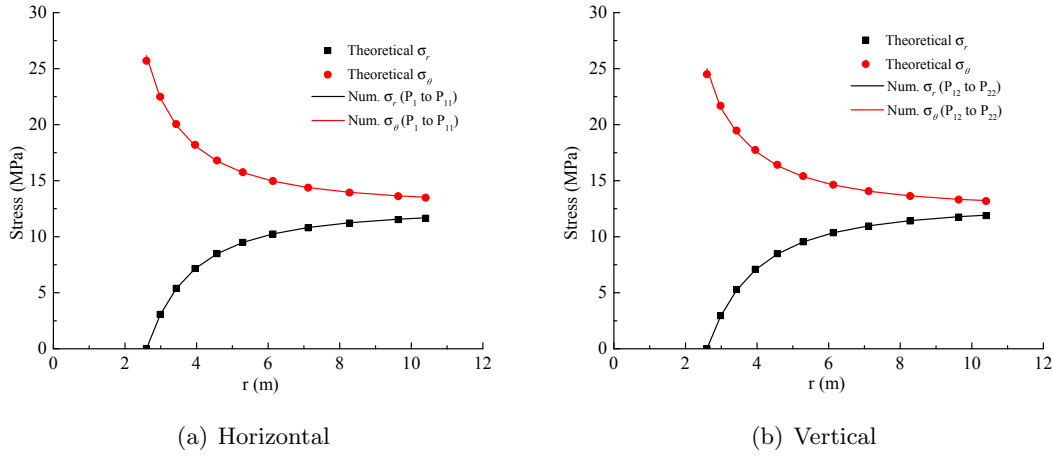


**Figure V .10:** Comparison of simulation and theoretical stress values along the horizontal and vertical directions

## 4 Numerical modeling of excavation deformation zones

The purpose of this section is to present the simulation results of the gallery excavation. The model for this excavation simulation takes into account the multi-scale and anisotropic properties of clayey rocks, which has been presented in Chapters II and III . For the gallery excavation simulations, two different excavation cases will be considered in this section:

★ Case 1: Excavation simulations under purely mechanical conditions;

★ Case 2: Excavation simulations under hydro-mechanical coupling conditions.

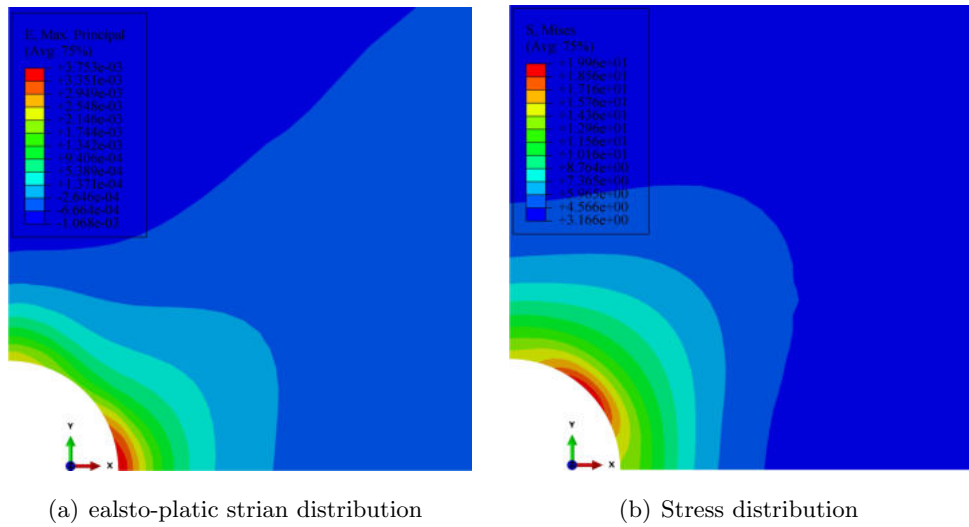
### 4.1 Excavation simulations under purely mechanical conditions

In this section, the excavation simulation takes into account elastic-plastic deformation, viscoplastic deformation, and the damage of clayey rocks surrounding the gallery wall induced by excavation. In this section deals with the excavation simulation under purely mechanical conditions, taking two main objectives into account. The first objective is to analyze the excavation under purely mechanical conditions. Another, the simulation results can be compared with the results of excavation simulations under hydro-mechanical coupling conditions, which can be used to analyze the effect of pore pressure on the deformation of clayey rocks.

The excavation model used in this section has been described in the previous section, which can be shown in Figure V .7. The model's parameters are shown in Tables V .1 and IV .3 (here  $\hat{T}_m = \hat{t}_m = 0.527$ ).

### Gallery *GCS*

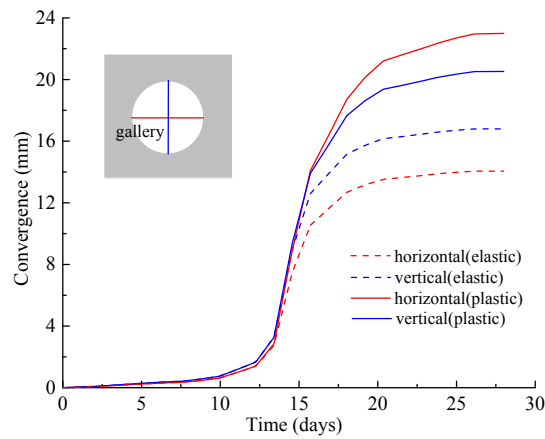
Figure V .11 illustrates the elasto-plastic strain and stress distribution. It can be seen that the strain along the horizontal direction is greater than the strain along the vertical direction. In addition, the strain and stress distribution in Figure V .11 are quantified by selecting the simulation results for several nodes, whose coordinates correspond to the coordinates of the measurement points in Table V .3. In fact, since the mesh is not infinitely small, the coordinates of the selected nodes will not be exactly equal to the coordinates of measured points in Table V .3. In this section, the linear interpolation method will be used to obtain relatively accurate simulation results of the measurement points (mainly for comparison with the simulation results in the following section).



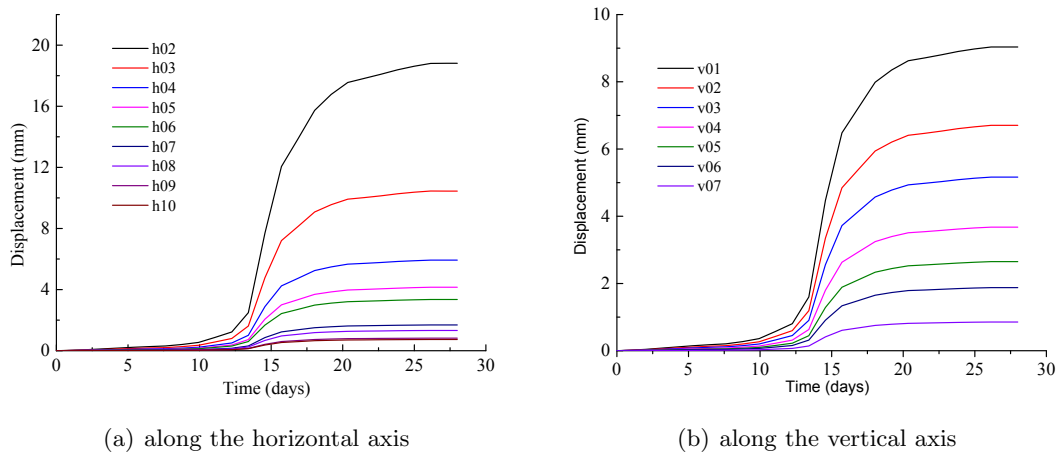
**Figure V .11:** Elasto-plastic strain and stress distribution at the end of excavation for transversely isotropic clayey rocks (GCS)

Figure V .12 shows the vertical and horizontal convergences of the gallery wall during excavation, indicated by the red and blue lines, respectively. The solid line in this figure shows the convergences considering elastic-plastic strain and damage-induced strain. The dashed line indicates the convergences of the elastic strain part only. The convergence of the purely elastic part clearly shows that the convergence in the vertical direction is greater than the convergence in the horizontal direction. This is mainly due to the fact that the

stiffness of clayey rocks at a depth of 490m in the vertical direction is smaller than that in the horizontal direction. The opposite phenomenon occurs for plastic convergences. As shown in Figure V .12, the plastic strain (i.e., convergences) in the horizontal direction is significantly greater than the plastic strain in the vertical direction. This plastic strain also includes the strain induced by damage during excavation, which coincides with the actual situation.



**Figure V .12:** Convergence evolutions of GCS



**Figure V .13:** Displacement evolutions of selected points (GCS)

Figure V .13 shows the change in displacement of the selected points during the simulated excavation. It can be seen that the further away the measurement point is from the gallery wall, the smaller the displacement occurs. It is consistent with the actual situation.

Gallery *GED*

Figure V .14 shows the distribution of elasto-plastic strain and stress zones. It can be seen that the strain along the vertical direction is larger than the strain along the horizontal direction. Figure V .15 shows the convergences of the gallery along with the horizontal and vertical directions (represented by solid lines). As shown in Figure V .15, the dashed lines represent the convergences of the purely elastic part. The convergence of pure elasticity in the horizontal direction is larger than that in the vertical direction. This is mainly because the  $\sigma_H$  is greater than the  $\sigma_v$ . The convergence value, considering the effect of plasticity and damage, in the vertical direction is larger than that in the horizontal direction, which is consistent with the actual situation. Figure V .16 shows the simulation results about the displacement of the measured points.

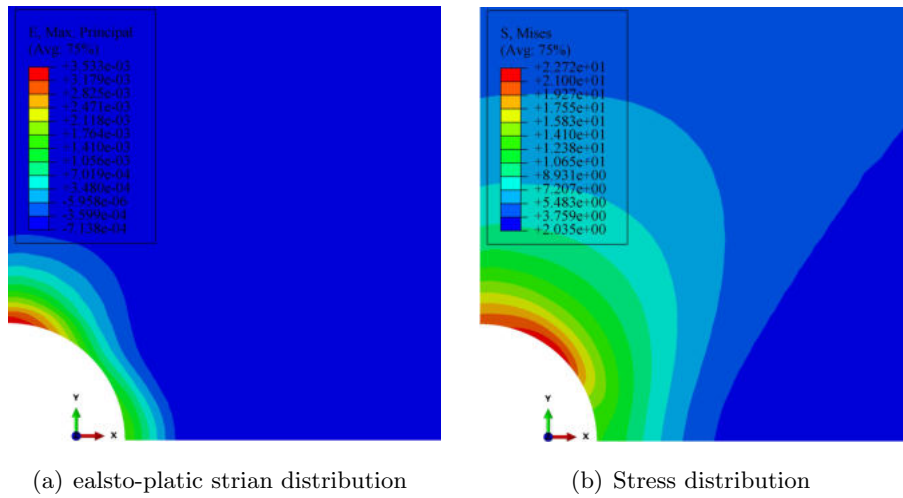


**Figure V .14:** Elasto-plastic strain and stress distribution at the end of excavation for transversely isotropic clayey rocks (GED)

The simulation results show that the multi-scale anisotropic model proposed above is suitable for simulating the excavation-induced deformation of clayey rocks near the gallery. As the clayey rocks in the actual environment are saturated at a depth of 490m, the excavation simulations under hydro-mechanical coupling conditions will be considered in the next section.

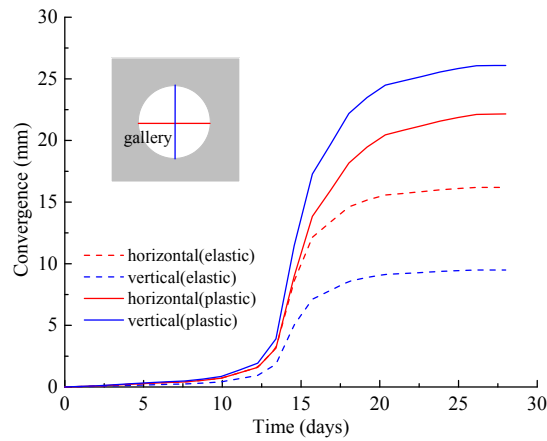
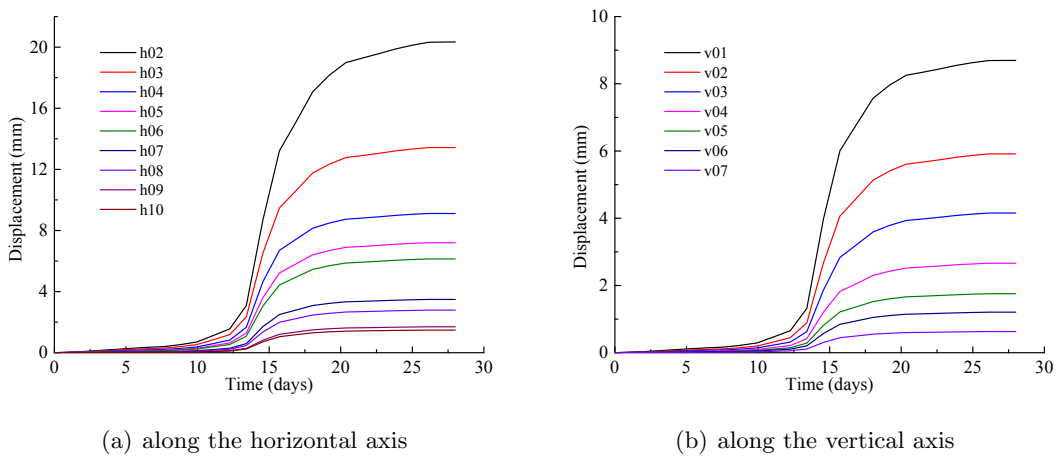


Figure V .15: Convergence evolutions of GED



(a) along the horizontal axis

(b) along the vertical axis

Figure V .16: Displacement evolutions of selected points (GED)

## 4.2 Excavation simulations under hydro-mechanical coupling conditions

Similar to the previous section, this section also considers two cases of excavation along with the major and minor stresses directions (i.e., galleries GCS and GED). In addition, the effect of hydro-mechanical coupling are also considered in this section. The boundary conditions for these two cases have been described in the previous section. For the GCS gallery, extensive *in situ* experiments were carried out on the displacement and pore pressure of the clayey rocks around the excavated gallery. However, relatively few *in situ* experiments conducted on the clayey rocks around the GED gallery. Therefore, in this section, the numerical simulations of the displacement and pore pressure in the clayey

rocks surrounding the GCS gallery will be compared with the *in situ* experiments. Numerical simulations of the clayey rocks surrounding the GED gallery will then be presented without comparison with the *in situ* experimental results.

### Gallery *GCS*

The excavation simulation results of the GCS gallery considering hydro-mechanical coupling condition show that the deformation of the clayey rocks around the gallery caused by the excavation is greater in the horizontal direction than in the vertical direction. It is consistent with the actual engineering situation (as shown in V .1). The displacement distribution and pore pressure distribution of the clayey rocks around the gallery at different time periods can be found in Figures VII .1 and VII .2 in Appendix B. Before the 14th day of excavation, the pore pressure near the gallery wall remains constant as it's not affected by excavation. And the displacement around the gallery is not changed significantly as a result of the excavation. When the excavation time exceeds 14 days, there is a decrease in pore pressure around the gallery, as shown in Figure V .9(b). When the excavation date is more than 28 days, the gallery excavation is considered completed and the stresses on the gallery wall remain at a small value. The deformation of the rocks around the gallery is mainly caused by the change of pore pressure and viscoplastic deformation.

It is worth noticing that the pore pressure decreases significantly in the horizontal direction near the gallery wall after 28th days. Besides, it can be observed that the pore pressure of the clayey rocks near the gallery wall has an increase zone in the vertical direction (i.e., red area). There are two main factors responsible for this phenomenon. The first is that the permeability of the clayey rocks is not completely symmetrical in the horizontal and vertical directions. For the GCS gallery, the permeability in the vertical direction is equal to  $1.3 \times 10^{-20} m^2$ , and the permeability in the horizontal direction is equal to  $4 \times 10^{-20} m^2$ , as shown in Table V .2. The second factor is that the stiffness tensor in horizontal and vertical directions are different, which leads to different elastic-plastic deformations in the horizontal and vertical directions. The skeletal deformation of the clay solid phase is directly related to the internal pore pressure.

Figure V .17 shows the convergences between the numerical simulation results and the *in situ* experiments. The numerical simulation results take into account the hydro-mechanical coupling conditions. From this figure, one can notice that the difference between the horizontal and vertical deformation is relatively small in the pre-excavation period (i.e., 28 days). As the creep time increases, the difference in deformation gradually increases. *In situ* experiments shown that horizontal convergence caused by gallery excava-

tion is greater than the vertical convergence. The simulation results using the multi-scale anisotropy model are consistent with the *in situ* experiments.

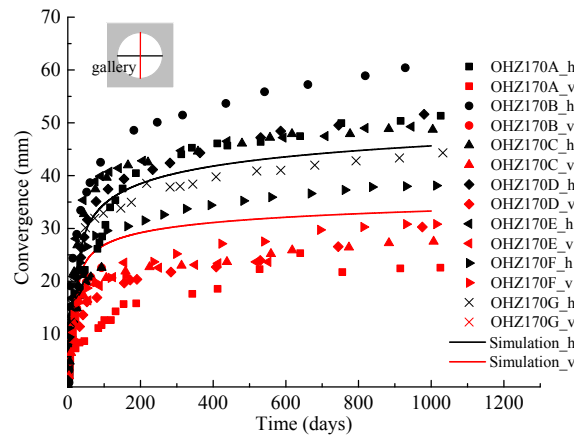


Figure V .17: Variation in horizontal and vertical convergences for GCS gallery

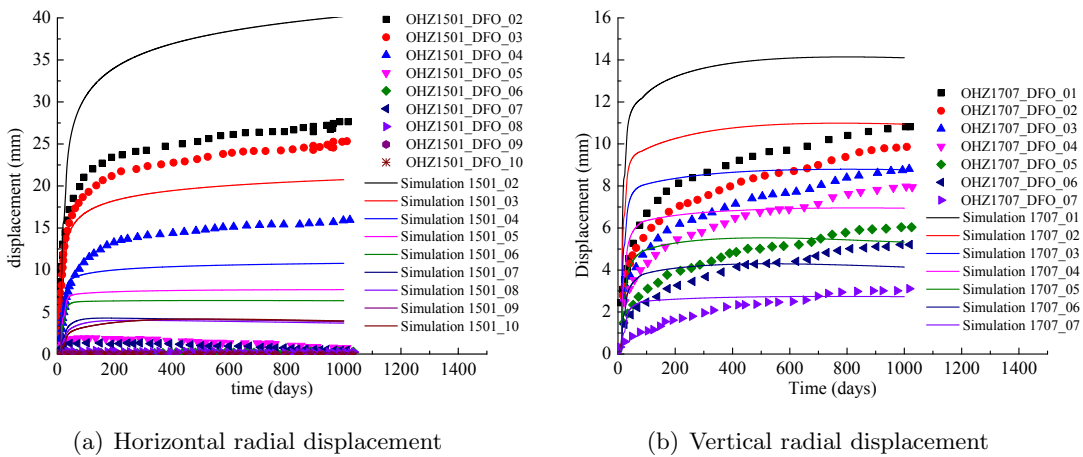
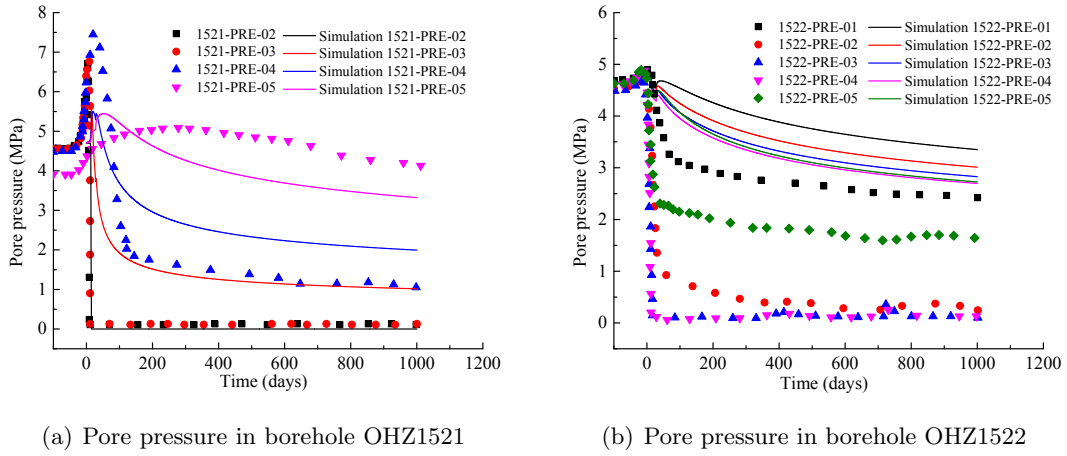


Figure V .18: Variation in horizontal and vertical radial displacements of GCS gallery

Figure V .18 shows the experiments and numerical simulation results in the horizontal and vertical directions. In particular, the measurement data are taken from measurement points in horizontal and vertical boreholes OHZ1501 and OHZ1707 (as shown in Figure V .3). The experimental data on deformation at the measurement points during the excavation are monitored and recorded by high-precision measuring equipment. The coordinates of the measurement points are presented in Table V .3.



**Figure V .19:** Variation in pore pressure in horizontal and inclined boreholes

Figure V .19 shows the *in situ* experimental and numerical simulation data for pore pressure. The coordinates of the measurement points located in the horizontal and inclined boreholes are shown in Table V .3. In Table V .3, we can find some measurement points with negative X-coordinates. This is mainly due to the special location of the inclined borehole OHZ1522, as shown in Figure V .3. Since this simulation work uses a quarter-symmetric model (as shown in Figure V .7), the X-coordinate here can be directly used as a positive value.

### Gallery *GED*

*In situ* experiments show that gallery excavation along the minor stress  $\sigma_h$ , such as the GED gallery, the displacement in the vertical direction around the GED gallery is greater than that in the horizontal direction. The displacement distribution and pore pressure distribution of clayey rocks around the gallery at different time periods are shown in Figures VII .3 and VII .4 in Appendix B. In this section, the effect of pore pressure inside the clay matrix on the deformation of the structure during the excavation is considered. The permeability and Biot's coefficient have been determined in previous section and are shown in Table V .2. The simulation time is considered to be 1000 days. When the excavation is completed (i.e., 28 days), the stresses on the gallery wall remain unchanged. As the creep time increases, the viscoplastic deformation gradually increases. The pore pressure inside the clay matrix also varies with creep time, and the pressure of the gas mixture  $p_g$  in the gallery is equal to standard atmospheric pressure.

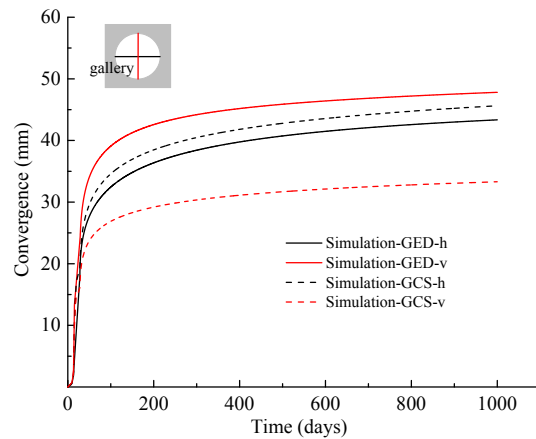
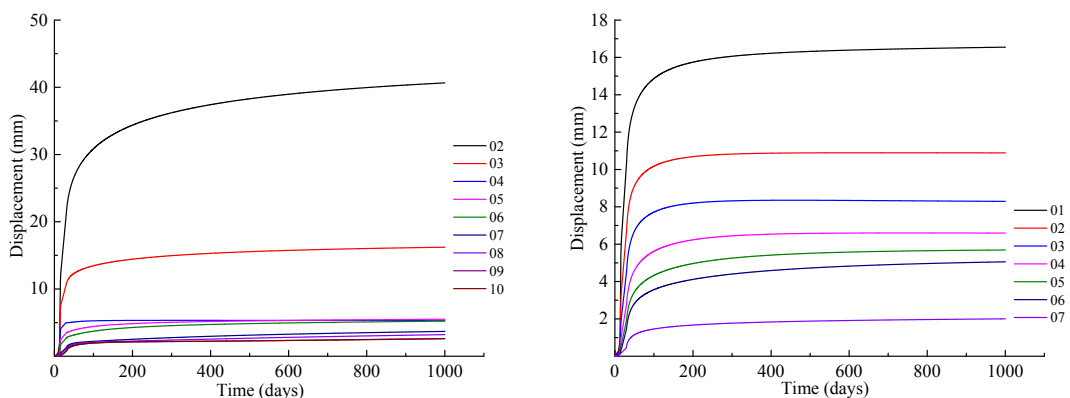


**Figure V .20:** Horizontal and vertical convergences for two excavation types, GCS and GED gallery

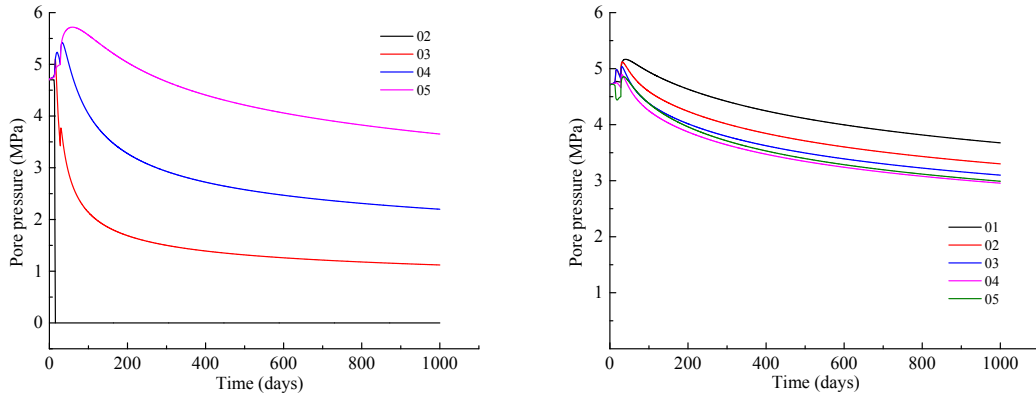
Figure V .20 shows the comparison of horizontal and vertical convergences of the two excavation types, i.e., galleries GCS and GED. The solid line in this figure represents the convergence of the GED gallery, and the dashed line represents the convergence of the GCS gallery. It can be observed that excavation along with the minor stress  $\sigma_h$  causes larger convergence than excavation along with the major stress  $\sigma_H$ . The excessive vertical deformation around the gallery means that more measures are needed to support the GED gallery.



(a) Horizontal radial displacement

(b) Vertical radial displacement

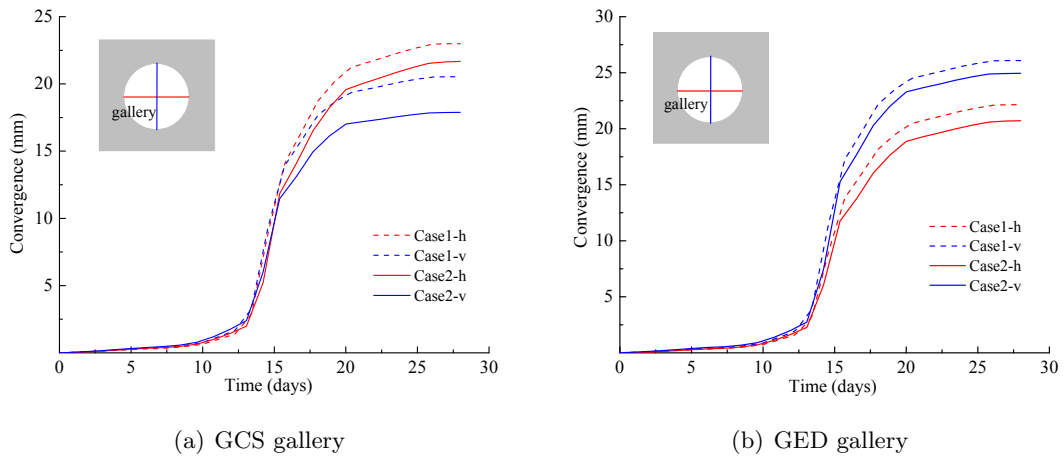
**Figure V .21:** Variation in horizontal and vertical radial displacements for GED gallery



(a) Pore pressure in the horizontal borehole O-HZ1521 (b) Pore pressure in the inclined borehole O-HZ1522

**Figure V .22:** Variation in pore pressure in horizontal and inclined borehole for GED gallery

Figures V .21 and V .22 are the displacement curves and pore pressure variation curves of the measurement points near the GED gallery wall. The selected measurement points are the same as in the GCS gallery, and their coordinates are shown in Tables V .3.



(a) GCS gallery (b) GED gallery

**Figure V .23:** Comparison of convergence of the galleries considering H-M coupling condition (Case 2) and purely mechanical condition (Case 1)

Figure V .23 represents the comparative results about the convergence of the galleries considering hydro-mechanical coupling (i.e., Case 2) and purely mechanical conditions (i.e., Case 1). This figure shows the convergences of the gallery wall in horizontal and vertical directions during the excavation period (28days). As can be seen from this figure,

there is a slight decrease in convergence due to the presence of pore pressure. Due to the relatively low pore pressure compared to the mechanical forces at a depth of 490m and the relatively low permeability of the clayey rock, the pore pressure has little effect on convergence during the excavation process (time less than 28 days).

## 5 Conclusions

This chapter presented the excavation simulations considering both purely mechanical and hydro-mechanically coupled conditions. The simulations used the multi-scale anisotropy model presented in the previous chapters. The simulation results performed well compared to *in situ* experiments, which indicated that this anisotropic model can be used for stability prediction in actual excavation construction. In this chapter, the first section was about introducing the background of excavation and the main objective of this chapter. The second section was about the presentation of the excavation simulation model. The description of the boundary conditions in this section mainly included the description of stress distribution and mesh types and distribution. The determination of the model parameters was also described in this section. The last section was about the excavation simulations. And several conclusions were obtained as follows: 1. The deformation of clayey rocks around the gallery is greater in the horizontal direction than in the vertical direction when the excavation direction is along the major stress  $\sigma_H$ ; 2. The deformation of the clayey rocks around the gallery is larger in the vertical direction than in the horizontal direction when the excavation along the minor stress  $\sigma_h$ ; 3. The deformation of the surrounding rocks of the gallery caused by excavation along the minor stress is greater than that caused by excavation along with the major stress.



# Chapter VI

## Conclusions and perspectives

### 1 Conclusions

As an important potential rock, clayey rocks are often encountered in projects such as the geological disposal of radioactive waste, shale gas production, and acid gas sequestration. The deformation and damage of clayey rocks under complex geo-conditions, such as hydro-mechanical coupling, is an important research project that needs to be investigated. Besides, the clayey rocks at the underground depth of around 490m are considered to be transversely isotropic materials. To this end, a multi-scale model has been developed which takes into account the anisotropic and hydro-mechanical coupling properties of clayey rocks. This multi-scale model can be used to describe the elasto-plastic, viscoplastic, and induced damage in clayey rocks. The main conclusions of this thesis are presented as follows:

- An effective elastic anisotropic model was proposed to simulate the elastic properties of clayey rocks under multi-scale, multi-physical (i.e., Hydro-Mechanical) conditions. In order to establish the relationship between macroscopic, mesoscopic, and microscopic strains in this elastic model, a localization tensor  $\mathbb{A}$  was introduced. This localization tensor  $\mathbb{A}$  was calculated using the Mori-Tanaka scheme, which takes into account the interaction of mineral particles (mesoscale) or pores (microscale). The Hill's tensor and Green's function were also used in the calculation of the elastic model. On the other hand, in this elastic model, the effect of hydro-mechanical coupling on clayey rock mechanics was considered.
- Plastic deformation plays an important role in the mechanics of clayey rocks. Therefore, an anisotropic macroscopic elasto-plastic model was proposed in this section.

A two-step of the homogenization process was used to determine the macroscopic yield criterion. This yield criterion considered the transverse isotropic properties of clayey rocks. Hydraulic effects were also considered in this plastic yield function, which relies on the relationship between the pore pressure and the maximum frictional coefficient. Besides, time-dependent deformation was also considered in this multi-scale model.

- In this thesis, the damage of clayey rocks assumes directly related to the interface debonding between the mineral particles and porous clay matrix. When the initially perfectly bonded inclusions are debonded, they are assumed to be completely detached from the surrounding clayey matrix and behave as voids. The Weibull's probability distribution function was introduced to reflect the debonding degree.
- With the support of the ANDRA and many research results, several laboratory tests and GCS excavation tests have been investigated and used by our multi-scale model. The model's parameters were determined based on the laboratory tests and used in the excavation simulation work. The numerical prediction of the excavation simulation results was in good agreement with the *in situ* observations.

## 2 Perspectives

Although the multi-scale anisotropic model under hydro-mechanical coupling has been studied in the previous chapters and obtained good simulation results, there are still a lot of works that need to be investigated. In the future, some aspects of the improvement of the proposed model are described below:

- In future works, the proposed model can be coupled with a regularization method for dealing with the transition from diffuse damage and plastic deformation to localized cracking.
- The geological environment of clayey rocks is complex, and the effect of temperature on the mechanical behavior of clay-rich rocks is also an important issue to be investigated.

# Chapter VII

## Appendix

### A. Several tensor representations and operations used in this thesis

- The tensor representations (illustrated with  $a$  as an example):

$a$  scalar

$\underline{a}$  vector

$\mathbf{a}$  second-order tensor

$\mathbb{A}$  fourth-order tensor

- The tensor operations:

$\langle \cdot \rangle$  Average value

$\cdot$  Simple contraction

$:$  Double contraction

$\otimes$  tensor product  $(\mathbf{a} \otimes \mathbf{b})_{ijkl} = a_{ij}b_{kl}$

$\overline{\otimes}$  tensor product  $(\mathbf{a} \overline{\otimes} \mathbf{b})_{ijkl} = \frac{1}{2}(a_{ik}b_{jl} + a_{il}b_{jk})$

### B. Excavation simulation results

This section is about the excavation simulation results of displacement and pore pressure zones at different time period for GCS and GED gallery.

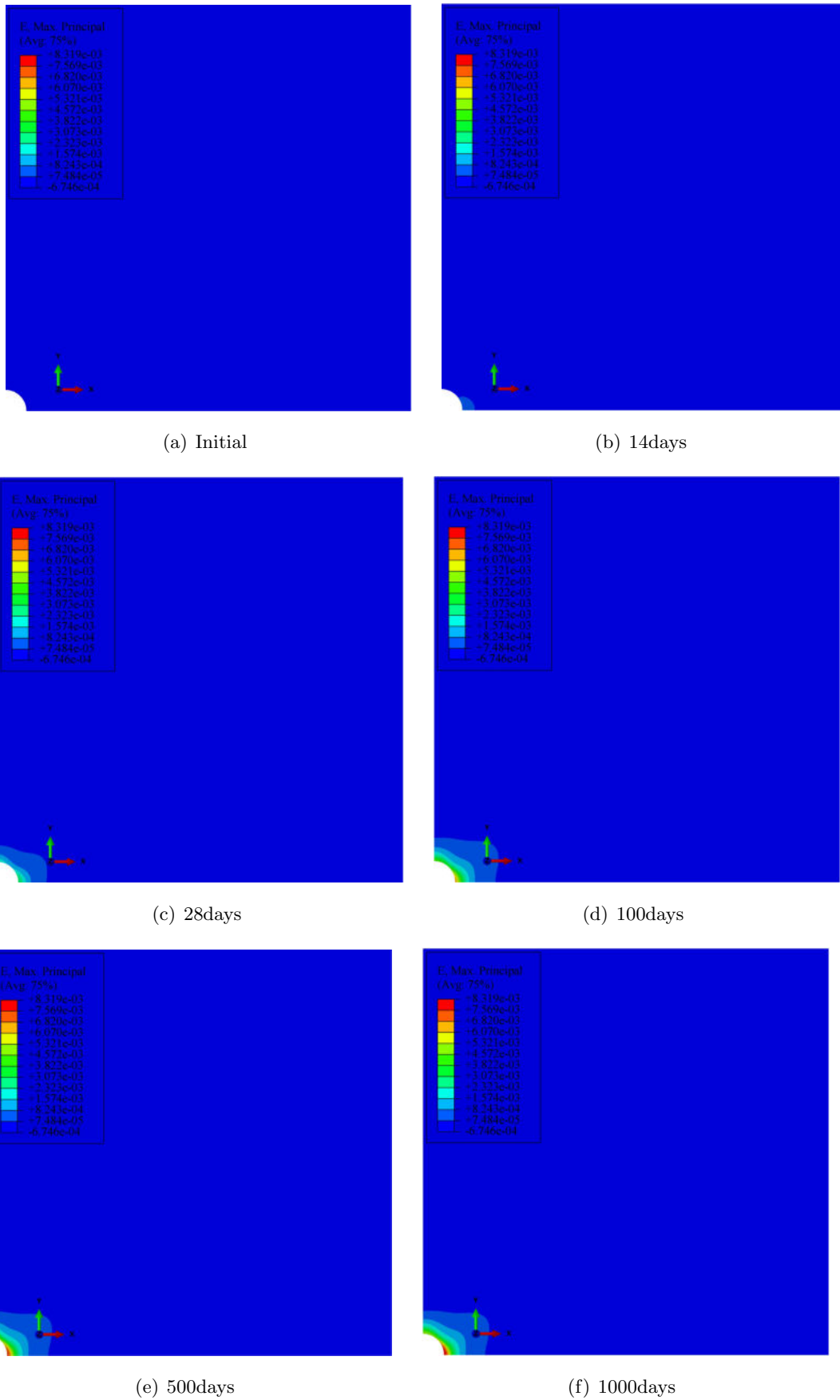
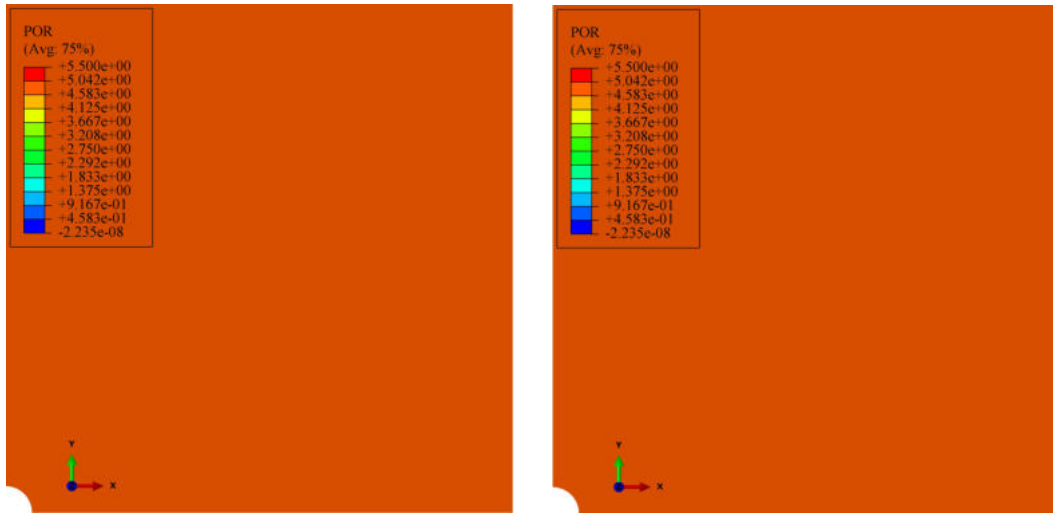
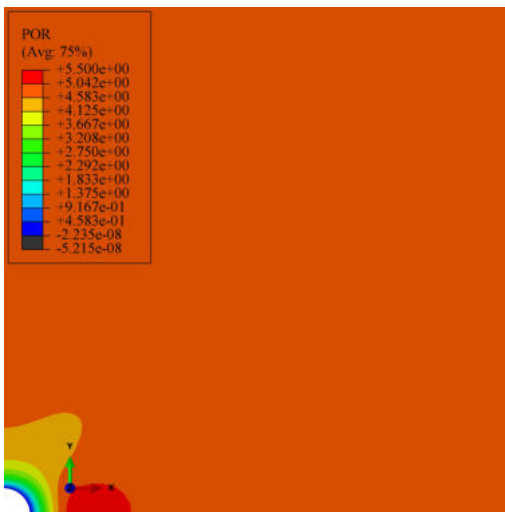


Figure VII .1: Displacement distribution at different excavation periods for GCS gallery

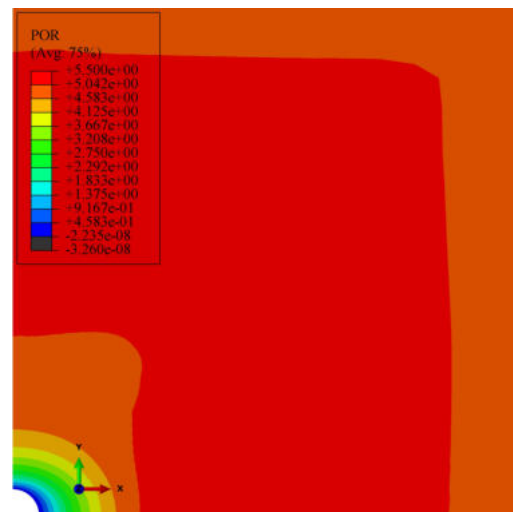


(a) Initial

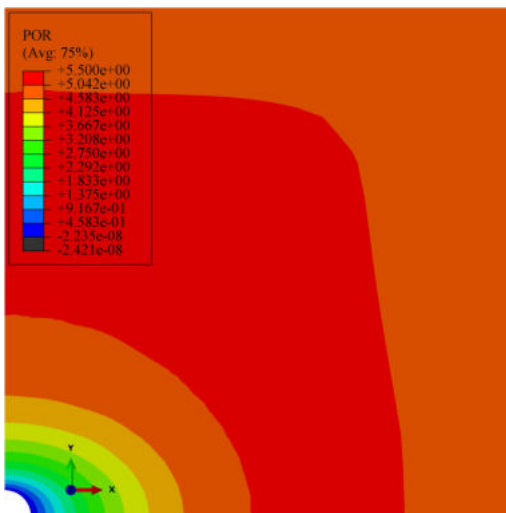
(b) 14days



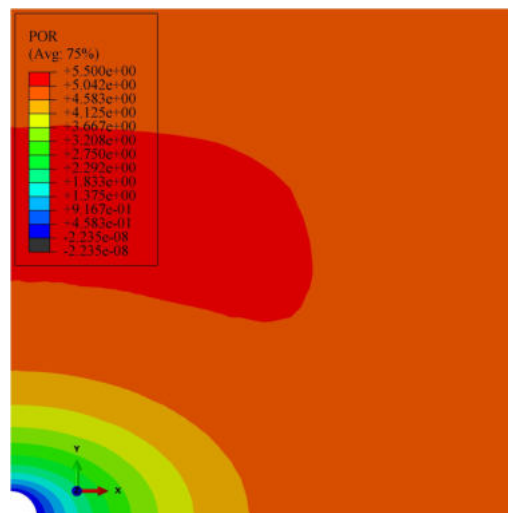
(c) 28days



(d) 100days

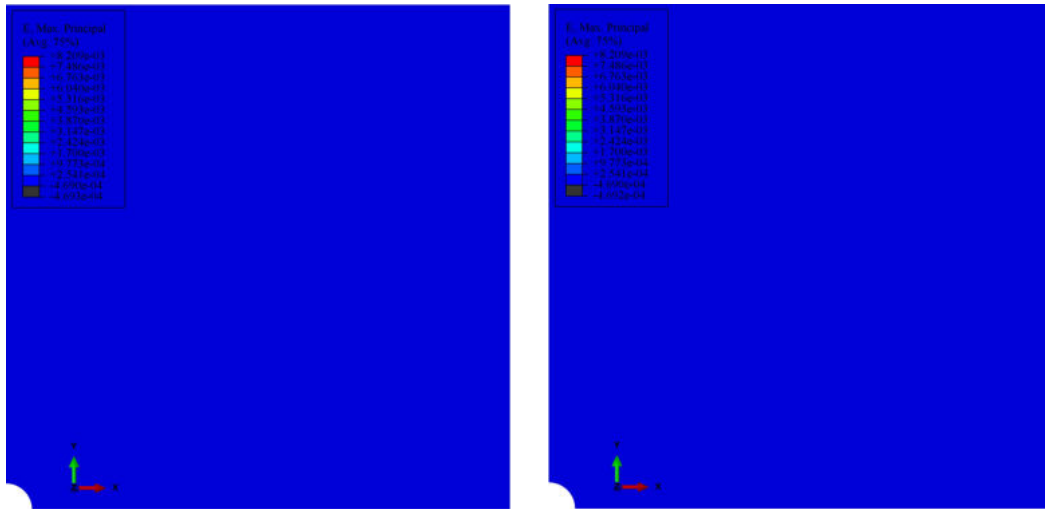


(e) 500days



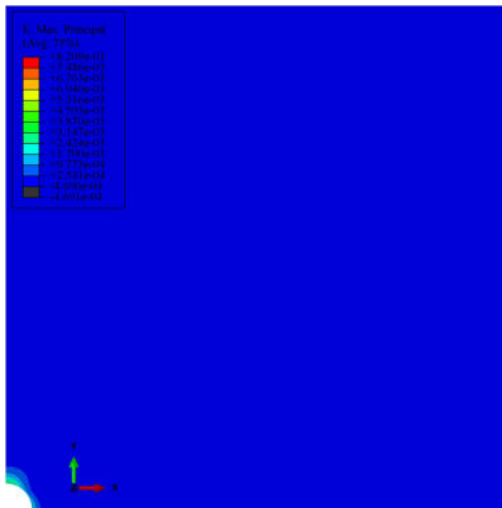
(f) 1000days

Figure VII .2: Pore pressure distribution at different excavation periods for GCS gallery

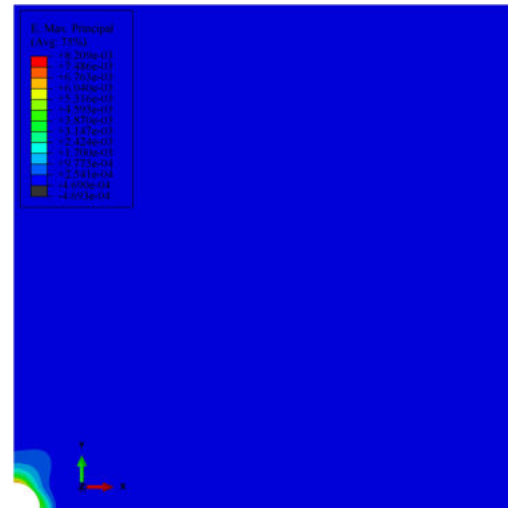


(a) Initial

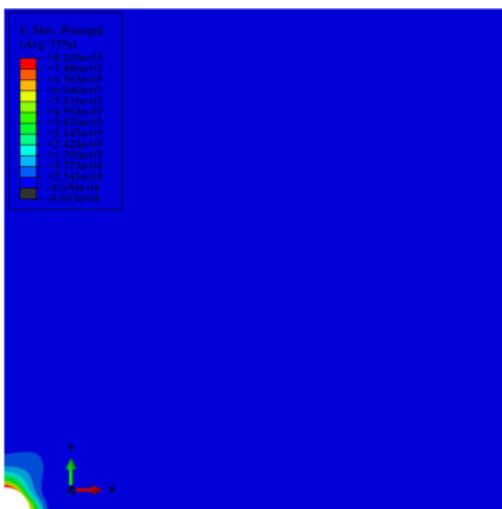
(b) 14days



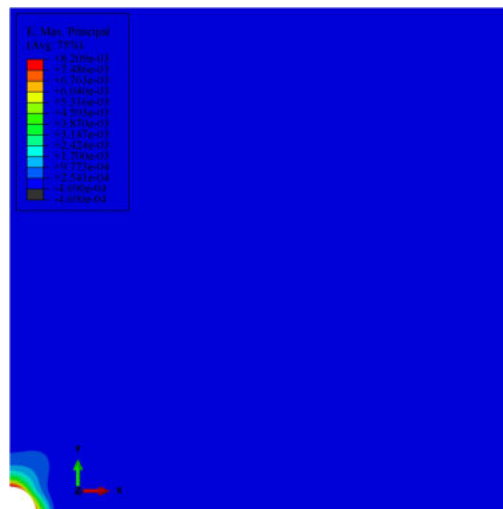
(c) 28days



(d) 100days



(e) 500days



(f) 1000days

**Figure VII .3:** Displacement distribution at different excavation periods for GED gallery

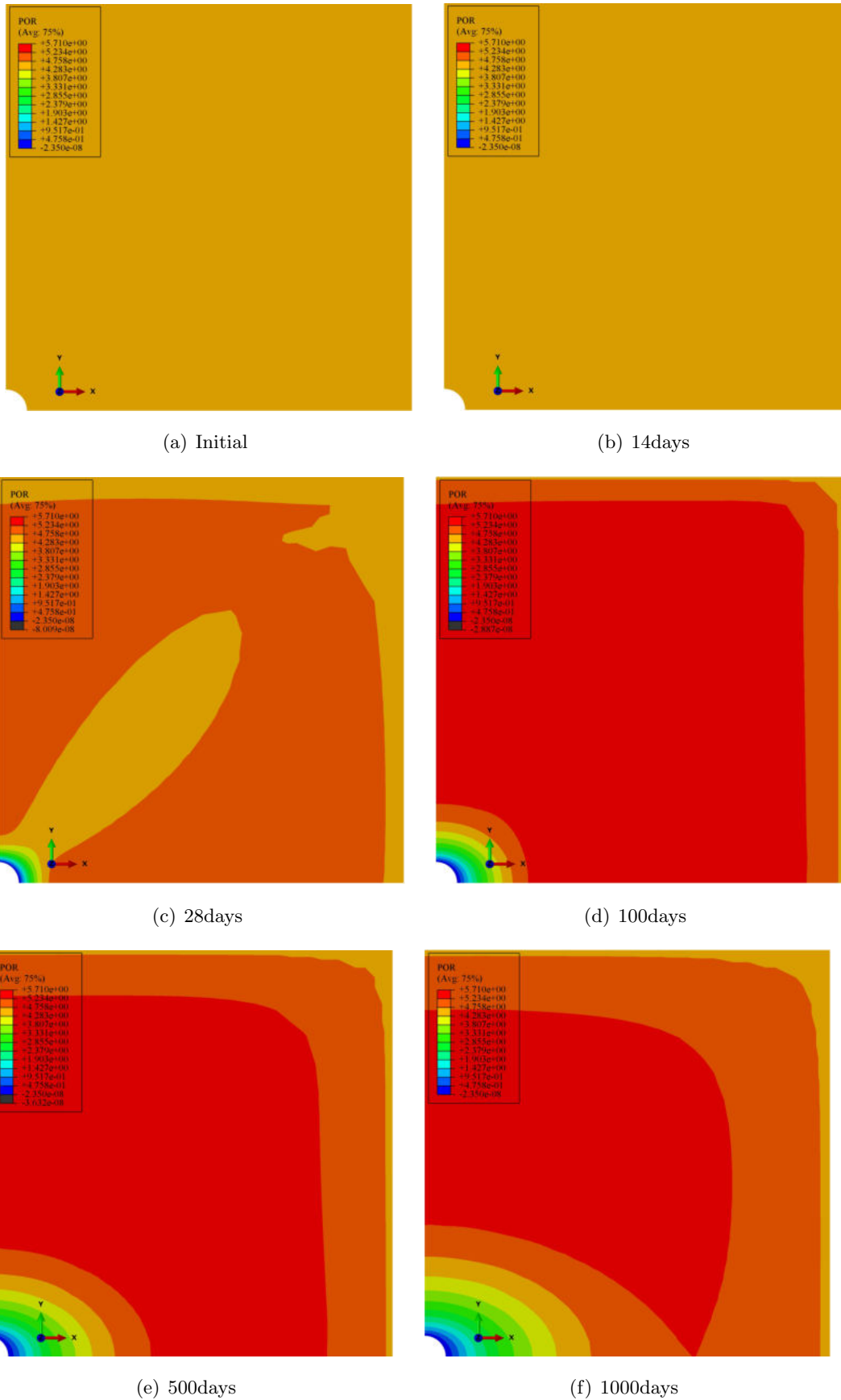


Figure VII.4: Pore pressure distribution at different excavation periods for GED gallery



# Bibliography

- Abou-Chakra Guéry, A. (2007). *Contributions à la modélisation micromécanique du comportement non linéaire de l'argilite du Callovo-Oxfordien*. PhD thesis, Lille 1.
- Al-Harthi, A. A. (1998). Effect of planar structures on the anisotropy of ranyah sandstone, saudi arabia. *Engineering geology*, 50(1-2):49–57.
- Allirot, D., Boehler, J., et al. (1979). Evolution of mechanical properties of a stratified rock under confining pressure. In *4th ISRM Congress*. International Society for Rock Mechanics and Rock Engineering.
- Alonso, E. E., Gens, A., and Josa, A. (1990). A constitutive model for partially saturated soils. *Géotechnique*, 40(3):405–430.
- Andra (2005a). Dossier 2005–référentiel du site meuse/haute-marne–tome 2.
- Andra (2005b). Dossier 2005 argile : Synthèse : Evolution phénoménologique du stockage géologique.
- Armand, G., Bumbieler, F., Conil, N., de la Vaissière, R., Bosgiraud, J.-M., and Vu, M.-N. (2017a). Main outcomes from in situ thermo-hydro-mechanical experiments programme to demonstrate feasibility of radioactive high-level waste disposal in the callovo-oxfordian claystone. *Journal of Rock Mechanics and Geotechnical Engineering*, 9(3):415–427.
- Armand, G., Conil, N., Talandier, J., and Seyedi, D. M. (2017b). Fundamental aspects of the hydromechanical behaviour of callovo-oxfordian claystone: from experimental studies to model calibration and validation. *Computers and Geotechnics*, 85:277–286.
- Armand, G., Leveau, F., Nussbaum, C., de La Vaissiere, R., Noiret, A., Jaeggi, D., Landrein, P., and Righini, C. (2014). Geometry and properties of the excavation-induced fractures at the meuse/haute-marne url drifts. *Rock Mechanics and Rock Engineering*, 47(1):21–41.

- Armand, G. and Su, K. (2006). Hydromechanical coupling phenomena observed during a shaft sinking experiment in a deep argillaceous rock. In *Proceeding of the Geoproc 2006 conference, to be publish, Nanjing*.
- Bagheripour, M. H., Rahgozar, R., Pashnesaz, H., and Malekinejad, M. (2011). A complement to hoek-brown failure criterion for strength prediction in anisotropic rock. *Geomechanics and Engineering*, 3(1):61–81.
- Barthélémy, J.-F. and Dormieux, L. (2004). A micromechanical approach to the strength criterion of drucker-prager materials reinforced by rigid inclusions. *International Journal for Numerical and Analytical Methods in Geomechanics*, 28(7-8):565–582.
- Bian, H., Zhang, X., and Shao, J. (2017). A coupled elastoplastic and visco-plastic damage model for hard clay and its application for the underground gallery excavation. *Underground Space*, 2(1):60–72.
- Bignonnet, F., Dormieux, L., and Kondo, D. (2016). A micro-mechanical model for the plasticity of porous granular media and link with the cam clay model. *International Journal of Plasticity*, 79:259–274.
- Bikong, C., Hoxha, D., and Shao, J.-F. (2015). A micro-macro model for time-dependent behavior of clayey rocks due to anisotropic propagation of microcracks. *International Journal of Plasticity*, 69:73–88.
- Biot, M. A. (1941). General theory of three-dimensional consolidation. *Journal of applied physics*, 12(2):155–164.
- Bornert, M. (2010). X-ray micro ct for studying strain localization in clay rocks under triaxial compression. *Advances in X-ray Tomography for Geomaterials*, 118:35.
- Bornert, M., Bretheau, T., and Gilormini, P. (2001). *Homogénéisation en mécanique des matériaux, Tome 1: Matériaux aléatoires élastiques et milieux périodiques*.
- Bornert, M., Vales, F., Gharbi, H., and Nguyen Minh, D. (2010). Multiscale full-field strain measurements for micromechanical investigations of the hydromechanical behaviour of clayey rocks. *Strain*, 46(1):33–46.

- Castañeda, P. P. and Willis, J. R. (1995). The effect of spatial distribution on the effective behavior of composite materials and cracked media. *Journal of the Mechanics and Physics of Solids*, 43(12):1919–1951.
- Charlier, R., Collin, F., Pardoën, B., Talandier, J., Radu, J.-P., and Gerard, P. (2013). An unsaturated hydro-mechanical modelling of two in-situ experiments in callovo-oxfordian argillite. *Engineering geology*, 165:46–63.
- Chiarelli, A. (2000). *Experimental investigation and constitutive modeling of coupled elastoplastic damage in hard argillitstones*. PhD thesis, Doctoral Thesis, University of Lille 1 (in French).
- Chiarelli, A.-S., Shao, J.-F., and Hoteit, N. (2003). Modeling of elastoplastic damage behavior of a claystone. *International Journal of plasticity*, 19(1):23–45.
- Coussy, O. (2004). *Poromechanics*. John Wiley & Sons.
- Coussy, O., Eymard, R., and Lassabatère, T. (1998). Constitutive modeling of unsaturated drying deformable materials. *Journal of Engineering Mechanics*, 124(6):658–667.
- Cuvilliez, S., Djouadi, I., Raude, S., and Fernandes, R. (2017). An elastoviscoplastic constitutive model for geomaterials: Application to hydromechanical modelling of claystone response to drift excavation. *Computers and Geotechnics*, 85:321–340.
- Desbois, G., Höhne, N., Urai, J. L., Bésuelle, P., and Viggiani, G. (2017). Deformation in cemented mudrock (callovo-oxfordian clay) by microcracking, granular flow and phyllosilicate plasticity: insights from triaxial deformation, broad ion beam polishing and scanning electron microscopy. *Solid Earth*, 8(2):291.
- Dormieux, L., Kondo, D., and Ulm, F.-J. (2006). *Microporomechanics*. John Wiley & Sons.
- Dormieux, L., Molinari, A., and Kondo, D. (2002). Micromechanical approach to the behavior of poroelastic materials. *Journal of the Mechanics and Physics of Solids*, 50(10):2203–2231.
- Enssle, C. P., Cruchaudet, M., Croisé, J., and Brommundt, J. (2011). Determination of the permeability of the callovo-oxfordian clay at the metre to decametre scale. *Physics and Chemistry of the Earth, Parts A/B/C*, 36(17-18):1669–1678.

- Eshelby, J. D. (1957). The determination of the elastic field of an ellipsoidal inclusion, and related problems. *Proceedings of the royal society of London. Series A. Mathematical and physical sciences*, 241(1226):376–396.
- Fabre, G. and Pellet, F. (2006). Creep and time-dependent damage in argillaceous rocks. *International Journal of Rock Mechanics and Mining Sciences*, 43(6):950–960.
- Farhat, F., Shen, W., and Shao, J.-F. (2017). A micro-mechanics based viscoplastic model for clayey rocks. *Computers and Geotechnics*, 89:92–102.
- Fassi-Fehri, O., Hihi, A., and Berveiller, M. (1989). Multiple site self consistent scheme. *International journal of engineering science*, 27(5):495–502.
- Fredlund, D. G. and Rahardjo, H. (1993). *Soil mechanics for unsaturated soils*. John Wiley & Sons.
- Gasc-Barbier, M., Chanchole, S., and Bérést, P. (2004). Creep behavior of bure clayey rock. *Applied Clay Science*, 26(1-4):449–458.
- Gaucher, E., Robelin, C., Matray, J., Negrel, G., Gros, Y., Heitz, J., Vinsot, A., Rebours, H., Cassagnabère, A., and Bouchet, A. (2004). Andra underground research laboratory: interpretation of the mineralogical and geochemical data acquired in the callovian–oxfordian formation by investigative drilling. *Physics and Chemistry of the Earth, Parts A/B/C*, 29(1):55–77.
- Giraud, A., Huynh, Q. V., Hoxha, D., and Kondo, D. (2007). Application of results on eshelby tensor to the determination of effective poroelastic properties of anisotropic rocks-like composites. *International journal of solids and structures*, 44(11-12):3756–3772.
- Guéry, A. A.-C., Cormery, F., Shao, J.-F., and Kondo, D. (2008). A micromechanical model of elastoplastic and damage behavior of a cohesive geomaterial. *International Journal of Solids and structures*, 45(5):1406–1429.
- Guéry, A. A.-C., Cormery, F., Shao, J.-F., and Kondo, D. (2010). A comparative micromechanical analysis of the effective properties of a geomaterial: effect of mineralogical compositions. *Computers and Geotechnics*, 37(5):585–593.

- Guo, T., Faleskog, J., and Shih, C. (2008). Continuum modeling of a porous solid with pressure-sensitive dilatant matrix. *Journal of the Mechanics and Physics of Solids*, 56(6):2188–2212.
- He, Z., Dormieux, L., and Kondo, D. (2013). Strength properties of a drucker–prager porous medium reinforced by rigid particles. *International Journal of Plasticity*, 51:218–240.
- Hill, R. (1965). A self-consistent mechanics of composite materials. *Journal of the Mechanics and Physics of Solids*, 13(4):213–222.
- Hoxha, D. and Auvray, C. (2004). Résultats des essais sur échantillons pour le développement des modèles rhéologiques hm et thm des argillites. *Rapport Andra n D. RP. 0ENG. 98.013/A*.
- Hoxha, D., Giraud, A., Homand, F., and Auvray, C. (2007). Saturated and unsaturated behaviour modelling of meuse–haute/marne argillite. *International Journal of Plasticity*, 23(5):733–766.
- Huang, Y., Shen, W., Shao, J.-F., Guéry, A. A.-C., and Jia, Y. (2014). Multi-scale modeling of time-dependent behavior of claystones with a viscoplastic compressible porous matrix. *Mechanics of Materials*, 79:25–34.
- Jeong, H.-Y. (2002). A new yield function and a hydrostatic stress-controlled void nucleation model for porous solids with pressure-sensitive matrices. *International journal of solids and structures*, 39(5):1385–1403.
- Jia, Y., Bian, H., Su, K., Kondo, D., and Shao, J.-F. (2010). Elastoplastic damage modeling of desaturation and resaturation in argillites. *International journal for numerical and analytical methods in geomechanics*, 34(2):187–220.
- Lebensohn, R., Tomé, C., and Maudlin, P. (2004). A selfconsistent formulation for the prediction of the anisotropic behavior of viscoplastic polycrystals with voids. *Journal of the Mechanics and Physics of Solids*, 52(2):249–278.
- Lenoir, N., Bornert, M., Desrues, J., Bésuelle, P., and Viggiani, G. (2007). Volumetric digital image correlation applied to x-ray microtomography images from triaxial compression tests on argillaceous rock. *Strain*, 43(3):193–205.
- Lide, D. R. (2004). *CRC handbook of chemistry and physics*, volume 85. CRC press.

- Liu, Z. and Shao, J. (2016). Moisture effects on damage and failure of bure claystone under compression. *Géotechnique Letters*, 6(3):182–186.
- Liu, Z., Shao, J., Xie, S., Conil, N., and Talandier, J. (2019). Mechanical behavior of claystone in lateral decompression test and thermal effect. *Rock Mechanics and Rock Engineering*, 52(2):321–334.
- Liu, Z., Shao, J., Xie, S., Conil, N., and Zha, W. (2018a). Effects of relative humidity and mineral compositions on creep deformation and failure of a claystone under compression. *International Journal of Rock Mechanics and Mining Sciences*, 103:68–76.
- Liu, Z., Xie, S., Shao, J., and Conil, N. (2018b). Multi-step triaxial compressive creep behaviour and induced gas permeability change of clay-rich rock. *Géotechnique*, 68(4):281–289.
- Liu, Z., Xie, S., Shao, J.-F., and Conil, N. (2015). Effects of deviatoric stress and structural anisotropy on compressive creep behavior of a clayey rock. *Applied Clay Science*, 114:491–496.
- Maghous, S., Dormieux, L., and Barthélémy, J.-F. (2009). Micromechanical approach to the strength properties of frictional geomaterials. *European Journal of Mechanics-A/Solids*, 28(1):179–188.
- Mánica, M., Gens, A., Vaunat, J., and Ruiz, D. F. (2017). A time-dependent anisotropic model for argillaceous rocks. application to an underground excavation in callovo-oxfordian claystone. *Computers and Geotechnics*, 85:341–350.
- Masri, M., Sibai, M., Shao, J.-F., and Mainguy, M. (2014). Experimental investigation of the effect of temperature on the mechanical behavior of tournemire shale. *International Journal of Rock Mechanics and Mining Sciences*, 70:185–191.
- Menaceur, H., Delage, P., Tang, A.-M., and Conil, N. (2015). The thermo-mechanical behaviour of the callovo-oxfordian claystone. *International Journal of Rock Mechanics and Mining Sciences*, 78:290–303.
- Mori, T. and Tanaka, K. (1973). Average stress in matrix and average elastic energy of materials with misfitting inclusions. *Acta metallurgica*, 21(5):571–574.

- Mura, T. (1987). Micromechanics of defects in solids. vol. 3. *Springer Science & Business Media*, 580:21.
- Mura, T. (2013). *Micromechanics of defects in solids*. Springer Science & Business Media.
- Nemat-Nasser, S., Lori, M., and Datta, S. (1996). Micromechanics: overall properties of heterogeneous materials.
- Niandou, H., Shao, J., Henry, J., and Fourmaintraux, D. (1997). Laboratory investigation of the mechanical behaviour of tournemire shale. *International Journal of Rock Mechanics and Mining Sciences*, 34(1):3–16.
- Pan, Y.-C. and Chou, T.-W. (1976). Point force solution for an infinite transversely isotropic solid.
- Panet, M. et al. (1976). La mécanique des roches appliquée aux ouvrages de génie civil.
- Pardoen, B. and Collin, F. (2017). Modelling the influence of strain localisation and viscosity on the behaviour of underground drifts drilled in claystone. *Computers and Geotechnics*, 85:351–367.
- Pham, Q. T. (2006). *Effets de la désaturation et de la resaturation sur l'argilite dans les ouvrages souterrains*. PhD thesis.
- Pietruszczak, S., Lydzba, D., and Shao, J.-F. (2002). Modelling of inherent anisotropy in sedimentary rocks. *International Journal of Solids and Structures*, 39(3):637–648.
- Pietruszczak, S., Lydzba, D., and Shao, J.-F. (2004). Description of creep in inherently anisotropic frictional materials. *Journal of Engineering Mechanics*, 130(6):681–690.
- Pietruszczak, S. and Mroz, Z. (2000). Formulation of anisotropic failure criteria incorporating a microstructure tensor. *Computers and Geotechnics*, 26(2):105–112.
- Pietruszczak, S. and Mroz, Z. (2001). On failure criteria for anisotropic cohesive-frictional materials. *International journal for numerical and analytical methods in geomechanics*, 25(5):509–524.

- Qi, M. (2016). *Modélisation micromécanique de l'endommagement et du frottement dans des géomatériaux initialement anisotropes*. PhD thesis, Lille 1.
- Robinet, J.-C. (2008). *Minéralogie, porosité et diffusion des solutés dans l'argilite du Callovo-Oxfordien de Bure (Meuse, Haute-Marne, France) de l'échelle centimétrique à micrométrique*. PhD thesis, Poitiers.
- Robinet, J.-C., Sardini, P., Coelho, D., Parneix, J.-C., Prêt, D., Sammartino, S., Boller, E., and Altmann, S. (2012). Effects of mineral distribution at mesoscopic scale on solute diffusion in a clay-rich rock: Example of the callovo-oxfordian mudstone (bure, france). *Water Resources Research*, 48(5).
- Seyedi, D. M., Armand, G., and Noiret, A. (2017). “transverse action”—a model benchmark exercise for numerical analysis of the callovo-oxfordian claystone hydromechanical response to excavation operations. *Computers and Geotechnics*, 85:287–305.
- Shao, J.-F., Jia, Y., Kondo, D., and Chiarelli, A.-S. (2006). A coupled elastoplastic damage model for semi-brittle materials and extension to unsaturated conditions. *Mechanics of materials*, 38(3):218–232.
- Shen, W., Cao, Y., Liu, Z., and Shao, J.-F. (2020). A multiscale elastoplastic constitutive model for geomaterials with a porous matrix-inclusion microstructure. *Computers and Geotechnics*, 126:103683.
- Shen, W., Kondo, D., Dormieux, L., and Shao, J.-F. (2013a). A closed-form three scale model for ductile rocks with a plastically compressible porous matrix. *Mechanics of Materials*, 59:73–86.
- Shen, W., Lanoye, E., Dormieux, L., and Kondo, D. (2014). Homogenization of saturated double porous media with eshelby-like velocity field. *Acta Geophysica*, 62(5):1146–1162.
- Shen, W., Pastor, F., and Kondo, D. (2013b). Improved criteria for ductile porous materials having a green type matrix by using eshelby-like velocity fields. *Theoretical and Applied Fracture Mechanics*, 67:14–21.
- Shen, W. and Shao, J.-F. (2015a). A micro–macro model for porous geomaterials with inclusion debonding. *International Journal of Damage Mechanics*, 24(7):1026–1046.

- Shen, W. and Shao, J.-F. (2015b). A micromechanical model of inherently anisotropic rocks. *Computers and Geotechnics*, 65:73–79.
- Shen, W. and Shao, J.-F. (2016). An incremental micro-macro model for porous geomaterials with double porosity and inclusion. *International Journal of Plasticity*, 83:37–54.
- Shen, W., Shao, J.-F., Dormieux, L., and Kondo, D. (2012a). Approximate criteria for ductile porous materials having a green type matrix: Application to double porous media. *Computational materials science*, 62:189–194.
- Shen, W., Shao, J.-F., and Kondo, D. (2017). Macroscopic criteria for green type porous materials with spheroidal voids: application to double porous materials. *International Journal for Numerical and Analytical Methods in Geomechanics*, 41(13):1453–1473.
- Shen, W., Shao, J.-F., Kondo, D., and Gatmiri, B. (2012b). A micro–macro model for clayey rocks with a plastic compressible porous matrix. *International journal of plasticity*, 36:64–85.
- Shen, W., Shao, J.-F., Oueslati, A., De Saxcé, G., and Zhang, J. (2018). An approximate strength criterion of porous materials with a pressure sensitive and tension-compression asymmetry matrix. *International Journal of Engineering Science*, 132:1–15.
- Singh, J., Ramamurthy, T., and Rao, G. V. (1989). Strength anisotropies in rocks. *Indian Geotechnical Journal*, 19(2):147–166.
- Souley, M., Armand, G., and Kazmierczak, J.-B. (2017). Hydro-elasto-viscoplastic modeling of a drift at the meuse/haute-marne underground research laboratory (url). *Computers and Geotechnics*, 85:306–320.
- Ullemeyer, K., Siegesmund, S., Rasolofosaon, P. N., and Behrmann, J. H. (2006). Experimental and texture-derived p-wave anisotropy of principal rocks from the transalp traverse: an aid for the interpretation of seismic field data. *Tectonophysics*, 414(1-4):97–116.
- Valès, F., Minh, D. N., Gharbi, H., and Rejeb, A. (2004). Experimental study of the influence of the degree of saturation on physical and mechanical properties in tournemire shale (france). *Applied Clay Science*, 26(1-4):197–207.

- Van den Eijnden, A., Bésuelle, P., Collin, F., Chambon, R., and Desrues, J. (2017). Modeling the strain localization around an underground gallery with a hydro-mechanical double scale model; effect of anisotropy. *Computers and Geotechnics*, 85:384–400.
- Wang, L., Bornert, M., Héripré, E., Chanchole, S., Pouya, A., and Halphen, B. (2015). The mechanisms of deformation and damage of mudstones: a micro-scale study combining esem and dic. *Rock Mechanics and Rock Engineering*, 48(5):1913–1926.
- Weibull, W. (1951). Wide applicability. *Journal of applied mechanics*, 103(730):293–297.
- Wileveau, Y., Cornet, F., Desroches, J., and Blumling, P. (2007). Complete in situ stress determination in an argillite sedimentary formation. *Physics and Chemistry of the Earth, Parts A/B/C*, 32(8-14):866–878.
- Yang, D., Chanchole, S., Valli, P., and Chen, L. (2013). Study of the anisotropic properties of argillite under moisture and mechanical loads. *Rock mechanics and rock engineering*, 46(2):247–257.
- Yao, C., Shao, J., Jiang, Q., and Zhou, C. (2017). Numerical study of excavation induced fractures using an extended rigid block spring method. *Computers and Geotechnics*, 85:368–383.
- Zaoui, A. (2002). Continuum micromechanics: survey. *Journal of Engineering Mechanics*, 128(8):808–816.
- Zhang, C.-L. (2017). Examination of effective stress in clay rock. *Journal of Rock Mechanics and Geotechnical Engineering*, 9(3):479–489.
- Zhang, C.-L. (2018). Thermo-hydro-mechanical behavior of clay rock for deep geological disposal of high-level radioactive waste. *Journal of Rock Mechanics and Geotechnical Engineering*, 10(5):992–1008.
- Zhang, C.-L., Armand, G., Conil, N., and Laurich, B. (2019). Investigation on anisotropy of mechanical properties of callovo-oxfordian claystone. *Engineering Geology*, 251:128–145.

- Zhang, C.-L., Rothfuchs, T., Su, K., and Hoteit, N. (2007). Experimental study of the thermo-hydro-mechanical behaviour of indurated clays. *Physics and Chemistry of the Earth, Parts A/B/C*, 32(8-14):957–965.
- Zhang, F., Xie, S., Hu, D., Shao, J.-F., and Gatmiri, B. (2012). Effect of water content and structural anisotropy on mechanical property of claystone. *Applied Clay Science*, 69:79–86.
- Zhou, H., Jia, Y., and Shao, J.-F. (2008). A unified elastic–plastic and viscoplastic damage model for quasi-brittle rocks. *International Journal of Rock Mechanics and Mining Sciences*, 45(8):1237–1251.